Unveiling Unique Solvation Phenomena and Interfacial Nitrogen Oxide Interactions in

Organic Solutions with Implications for Atmospheric Aerosol

Dissertation

Presented in Partial Fulfillment of the Requirements for the Degree Doctor of Philosophy

in the Graduate School of The Ohio State University

By

Jessica B. Clark

Graduate Program in Chemistry

The Ohio State University

2024

Dissertation Committee

Dr. Heather C. Allen, Advisor

Dr. Bern Kohler

Dr. Zachary D. Schultz

Abstract

Understanding the fundamental interactions within and at the surface of atmospheric aerosol is of the utmost importance as they drive the properties of aerosol that influence global climate and public health. The first work presented herein explores the highly perturbed structure of water within systems inspired by phase separated organic aerosol. An approach is taken that combines polarized Raman spectroscopy and molecular dynamics (carried out by collaborator) to reveal the structural changes that occur as water is added incrementally to propylene carbonate (PC), a polar, aprotic solvent that is relevant in the environment and in electrochemical systems. Polarized Raman spectra of PC solutions were collected for water mole fractions $0.003 \leq \chi_{water} \leq 0.296$, which encompasses the solubility range of water in PC. The novel approach taken to the study of water-in-PC mixtures herein provides additional hydrogen bond and solvation characterization of this system that has not been achieveable in previous studies. Analysis of the polarized carbonyl Raman band in conjunction with simulations demonstrated that the bulk structure of the solvent remained unperturbed upon the addition of water. Experimental spectra in the O-H stretching region were decomposed through Gaussian fitting into sub-bands and studies on dilute HOD in H_2O. With the aid of simulations, we identified these different bands as water arrangements having different degrees of hydrogen bonding. The observed water structure within PC indicates that water tends to self-

aggregate, forming a hydrogen bond network that is distinctly different from the bulk and dependent on concentration. For example, at moderate concentrations, the most likely aggregate structures are chains of water molecules, each with two hydrogen bonds on average.

The interaction of NO_2 with organic interfaces is critical in atmospheric processing of marine and continental aerosol as well as in the development of NO_2 sensing and trapping technologies. Recent studies point to the importance of surface oxygen groups in these systems, however the role of specific functional groups on the microscopic level has yet to be fully established. In the second part of this work, the aim is to provide fundamental information on the behavior of NO_2 at atmospherically relevant organic interfaces that may also help inform innovation in NO_2 sensing and trapping development. An investigation into the structural changes induced by NO_2 at the surface of PC, an environmentally relevant carbonate ester, is presented. Surface-sensitive spectra of the PC liquid surface are acquired before, during, and after exposure to NO_2 using infrared reflection-absorption spectroscopy (IRRAS). Spectra reveal that NO_2 preferentially interacts with the carbonyl of PC at the interface, forming a distribution of binding symmetries. At low ppm levels, NO_2 saturates the PC surface within 10 minutes and the perturbations to the surface are constant over time during the flow of NO_2. Upon removal of NO_2 flow, and under atmospheric pressures, these interactions are reversible, and the liquid surface structure of PC recovers completely within 30 min. Another ester-containing molecule, diethyl sebacate (DES), was also investigated and the same carbonyl-specific interaction with NO_2 was intermittently observed.

N$_2$O$_5$ is an important atmospheric oxidant that plays a critical role in the nighttime chemistry of the troposphere, where it is efficiently hydrolyzed at the surface of aerosol particles to form HNO$_3$. The decomposition of N$_2$O$_5$ at the interface proceeds through a unique pathway that requires the separation of the charged species NO$_2^+$ and NO$_3^-$ to be stabilized. This property of N$_2$O$_5$ makes it an ideal probe molecule to inform on the fundamental properties that lead to charge stabilization at soft interfaces (i.e. air/liquid interfaces). The final part of this work describes the design, construction, and troubleshooting of a novel system wherein N$_2$O$_5$ is synthesized and flowed over the surface of low vapor pressure organic liquids (propylene carbonate and diethyl sebacate). Infrared reflection-absorption spectroscopy enables the elucidation of the surface structure before, during, and after N$_2$O$_5$ exposure. IRRAS experiments reveal a side reaction with KBr windows, leading to the buildup of HNO$_3$ over time. Additional analysis of the N$_2$O$_5$ flow demonstrates that there is significant H$_2$O contamination, leading to high concentrations of HNO$_3$ gas. Possible solutions to remove excess water are discussed. Preliminary results of the N$_2$O$_5$ flow over the surface of PC and DES demonstrate a reversible perturbation to the carbonyl mode for each organic, much like that observed in the second work presented here.

Dedication

To the little girl who wanted to be a Dixie Chick when she grew up.

The backup plan isn't half bad.

Acknowledgments

As I write this today, I am sitting on the campus of my undergraduate university and thinking about just how far my academic journey has taken me. I am reminded that during each phase, the success that I have found would not be possible without all the incredible people who have supported me along the way. To my family, I am thankful beyond words for your endless support and encouragement. You have taught me to work hard and to never give up on my dreams. Your interest in my research and genuine desire to understand it, even as non-scientists, has meant the world to me. Mom, Dad, Sis, I love you to the moon and stars.

To my wonderful husband Travis, you have made so many sacrifices to help make this dream a reality. I am eternally grateful for you and have been so lucky to have you by my side every step of the way. Your passion for science has been a constant inspiration and a force that has kept me going through the most difficult moments of this process. While our fur babies Sophie, Vinny, and Piper have not helped to make this process go smoother, they have been a constant reminder to stop and appreciate the small things in life. I would like to say thank you to the family that I have gained through marriage for also being some of my biggest cheerleaders. To my father-in law, who is always there to ask the tough questions and make sure I keep the "physics" in "physical chemistry" and to my mother-in-law who is always there when I need a listening ear, I am so grateful for your support.

The culmination of my academic journey in this dissertation would, of course, not have been possible without the guidance and mentorship of my PhD advisor, Dr. Heather Allen. Dr. Allen has shown me what it takes to carve space for yourself as a woman in a male-dominated field. She has pushed me to move past my perfectionistic tendencies and to understand that scientific progress is not perfect, nor linear. With her support these past five years, I have grown beyond my imagination both personally and as a scientist. I would also like to thank Dr. David Limmer who served as a collaborator and mentor to me in the later stages of this process. Our work together has helped me see my science from new perspectives and pushed our projects to be greater than the individual components.

Finally, the support, comradery, and friendship that I have found among the members of the Allen lab has been a source of great joy and inspiration for me during this time. I would like to say thank you to all current members of the lab for helping to create such a supportive environment in which we can all help each other to learn and grow. Dr. Maria Vazquez de Vasquez and Dr. Kim Carter-Fenk were incredible mentors to me as I was first learning to navigate graduate school and have continued to be sources of invaluable advice. To Dr. Abbie Enders and Dr. Nicole North, I don't have the words to say how much your friendship has meant to me. I am so glad we got to take this journey together.

Vita

Born – Middletown, OH…………………………………………..November 8, 1996

Valedictorian – Franklin High School, Franklin, OH……………………May 29, 2015

B.S. Chemistry, *Summa Cum Laude*, Wright State University……………….May 4, 2019

Graduate Fellow, The Ohio State University………………...…Aug. 2019 – Aug. 2020

Graduate Teaching Associate, The Ohio State University……...…Aug. 2020 – Dec. 2021

Graduate Research Associate, The Ohio State University…………….Jan. 2022 – Present

Publications

Clark, J.B. and Allen, H.C. Interfacial Carbonyl Groups of Propylene Carbonate and Diethyl Sebacate Facilitate the Reversible Binding of Nitrogen Dioxide. *ChemRxiv*, 2024.

North, N.M; **Clark, J.B.**; Enders, A.A.; Grooms, A.; Wairegi, S.; Duah, K.A; Palassis-Naziri, E.; Badu-Tawiah, A.; Allen, H.C. Multi Concentration Determination in Field Ocean Samples Through Regression Based Machine Learning. *ChemRxiv*, 2024.

Enders, A.A.; North, N.M.; **Clark, J.B.**; Allen, H.C. Saccharide concentration prediction from proxy ocean samples analyzed via infrared spectroscopy and quantitative machine learning. *ACS Earth & Space Chem*, doi/10.1021/acsearthspacechem.3c00310.

Clark, J.B.; Bowling-Charles, T.; Biswas, B.; Proma, S.J.; Limmer, D.T.; Allen, H.C. Structural Evolution of Water-in-Propylene Carbonate Mixtures Revealed by Polarized Raman Spectroscopy and Molecular Dynamics. *Phys. Chem. Chem. Phys.*, 2023, 25, 23963-23976

Enders, A.A.; **Clark, J.B.**; Elliott, S.M.; Allen, H.C. New Insights into Cation Driven Adsorption of Proteins at the Air-Water Interface Through IRRAS Studies of Bovine Serum Albumin. *Langmuir*, 2023, 39, 15, 5505–5513.

Vazquez de Vasquez, M.G.; Carter-Fenk, K.A.; McCaslin, L.; Beasley, E.; **Clark, J.B.**; Allen, H.C. Hydration and Hydrogen Bond Disorder of Octadecanoic Acid and Octadecanol Films on Water at 21°C and 1°C. *J. Phys. Chem. A*, 2021, 125, 46, 10065–10078

Fields of Study

Major Field: Chemistry

Table of Contents

List of Tables

List of Figures

List of Equations

List of Common Abbreviations

AA	Double Acceptor Water Hydrogen Bonding Arrangement
ATR	Attenuated Total Reflection
CCD	Charge Coupled Device
DA	Single Donor-Single Acceptor Water Hydrogen Bonding Arrangement
DAA	Single Donor-Double Acceptor Water Hydrogen Bonding Arrangement
DD	Double Donor Water Hydrogen Bonding Arrangement
DDA	Double Donor-Single Acceptor Water Hydrogen Bonding Arrangement
DDAA	Double Donor-Double Acceptor Water Hydrogen Bonding Arrangement
FTIR	Fourier Transform Infrared
GROMOS	Groningen Molecular Simulation
IR	Infrared
IRRAS	Infrared Reflection-Absorption Spectroscopy
LN$_2$	Liquid Nitrogen
MD	Molecular Dynamics
NCE	Noncoincidence Effect
NMR	Nuclear Magnetic Resonance
PC	Propylene Carbonate
PM$_{2.5}$	Particulate Matter Having Diameter < 2.5 μm
SOA	Secondary Organic Aerosol
SPC/E	Extended Simple Point Charge Model of Water

Chapter 1. Introduction

1.1 Motivation

The work presented in this dissertation was conducted to develop a molecular-level understanding of the solvation and uptake properties of unique systems relevant to atmospheric organic aerosol. Advancements towards this goal not only inform on the complex nature of one of the largest components of the biosphere, but also provide fundamental information that is critical in the development of cutting-edge electrochemical and gas-sensing materials.

Aerosol particles are ubiquitous in the atmosphere, with concentrations of up to 10^8 cm^{-3}.[1,2] These particles have significant impacts on both global climate and public health. In regard to climate, aerosol particles absorb and scatter radiation, affecting visibility conditions and directly influencing Earth's albedo.[2] Depending on their composition and morphology, aerosol particles can also influence the formation of clouds by serving as cloud condensation nuclei.[3,4] Public health implications arise from the significant portion of aerosol that contributes to PM$_{2.5}$, a particle size that is shown to easily penetrate the alveolar region of the lungs and cause a plethora of negative health effects.[2] Additionally, aerosol can transport pathogens across great distances, contributing to the spread of infectious disease.[5–7] Particles can be directly emitted into the atmosphere as primary aerosol or formed there by chemical reactions producing secondary aerosol. Major sources

of primary aerosol include biomass burning, volcanic eruptions, fossil fuel combustion, and sea spray from the ocean. Secondary aerosol typically results from condensation of volatile organic compounds following reaction with atmospheric oxidants.[1,2] The variability in sources of atmospheric aerosol leads to an incredibly high degree of compositional complexity. The dynamic and highly complex chemistry of atmospheric aerosol is the reason that it remains the largest source of uncertainty in global climate models.[8,9] Thus, there is a critical need to provide a more complete understanding of the molecular-level processes that govern aerosol properties.

A significant portion (20-90%) of all submicron aerosol in the troposphere is organic aerosol.[10–12] Many studies demonstrate that organic aerosol tends to undergo phase separation in the atmosphere, with up to 65% of all organic aerosol being phase separated.[13] Such particles are then comprised of a water-rich phase containing solvated inorganic material and a second hydrophobic organic-rich phase. The ratio of oxygen to carbon (O:C) for organics in aerosol is generally used as a measure for the likelihood of phase separation. Phase separation occurs most readily for O:C ≤ 0.8. For 0.5 ≤ O:C ≤ 0.8, phase separation has been shown to depend strongly on the functional groups present.[14,15] This process leads to a unique environment in which the bulk properties of water break down due to their confinement within microscopic aerosol particles.

To this point, studies have not been able to develop a consistent picture of the properties of water in confinement, however the general conclusion has been that there is a large degree of correlation between the effects of imposed geometric constraints and the specific interactions between water molecules and their confining environment.[16–18] A

study by Fayer and Levinger using ultrafast infrared pump-probe experiments found that for water/bis(2-ethylhexyl) sulfosuccinate (AOT) reverse micelles that model the morphology of some phase separated organic aerosol, the hydrogen bond dynamics within the confined water pool were strongly influenced by the size of the particle, with small and intermediate sized (d < 5.5 nm) water pools containing no bulk-like water.[17] Using Raman spectroscopy, Crupi and coworkers observed a decrease in bulk-like spectral features corresponding to a shift to less coordinated hydrogen bonding arrangements for water trapped within 25 Å silica pores compared to water within 75 Å pores. Such observations lead to the motivation for the work presented in Chapter 3, which explores the microscopic structure of water under dynamic confinement by the environmentally relevant organic phase, propylene carbonate.

Surface-mediated heterogeneous reactions at the aerosol interface influence particle properties as well as the abundance of atmospheric trace gases.[1,2] Nitrogen oxides make up a group of atmospheric trace gases that are shown to play a pivotal role in the heterogeneous chemistry of aerosol. Commonly referred to as NO_x ($NO + NO_2$), nitrogen oxides are anthropogenic in origin and are commonly found in the polluted troposphere at concentrations in the low ppb range. The oxidation of hydrocarbons in the troposphere by radical species (mostly OH) leads to the formation NO_2 under polluted conditions. The NO_2 produced in this process can then be photolyzed during the daytime to produce O_3, thus resulting in the only known anthropogenic source of tropospheric ozone. As stated previously, NO_x species are also critical in the heterogeneous chemistry of atmospheric aerosol. NO_2 has been shown to accelerate the formation of sulfate aerosol through the

oxidation of SO_2 at the interface.[19] Interfacial reactions of NO_2 also provide a pathway for reservoir species of highly-reactive radicals including OH and Cl to be formed.[20–22] Recent studies have also shown that the composition and formation mechanism of SOA can depend strongly on NO_x conditions.[23–27] The importance of NO_2 in the heterogeneous chemistry of organic aerosol provides the motivation for the work presented in Chapter 4.

During nighttime, the absence of photolysis leads to the formation of NO_3 radicals from the reaction of NO_2 with O_3. NO_3 radicals facilitate the production of secondary organic aerosol (SOA) and can react with NO_2 to form N_2O_5.[1,2] The hydrolysis of N_2O_5 at the surface of aerosol particles provides the major sink for NO_x in the troposphere. This process has been suggested to depend strongly on the dielectric environment as recent advancements in molecular dynamics simulations demonstrate the interfacial hydrolysis mechanism proceeds through a charge-separated pathway.[28] The reactive uptake of N_2O_5 at organic interfaces is known to be influenced by surface morphology and composition,[29–34] however the molecular-level interactions underlying these processes have not been fully elucidated. This provides the motivation for the development of surface-sensitive spectroscopic experiments of N_2O_5 at organic interfaces presented in Chapter 5.

1.2 Dissertation Highlights

In this section, the key contents of the dissertation are summarized. Chapter 2 includes a summary of the theory and instrumentation used to conduct the spectroscopic studies described throughout the dissertation. A brief overview of the theory of vibrational spectroscopy is given. This theory is then extended to linear infrared techniques, reflection

infrared techniques, and Raman spectroscopy. The Raman and infrared reflection-absorption spectroscopy instruments are also described.

Chapter 3 informs on the behavior of water under dynamic confinement by the environmentally relevant organic solvent, propylene carbonate. A detailed deconvolution of polarized Raman spectra as a function of water content in PC shows significant self-association of water molecules within the solvent. The noncoincidence effect of the carbonyl region reveals the primary site of solute-solvent interaction. Molecular dynamics simulations agree with experiment and provide the first insights into the structure of water aggregates within this system. All molecular dynamics experiments described herein were carried out by collaborator, Dr. David Limmer.

Chapter 4 explores the interaction of gas-phase NO_2 with the surface of selected organic esters; propylene carbonate and diethyl sebacate. Here, IRRAS studies provide time-resolved insights into the interfacial structure of the organic liquid surfaces before, during, and after exposure to NO_2. The results demonstrate a carbonyl-mediated, reversible binding of NO_2 at the PC and DES liquid interface. Changes in the PC surface structure as a function of dehydration are also elucidated.

Chapter 5 documents the progress made towards synthesizing N_2O_5 for use as a gas-phase probe molecule in the determination of the charge separation stabilization ability of various dielectric interfaces. The design and construction of the system, which is novel to the lab are described at length. The conduction of control experiments and the improvement of the synthesis system as a result of troubleshooting are included. Results show high levels of water contamination within the gas lines leading to excess formation

of HNO_3. Solutions for this contamination are explored. Preliminary experiments of N_2O_5 flowing over the surface of propylene carbonate and diethyl sebacate show similar carbonyl-specific interactions with the gas molecules at the interface as shown for NO_2 in Chapter 4.

Chapter 2. Theoretical Background and Instrumentation

2.1 Vibrational Spectroscopy Theory

The work presented in this dissertation utilizes the principles of vibrational spectroscopy to unravel the molecular structure of unique chemical environments. Thus, the goal of this section is to provide an overview of the theoretical background necessary to understand such processes. Pertinent information is provided for infrared spectroscopy, Raman spectroscopy, and infrared reflection-absorption spectroscopy (IRRAS).

2.1.1 The Harmonic Oscillator

When considering molecular vibrations, it is useful to first consider a model diatomic molecule taking the form A–B. This molecule can then be modeled as a simple system consisting of two spheres of some mass, m, connected by a spring that represents the chemical bond.[35–37] Upon small displacements caused by stretching or compressing the spring, the potential energy, $V(x)$, of the system is changes with respect to the motion of the two masses within the same plane. This process is described by Hooke's Law,

Equation 1

$$F = \frac{dV(x)}{dx} = -kx$$

where F is the restoring force, k is the spring constant that describes the stiffness of the spring or the strength of the bond, and x is the displacement of the spring from its equilibrium position. Another way to represent x is $r - r_e$, where r is the bond length after

7

some displacement and r_e is the equilibrium bond length. Integration of Equation 1 with respect to x gives,

Equation 2

$$V(x) = \frac{1}{2}kx^2$$

which describes the potential energy of a harmonic oscillator. The time-independent Schrödinger equation is given generally as,

Equation 3

$$H\psi = E\psi$$

where H is the one-dimensional Hamiltonian operator, which when operating on the wavefunction, Ψ, gives an energy, E, multiplied by the wavefunction. The form of the Hamiltonian operator is:

Equation 4

$$H = \frac{-\hbar^2}{2\mu}\frac{\partial^2}{\partial x^2} + V(x).$$

Plugging in the potential energy of the harmonic oscillator given in Equation 2 gives,

Equation 5

$$H = \frac{-\hbar^2}{2\mu}\frac{\partial^2}{\partial x^2} + \frac{1}{2}kx^2$$

where $\hbar$ is the reduced Planck's constant and μ is the reduced mass of the diatomic molecule:

Equation 6

$$\mu = \frac{m_A m_B}{m_A + m_B}.$$

The Schrödinger equation for the harmonic oscillator can then be written as:

8

Equation 7

$$\frac{\partial^2 \psi}{\partial x^2} + \left(\frac{2\mu E_v}{\hbar^2} - \frac{\mu k x^2}{\hbar^2}\right)\psi = 0.$$

From Equation 7, the eigenvalues of the harmonic oscillator are,

Equation 8

$$E_v = h\nu \left(v + \frac{1}{2}\right)$$

where E_v is the energy of each quantized energy level (v = 0, 1, 2, …n) of the harmonic oscillator, ν is the classical vibrational frequency, and h is Planck's constant. Equation 8 demonstrates that adjacent energy levels with the harmonic oscillator are equally spaced by $h\nu$ or, in angular frequency, $\hbar\omega$.

The form of the classical vibrational frequency, ν, can be developed starting from Newton's second law,

Equation 9

$$F = ma$$

where m is mass and a is acceleration, also known as the second derivative of distance with respect to time (d^2x/dt^2). Combining Equation 1 and Equation 9 gives,

Equation 10

$$\frac{d^2 x}{dt^2} = \frac{-kx}{m}$$

which is a differential equation that requires that the second derivative of the solution must equal the original function multiplied by -k/m. Cosine functions provide suitable solutions to this form, therefore the solution for Equation 10 is:

Equation 11

$$x = A\cos(2\pi vt).$$

Taking the second derivative of Equation 11 gives,

Equation 12

$$\frac{d^2x}{dt^2} = -4\pi^2 v^2 A\cos(2\pi vt)$$

Substituting Equation 11 and Equation 12 into the form of Newton's second law given in Equation 10, simplifying and solving for v gives,

Equation 13

$$v = \frac{1}{2\pi}\sqrt{\frac{k}{\mu}}$$

where the mass, m, is replaced with the reduced mass, μ, as this system is describing a diatomic molecule. Equation 13 demonstrates that the vibrational frequency, v, of a bond depends on both the strength of the bond, k, and the reduced mass, μ.

2.1.2 Infrared Spectroscopy

The selection rules for transitions from lower to upper vibrational states through the absorption of infrared light can be demonstrated by considering the transition dipole moment, which also defines the intensity of such transitions. The transition dipole moment ($\boldsymbol{R_v}$) is given by the integral,

Equation 14

$$\boldsymbol{R_v} = \int \psi_v'^* \boldsymbol{\mu}\, \psi_v''\, dx$$

where x is the displacement of the bond from equilibrium and ψ_v' and ψ_v'' are the wavefunctions describing the lower and upper vibrational states, respectively. Here, μ is the electric dipole moment operator, which is defined as,

Equation 15

$$\boldsymbol{\mu} = \sum_i q_i \boldsymbol{r}_i$$

where q_i and r_i are the charge and position vector of the ith particle. Diatomic molecules composed of two atoms of the same element (homonuclear) do not induce a change in dipole moment upon vibration, therefore $\mathbf{R_v}$ is zero. In this case, all vibrational transitions are forbidden. In contrast, heteronuclear diatomic molecules do undergo a change in dipole moment with vibration, which varies with displacement, x. In this case, a Taylor series expansion of the dipole moment can be applied giving,

Equation 16

$$\boldsymbol{\mu} = \boldsymbol{\mu}_e + \left(\frac{d\boldsymbol{\mu}}{dx}\right)_e x + \frac{1}{2!}\left(\frac{d^2\boldsymbol{\mu}}{dx^2}\right)_e x^2 + \cdots$$

where the subscript "e" indicates the equilibrium position of the bond. Following the substitution of this result into Equation 14, the transition dipole moment becomes:

Equation 17

$$\boldsymbol{R_v} = \boldsymbol{\mu}_e \int {\psi_v'}^* \psi_v'' \, dx + \left(\frac{d\boldsymbol{\mu}}{dx}\right)_e \int {\psi_v'}^* x \, \psi_v'' \, dx + \cdots$$

Due to the orthogonality of ψ_v' and ψ_v'', the first term in Equation 17 is zero for all vibrational transitions ($v' \neq v''$). As a result, the second term dictates the vibrational

11

transition and is nonzero only when $\Delta \upsilon = \pm 1$. The intensity, I, of a vibrational absorption

or emission under the harmonic oscillator approximation is:

Equation 18

$$I \propto |R_\upsilon|^2 \propto |\frac{d\boldsymbol{\mu}}{dx}|^2$$

When considering polyatomic molecules, the number of possible vibrational modes

can be calculated by considering the number of degrees of freedom of its motion.[36] First,

3N total degrees of freedom are defined for a molecule with N number of atoms in order

to completely describe the position of each molecule in three-dimensional space. When

defining the motion of the molecule, three types of motion need to be considered:

translation of the entire molecule through space, rotation of the molecule about its center

of gravity, and motion of each atom relative to the others (*i.e.* vibrations). In order to

describe translational motion, three coordinates are needed, thus three out of the total 3N

degrees of freedom result from translation. Nonlinear polyatomic molecules have three

unique axes by which they can rotate, so three additional degrees of freedom are assigned

to rotational motion. The remaining 3N–6 degrees of freedom are assigned to interatomic

motion and give the number of possible molecular vibrations. Linear molecules deviate

from this equation as only two axes of rotation are possible. The number of vibrations

possible for linear molecules is then given by 3N–5. Each vibration identified through this

process is known as a normal mode. The appearance of polyatomic normal modes in

infrared spectra is reliant upon the selection rules described above.

2.1.3 Raman Spectroscopy

Raman spectroscopy is another technique used to probe molecular vibrations. In contrast to infrared spectroscopy, which directly excites vibrations in a molecule though the absorption of IR light, Raman spectroscopy informs on these vibrations through inelastic scattering processes.[35,37,38] Excitation sources for Raman experiments are generally single-wavelength lasers in the visible or near-IR spectral regions and are chosen to be far removed from any absorption bands of the analyte to avoid fluorescence. The excitation source excites the molecule to an energy level between the ground electronic state and the lowest excited electronic state. This state is unquantized and is typically referred to as a virtual state. The most probable scattering process following collision of the photon with the molecule is Rayleigh scattering. In this process, the molecule scatters the light without changing its energy, therefore the collision is said to be elastic. The second most probable Raman scattering process, at standard temperatures, is Stokes scattering. In this process, molecules existing in the vibrational ground state ($\upsilon = 0$) are excited to a virtual state. The molecule then reemits (scatters) the light at an energy less than that of the excitation and the molecule returns to a higher vibrational state. The energy for Stokes scattering is given as,

Equation 19

$$E_{Stokes} = h(\nu_{ex} - \nu_{\upsilon})$$

where ν_{ex} is the frequency of the excitation source and ν_{υ} is the frequency of the vibrational mode. Because this type of scattering results in a change in energy of the photon, the collision is said to be inelastic. Finally, molecules initially existing in the vibrational

excited state ($\upsilon = 1$) can inelastically scatter light to produce a Raman signal with energy greater than the excitation. This process is known as anti-Stokes scattering and the energy is given by:

Equation 20

$$E_{anti-Stokes} = h(\nu_{ex} + \nu_\upsilon).$$

Anti-stokes scattering is less probable than Stokes scattering because the population of vibrational states is determined by the Boltzmann distribution, which shows that at standard temperatures, most molecules exist in their ground vibrational state. The probability of anti-Stokes scattering is increased at elevated temperatures. It is clear from Equation 19 and Equation 20 that the change in energy following Stokes or anti-Stokes scattering is equal to the frequency of the vibrational mode ν_υ, thus the Raman frequency shift and IR absorption frequency are identical for modes active in both methods. These scattering processes are summarized in Figure 1.
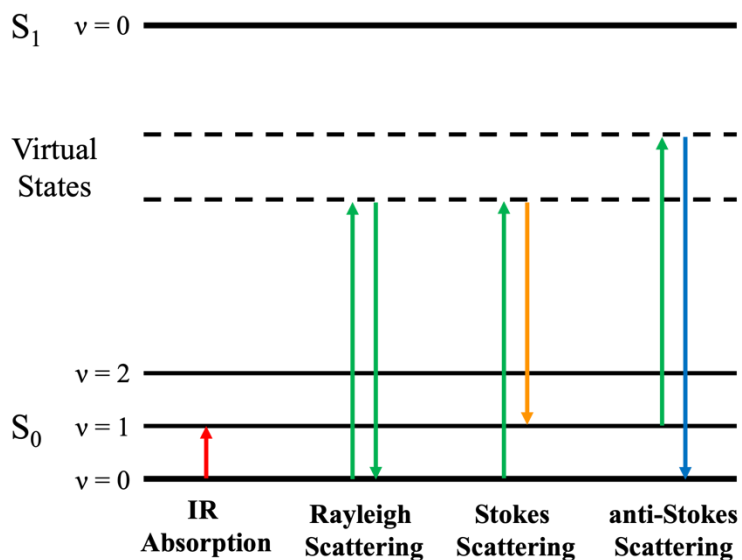
Figure 1. Diagram depicting the scattering processes involved in Raman spectroscopy. Molecules in the ground electronic state (S_0) are promoted to "virtual states" that are lower in energy than the lowest excited electronic state (S_1). Relaxation occurs through scattering.

The physical process of Raman scattering and the selection rules governing it can be understood by first considering the interaction of the oscillating electric field, $\boldsymbol{E}$, of monochromatic radiation with the electron cloud of a particular molecule. The electric field oscillations with time can be described as,

Equation 21

$$E = E_0\cos(2\pi\nu_{ex}t)$$

where E_0 is the amplitude of the oscillation. When the electric field is incident on a molecule, an electric dipole moment is induced. The induced dipole moment, μ, is related to $\boldsymbol{E}$ through the polarizability, α, as follows:

Equation 22

$$\mu = \alpha E.$$

Polarizability is a measure of the ease by which the electron cloud of a bond can be deformed. Substituting Equation 21 into Equation 22 gives:

Equation 23

$$\mu = \alpha E_0 \cos(2\pi\nu_{ex}t).$$

The polarizability varies as a function of the distance between the nuclei relative to equilibrium $(r - r_e)$ according to the Taylor series expansion,

Equation 24

$$\alpha = \alpha_e + (r - r_e)\left(\frac{\partial\alpha}{\partial r}\right)_e$$

where α_e is the polarizability of the bond at the equilibrium internuclear distance $(r = r_e)$. Relatedly, the change internuclear separation varies with the vibrational frequency and can be defined as,

Equation 25

$$r - r_e = r_m cos(2\pi v_v t)$$

where r_m is the maximum internuclear distance relative to equilibrium. Substitution of

Equation 25 into Equation 24 yields:

Equation 26

$$\alpha = \alpha_e + \left(\frac{\partial \alpha}{\partial r}\right)_e r_m cos(2\pi v_v t).$$

To obtain an expression for the induced dipole moment, Equation 26 is substituted into

Equation 23. Carrying out this substitution and simplifying using trigonometric identities

gives:

Equation 27

$$\mu = \alpha_e E_0 \cos(2\pi v_{ex} t) + \frac{E_0}{2} r_m \left(\frac{\partial \alpha}{\partial r}\right)_e \cos[2\pi(v_{ex} - v_v)t]$$

$$+ \frac{E_0}{2} r_m \left(\frac{\partial \alpha}{\partial r}\right)_e \cos[2\pi(v_{ex} + v_v)t].$$

In the above expression, the first term describes Rayleigh scattering and the second and

third terms describe Stokes and anti-Stokes scattering, respectively. The selection rules for

Raman spectroscopy can be discerned by evaluating the transition moment upon a change

in polarizability. Beginning with the transition moment integral given in Equation 14, the

polarizability operator as given in Equation 24 can be substituted in place of the dipole

moment operator.

Equation 28

$$\boldsymbol{R} = \int \psi_v'^* \left[\alpha_e + (r - r_e)\left(\frac{\partial \alpha}{\partial r}\right)_e\right] \psi_v'' \, dr$$

Simplification of the above equation results in,

Equation 29

$$R = \left(\frac{\partial \alpha}{\partial r}\right)_e \int \psi_v'^* (r - r_e)\, \psi_v'' \, dr.$$

From Equation 29, it is clear that in order for Raman scattering to occur, there must be a change in polarizability during the vibration. Additionally, the selection rules dictated by this equation require that Δv must be ± 1 in order for the transition moment integral to be nonzero.

2.1.4 Infrared Reflection-Absorption Spectroscopy

Infrared reflection-absorption spectroscopy is a surface-sensitive spectroscopic technique that has been used extensively to understand the structure and interactions occurring at liquid interfaces following some perturbation to the surface.[39–47] Often, this perturbation is the spontaneous assembly of lipid monolayers anchored at the air/water interface.[39,44,48] Other perturbations investigated using this technique include surface enrichment of organics (e.g. saccharides and proteins)[41,48,49] and interfacial gas-liquid interactions.[42,50] This technique measures the small fraction of light (4-8%)[45] that is reflected off the liquid surface relative to that reflected from a reference surface. Spectra are obtained by calculating the reflectance-absorbance (RA) which is defined as,

Equation 30

$$RA = -log_{10}\left(\frac{R}{R_0}\right)$$

where R is the reflectance measured for the sample interface (following perturbation) and R_0 is the reflectance measured for the reference surface (prior to perturbation). The major advantage of this technique compared to other surface vibrational spectroscopies is that the

entire mid-IR region ($450 - 4000$ cm^{-1}) of the spectrum can be sampled at once, leading to quick and highly reproducible measurements. Such measurements are enabled by the use of highly sensitive HgCdTe (MCT) detectors, which provide excellent signal-to noise ratios for the low intensity process of reflection. The surface-sensitivity of this technique originates from both the sampling geometry and the calculation of RA. Angles of incidence for IRRAS spectra are chosen close to that of the bulk liquid's Brewster angle in order to minimize reflection and sampling of the bulk. Additionally, when RA is calculated, the signal from the bulk is subtracted from the sample spectrum. The majority of the remaining signal is due to interfacial changes from the perturbation at the surface.

Electromagnetic theory can be used to derive expressions describing the reflection and transmission of light at interfaces.[35,38,51] A summary of the electromagnetic theory relevant to IRRAS spectra is presented here. It is useful to start by considering a plane wave of that is incident on a dielectric medium at a defined angle of incidence, θ_i. Interaction of the wave with the interface results in it being split in two, where one wave then propagates into the second phase (transmission/refraction) and the second wave is redirected by the second phase but continues propagating in the original phase (reflection). The Law of Reflection states that the angle of incidence, θ_i, is equal to the angle of reflection θ_r,

Equation 31

$$\theta_i = \theta_r$$

where the angles are defined relative to the surface normal. The behavior of the transmitted wave is described by the Law of Refraction (also known as Snell's Law).

Equation 32

$$\tilde{n}_1 sin\theta_i = \tilde{n}_2 sin\theta_t$$

where θ_t is the angle of the transmitted wave and $\tilde{n}$ is the complex index of refraction for each material in which the wave propagates. The complex index of refraction is given by,

Equation 33

$$\tilde{n} = n - ik$$

where the real part of the index, n, describes the refractive properties of the material, while the imaginary part of the index, k, describes attenuation of the incident wave. If a material is non-absorbing, $k = 0$ and $\tilde{n} = n$. The fraction of the incident wave that is reflected or transmitted can be determined using Fresnel coefficients. Two sets of Fresnel coefficients are developed for the two possible linear polarization components of the incident wave, defined as s and p polarizations. The p polarization refers to light in which the electric field oscillates parallel to the plane of incidence. The s polarization refers to light in which the electric field oscillates normal (90°) to the plane of incidence. The Fresnel coefficients for the reflection (r_s) and transmission (t_s) of s-polarized light are:

Equation 34

$$r_s = \frac{\tilde{n}_1 cos\theta_i - \tilde{n}_2 cos\theta_t}{\tilde{n}_1 cos\theta_i + \tilde{n}_2 cos\theta_t}$$

and

Equation 35

$$t_s = \frac{2\tilde{n}_1 cos\theta_i}{\tilde{n}_1 cos\theta_i + \tilde{n}_2 cos\theta_t}.$$

The Fresnel coefficients for the reflection (r_p) and transmission (t_p) of p-polarized light are:

19

Equation 36

$$r_p = \frac{\tilde{n}_2 cos\theta_i - \tilde{n}_1 cos\theta_t}{\tilde{n}_1 cos\theta_i + \tilde{n}_2 cos\theta_t}$$

Equation 37

$$r_s = \frac{\tilde{n}_1 cos\theta_i - \tilde{n}_2 cos\theta_t}{\tilde{n}_1 cos\theta_i + \tilde{n}_2 cos\theta_t}.$$

The total reflectance, R, and transmittance, T, of light at an interface is defined by the ratio

of the light intensity that is either reflected, I_r, or transmitted, I_t, to the intensity of the

incident light I_i.

Equation 38

$$R = \frac{I_r(\lambda)}{I_i(\lambda)}$$

Equation 39

$$T = \frac{I_t(\lambda)}{I_i(\lambda)}$$

The reflectance and transmittance of linearly polarized light can be determined using the

Fresnel coefficients. For s-polarized light:

Equation 40

$$R_s = |r_s|^2$$

and

Equation 41

$$T_s = \left(\frac{\tilde{n}_2 cos\theta_t}{\tilde{n}_1 cos\theta_i}\right) t_s^2.$$

For p-polarized light:

Equation 42

$$R_p = |r_p|^2$$

and

Equation 43

$$T_p = \left(\frac{\tilde{n}_2 \cos\theta_t}{\tilde{n}_1 \cos\theta_i}\right) t_p^2.$$

For unpolarized light, the reflectance is defined by:

Equation 44

$$R = \frac{1}{2}(R_s + R_p) = |r|^2.$$

According to the Fresnel coefficients, the reflectance from an interface depends on the angle of incidence, polarization of incident light, and the optical properties (complex refractive index) of the reflecting material. As a result, the peaks observed in IRRAS spectra can be both positive and negative. For example, when p-polarized light is incident on a material at angles less than the Brewster angle, the RA peaks are negative. If the angle of incidence is greater than the Brewster angle in this polarization, the peaks are positive. When s-polarized light is incident on a surface, RA peaks are negative regardless of the angle of incidence. For all IRRAS experiments described herein, spectra are acquired using unpolarized light at incidence angles slightly less than the Brewster angle. As a result, the positive and negative nature of the peaks observed is primarily due to the calculation of RA as given in Equation 30. In this case, positive peaks occur when the reflectivity of the reference is greater than that of the sample, $R/R_0 < 1$. Negative peaks occur when the sample reflectance is greater than that of the reference, thus $R/R_0 > 1$.

2.2 Instrumentation

2.2.1 Raman Instrument

The custom-built polarized Raman system is described in section 3.2.2 of this document. The description of the instrument is reproduced here for continuity of the introductory material. The Raman spectrometer used in this work consists of a diode-pumped continuous wave excitation laser (532 nm, 100:1 vertically (V) polarized, CrystaLaser) directly coupled to a Raman probe optical system (InPhotonics). Scattered light is collected using two independent fiber-optic cables which simultaneously collect the parallel (VV) and perpendicular (VH) polarized responses. The fiber optics are coupled to a spectrograph (IsoPlane 320, Princeton Instruments) using a 150 μm slit width and 600 g/mm grating (750 nm blaze). The two polarized signals are detected on separate regions of a LN$_2$-cooled CCD detector (Pylon 400BRX back-illuminated, Princeton Instruments). Spectra are collected by averaging 150 exposures using a 0.045 s exposure time. A diagram of the Raman system is presented in Figure 2.
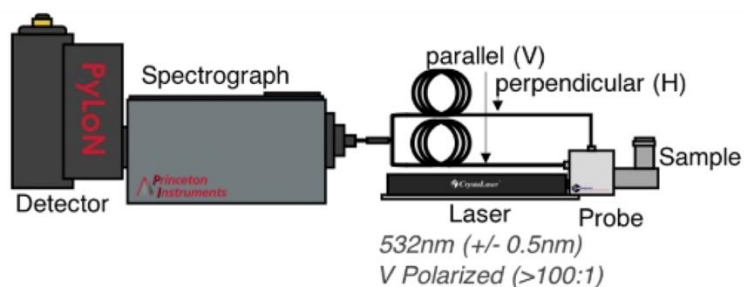
Figure 2. Schematic of the custom-built Raman system used in this work.

2.2.2 IRRAS Instrument

IRRAS spectra are acquired by equipping a commercial FTIR spectrometer with a lab-built array of mirrors that enables the IR beam to be directed onto the surface at the specified angle of incidence. IRRAS spectra were collected using a PerkinElmer Spectrum 3 FTIR. The lab-built mirror array consists of two gold-plated mirrors (2 in. diameter) mounted to a breadboard. In this setup, the unpolarized infrared light from the spectrometer is incident on the first mirror, which is angled such that the incident light is directed onto the liquid surface at a 48° angle relative to the surface normal. The light that is reflected off the liquid surface is collected with the second gold mirror, which directs the beam into the LN_2 cooled HgCdTe (MCT) detector. The liquid sample can be coupled to the IRRAS optical system in several ways including a Langmuir trough, a height-adjusted petri dish, and an isolated cell, which allows for gas-liquid experiments. Figure 3 depicts the IRRAS setup when coupled to a Langmuir trough such as in Enders, A.A.; Clark, J.B. et al. *Langmuir* 2023.
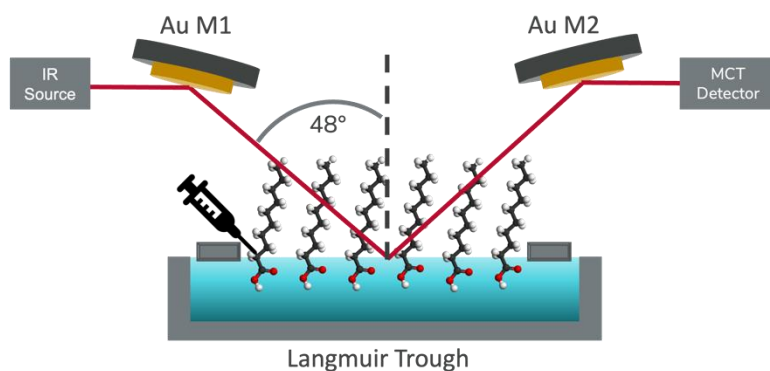
Figure 3. Depiction of the IRRAS mirror array sampling the air/water interface following the spreading of a fatty acid monolayer.

Chapter 3. Structural Evolution of Water-in-Propylene Carbonate Mixtures Revealed by Experimental Raman Spectroscopy and Molecular Dynamics
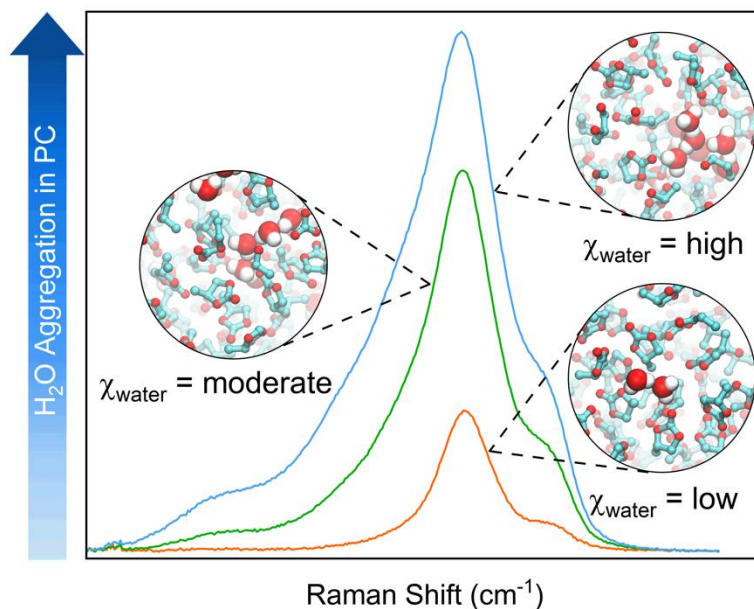
Figure 4. Graphical abstract showing that combined polarized Raman and MD simulation studies demonstrate that water undergoes increasing aggregation in mixtures with propylene carbonate as its concentration is increased.

3.1 Introduction

The structure and properties of water within complex environments is of fundamental interest due to its potential to reveal new insights into the dynamic hydrogen bonding network of water and its many anomalous bulk properties which have confounded the community for decades.[52,53] When water is limited in quantity and geometric

24

configuration by physical or chemical constraints, its properties often differ significantly from those of a bulk liquid.[517,16,54] It is necessary to understand how the properties of water are altered in these environments in order to establish the limits at which bulk properties begin to arise or break down. This knowledge aids in the understanding of the fundamental microscopic mechanisms that govern water's macroscopic properties.

There has been significant study of the structure of water in systems with well-defined boundaries such as in confinement within reverse micelles[17,55] carbon nanotubes,[56,57] metal-organic frameworks,[58,59] and silica pores[18]. However, the study of water in disordered, dynamic environments such as binary mixtures has been more limited.[60–65] Notable exceptions are water in ionic liquids, which have gained significant interest in recent years.[64–70] Studies of ionic liquid binary mixtures with water reveal nanoscopic aggregation of water within the solvent (i.e. formation of a nanoconfined "water pocket") that is strongly dependent on the chemical structure of the ionic liquid.[64–66,71] Using small angle x-ray and neutron scattering, Abe and coworkers found that the "water pocket" formed in the ionic liquid [C_4mim][NO_3] has slow orientational dynamics and weak hydrogen bonds due to the nanoconfined nature of the system.[65]

In contrast to studies of water in ionic liquids, studies investigating binary mixtures of dilute water dispersed in dipolar, aprotic, organic solvents are more limited.[60,62,72–77] Studies in the late 1960s showed that within partially chlorinated hydrocarbon solvents, water formed small clusters with itself (dimers to tetramers), but there was disagreement concerning the primary species.[76] In comparison to the previous study, Shultz and coworkers revealed that water exists as monomers in the non-polar solvent CCl_4 and that

that the rotational motion of the monomers is greatly restricted by the solvating environment.[78] In hydrogen bond accepting solvents such as amines and ketones, water self-association has been observed and formation of the trimer species has been proposed.[60,75] In such systems, water exists under dynamic confinement by the polar, aprotic solvents due to a balance of intermolecular interactions. The structural characterization of these binary mixtures provides information that is critical in multiple materials applications such as ion solvation in electrolyte solutions.[79–81]

Propylene carbonate (PC) is a commonly used solvent in lithium-ion batteries, where it is typically mixed with linear carbonates to provide optimal charge stabilization and transport.[81–89] One of the pitfalls of these electrolyte solutions is the hygroscopicity of PC, which can result in water contamination. This contamination causes hydrolysis of $LiPF_6$ to HF and significantly impedes battery performance.[90,91] Studies have also shown that the addition of PC or water to electrolyte solutions greatly impacts the ion conductivity, which in some cases is dictated by the types of ion pairs formed in solution.[92–96] It is still unclear how the addition of water to PC impacts the PC/Li ion pair formation and thus the conductivity. Therefore, it is critical to understand the solvation structure of water in PC.[84,88–91] PC has unique chemical and physical properties that make it a well-suited solvent for studies of water structure under dynamic confinement. PC has a high dielectric constant (64.40 at 25 °C) and dipole moment (4.94 D).[97] Unlike many other similar organic solvents, it cannot act as a hydrogen bond donor, only as an acceptor. As a result, some of the chemical complexity that exists in hydrogen bond donating solvents is removed, enabling simpler structural characterization.

The behavior of water in a binary solution with PC has been evaluated in two notable previous studies, yet there is disagreement between the proposed water structure. The first study by Grunwald and coworkers evaluated mixtures of PC and water in the concentration range 0-3.5 m ($\chi_{water} \leq 0.26$) using FTIR and ^{1}H NMR spectroscopies.[60] From this study, it was concluded that water primarily forms monomers and dimers when solvated in PC and that cyclic trimers or other highly coordinated species do not form. Then in a second study, Dei and coworkers used surface tensiometry, differential scanning calorimetry, and FTIR spectroscopy to investigate mixtures of PC and water in the molar ratio range of $0.041 \leq \chi_{water} \leq 0.33$.[62] In contrast to the former study, the authors claim that monomers and dimers are the primary species only under very limited water conditions ($\chi_{water} < 0.14$). Once the water concentration exceeds the threshold, the authors observe that water shifts from being fully solvated by PC to forming stronger solute-solute interactions in trimers structures, a finding that is inconsistent with the older work by Grunwald et al. In the present work, we expand the knowledge of water structure within PC beyond what has been accomplished using FTIR spectroscopy to help address the conflicting conclusions that have been reached in previous works. This is achieved by combining MD simulations with polarized Raman spectroscopy, a technique that provides complementary vibrational information to FTIR spectroscopy.

In the analysis of water's structure, vibrational spectroscopy is often employed due to its high sensitivity to the local environment of the molecule(s) being studied.[98–100] Raman spectra, as opposed to FTIR, provides more highly differentiable O-H spectral features given the same instrument resolving power due to the differing selection rules. It is

therefore highly suitable for observing subtle changes in water's hydrogen bond structure.[98,101] An additional advantage that Raman spectroscopy provides is the ability to observe polarized responses that result from local vibrational symmetry.[102] The analysis of such responses from PC enables the determination of its liquid structure, which was unclear in prior work that relied on FTIR peak shifts alone.[60,62]

In its bulk liquid state, water forms four hydrogen bonds in an approximately tetrahedral geometry, on average. These hydrogen bonds are highly dynamic and fluctuate on a picosecond timescale causing a distribution of configurations with varying bond strengths.[103,104] As a result, the O-H stretching vibrational bands are broad and complex to interpret due to their close overlap with one another. It is generally accepted that this convolution of bands is a result of several component bands that correspond to different hydrogen-bonded water assemblies.[62,68,99,100,103–109] Therefore, this region is commonly deconvoluted using multiple Gaussian sub-bands allowing for characterization of water structure under varying conditions.[68,98–100] Despite decades of research in this area, there is still much debate over the identity of the water assemblies that give rise to each sub-band.[68,69,98,100,101,105,109–112] For example, Sun and colleagues use five bands to fit the Raman O-H stretching band of bulk water. The bands are centered at 3041, 3220, 3430, 3572, and 3636 cm^{-1} and are assigned to the single donor-double acceptor (DAA), double donor-double acceptor (DDAA), single donor-single acceptor (DA), double donor-single acceptor (DDA), and free-OH water arrangements, respectively.[100,105] In contrast, studies of dilute water in ionic and dipolar liquids have deconvoluted the FTIR O-H stretching band into 3-5 Gaussians. These bands are assigned more generally to symmetrically and

asymmetrically solvated water molecules as well as free-OH stretching. The absolute positions of these bands are dependent on the identity of the solvent.[68,69,77]

Herein we present, to the best of our knowledge, the first Raman and MD simulation study of the liquid structure of water-in-propylene carbonate mixtures. We evaluate the structure of dilute water in PC as the concentration is increased from $\chi_{water} = 0.003$ up to saturation ($\chi_{water} = 0.296$). Analysis of the O-H stretching, and carbonyl regions of the Raman spectra reveals a hydrogen bond structure that is distinctly different from bulk water and highly concentration dependent. The noncoincidence effect (NCE) in the polarized carbonyl Raman band provides insight into structural changes in PC due to water solvation. Isotopic dilution spectroscopic experiments (10% HOD in D_2O) bridge the gap between experiment and simulations as well as highlight the extent of intramolecular vibrational coupling within water aggregates. Molecular dynamics simulation results find that water associates with itself in PC more than previous experimental inferences.[60,62] Our simulations also provide the first insight into the structure of water aggregates within PC and their compositional evolution. This study expands the fundamental knowledge of the behavior of limited water in complex solvation environments, which has applications in various fields including, materials and electrochemistry.

3.2 Methods

3.2.1 Materials and Sample Preparation

Solutions of dilute water dispersed in PC were prepared in the concentration range of $0.003 \leq \chi_{water} \leq 0.296$. These concentrations span the water-in-PC solubility range, stopping near the known miscibility gap ($0.33 \leq \chi_{water} \leq 0.95$ at 20 °C) of the two liquids.[62]

PC/water solutions were prepared by the incremental addition of ultrapure water (Milli-Q Advantage A10, resistivity 18.2 MΩ) to 3.2626 ± 0.0017 g of PC (Sigma-Aldrich, ≥ 99.7%, anhydrous) in a standard quartz cuvette (Starna, 10 mm path length) that was sealed using a cap equipped with a silicone gasket to provide an air-tight seal. To limit water contamination of the solvent, a single-use sterile syringe and needle were used to transfer PC from the septum sealed bottle directly to the cuvette for immediate use without further purification. Thus, the purity of PC can be reasonably assumed to be that reported by the manufacturer (purity ≥ 99.65%, water content by Karl Fischer titration ≤ 0.002 %).[113] To further limit excess water in the system, the cuvette was dried in a 150 °C oven for at least 12 hours before use.

Prior to the addition of water, the Raman spectrum of the pure PC sample was acquired. To achieve the desired molar ratio, water was then added to the PC sample incrementally until phase separation was reached. Phase separation occurred between a total of 240 and 260 μL of water added for all samples which corresponds to a water concentration in PC between χ_{water} = 0.29 and 0.31. The exact amount of water added to PC was determined by weighing the cuvette after each water addition (Mettler Toledo, XS104, ± 0.1 mg). Following each addition of water to PC, the sealed cuvette was manually shaken for at least 2 minutes then allowed to settle, undisturbed for 2 minutes prior to acquiring the polarized Raman spectra. Experiments were performed in duplicate at a room temperature of 20 °C.

3.2.2 Raman Spectroscopy

The custom-built Raman spectrometer used in the current work has been described previously.[114] Briefly, the Raman spectrometer consists of a diode-pumped continuous wave excitation laser (532 nm, 100:1 vertically (V) polarized, CrystaLaser) directly coupled to a Raman probe optical system (InPhotonics). Scattered light is collected using two independent fiber-optic cables, which simultaneously collect the parallel (VV) and perpendicular (VH) polarized responses. The fiber optics are coupled to a spectrograph (IsoPlane 320, Princeton Instruments) using a 150 μm slit width and 600 g/mm grating (750 nm blaze). The two polarized signals are detected on separate regions of a LN_2-cooled CCD detector (Pylon 400BRX back-illuminated, Princeton Instruments). Spectra are collected by averaging 150 spectra using a 0.045 s exposure time. Laser power stability was ensured by taking the Raman spectrum of pure water following every 5 sample spectra. Intensity variations in the OH stretching region of the water spectrum were < 0.6% for all experiments.

3.2.3 Computational Studies

In order to validate the molecular inferences concerning the structure of water/PC mixtures, a molecular dynamics simulation model was developed by collaborator Dr. David Limmer. Using a GROMOS forcefield with an SPC/E water model, we simulated water/PC mixtures across a range of compositions between dilute solutions and across the experimental miscibility gap.[115,116] All simulations were done under fixed number of molecules, temperature, and pressure using a Nose-Hoover thermostat and barostat.[117,118] The temperature and pressure were fixed to 298 K and 1 bar, respectfully. The number of

molecules was equal to 200 PC molecules plus the number of water molecules necessary to fix the mole fraction between 0.04 and 0.22. Standard periodic boundary conditions, Ewald summation treatment of electrostatic interactions and a 2 fs timestep was employed in all simulations with the covalent hydrogen bonds held rigid with RATTLE.[119] Each composition was simulated for 10 ns, with an initial 1 ns simulation at elevated temperature of 400 K and fixed volume to equilibrate the initial composition fluctuations. The specific forcefields were choosen because of their previous validation in related studies. The specific water model SPC/E has been previously shown to provide an accurate model for the electrostatic environments contributing to the inhomogenious vibrational line shapes[120–122] and SPC/E GROMOS mixtures are able to reproduce experimental trends in solvation thermodynamics.[123]

3.3 Results and Discussion

It is well known that the liquid structure of water is highly sensitive to its environment, yet there is still much debate over the microscopic mechanisms that govern water structure, particularly within systems where water is the solute. The aim of this study was to utilize a combined computational and experimental Raman approach to determine how dilute water partitions and interacts within a propylene carbonate (PC) solvent environment as water is increased up to the saturation limit. Structural changes within PC induced by the addition of water were also evaluated.

3.3.1 Raman Spectroscopy

The polarized Raman spectra of PC solutions were acquired as the water concentration was increased from a mole ratio of $\chi_{water} = 0.003$ to the saturation point

(phase-separation) at χ_{water} = 0.296. Particular attention is paid to the O-H stretching (3000 – 3800 cm^{-1}) and carbonyl regions (1720 – 1820 cm^{-1}) to determine water structure. The O-H stretching region consists of a broad band resulting from the population distribution of hydrogen-bonded water assemblies, which are expected to evolve as more water is added to the system.[18,55,98,99] Deconvolution of the O-H stretching band into Gaussian sub-bands allowed for the characterization of water structure. The carbonyl band revealed interactions of water with the solvating environment and developed a complete picture of how the PC bulk structure evolves to accommodate the solvation of water molecules.

3.3.2 Water Structure

The O-H stretching region of the PC/water Raman spectra after removing spectral contributions of pure PC through pre-processing is depicted in Figure 5. Further discussion of the spectral pre-processing procedure is presented in Appendix A (see also Figure 31 & Figure 32). These results demonstrate that the O-H stretching band increases in intensity and broadness as the water concentration is increased. It is difficult to determine the solvation structure of water from these spectra without further deconvolution of the hydrogen bonded sub-structure, therefore a Gaussian fitting was applied to this region. The fitting procedure is described in Appendix A and the converged parameters are included in Table 2 and Figure 33.
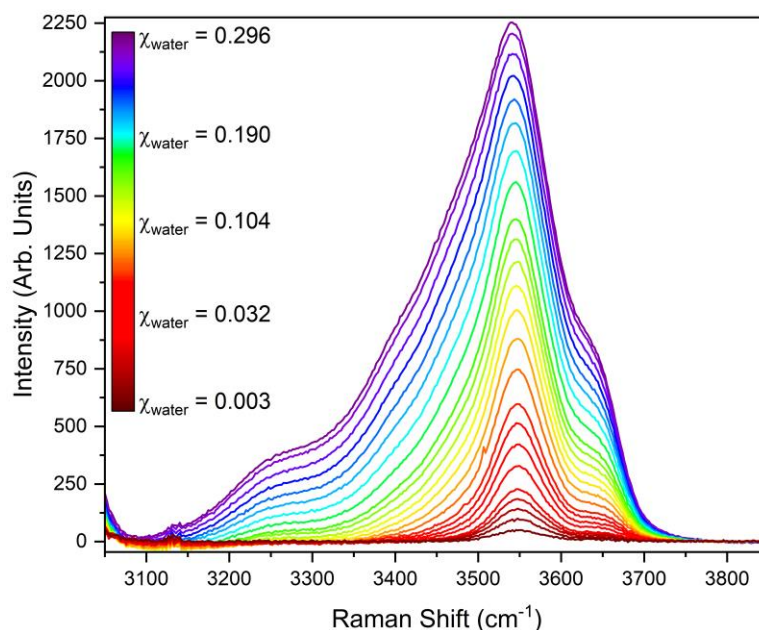
Figure 5. Raman spectra (VV polarization, O-H stretching region) of PC as water concentration is increased from 0.003 mole fraction (red) to 0.296 mole fraction (violet). Spectra demonstrate that O-H stretching band increases in intensity and broadness as water is added to PC.

The number of Gaussian bands required for the fit was dependent on water concentration. In the low water concentration spectra (χ_{water} < 0.091), only three Gaussian bands are required for the fit. These bands are centered at approximately 3480, 3550, and 3643 cm^{-1}. A representative spectrum for the low water concentrations (χ_{water} = 0.013) is plotted in Figure 6a. Based on literature of aqueous interfaces and confined water, the highest frequency Gaussian, centered at 3643 cm^{-1}, is assigned to dangling-OH groups (also referred to as "free-OH" in previous publications).[124–130] These O-H groups are pointed towards the solvating PC molecules, but are not participating in a hydrogen bond. The dangling-OH vibrational band arising from the hydration shells of dissolved nonpolar groups has been reported to occur at ~3660 cm^{-1}.[124,126] In our spectra, this band is shifted to lower energy due to the solvating dielectric environment.[68]

34

Based on previous water cluster and dilute water studies, the second and third Gaussians, which occur at ~3550 and 3480 cm^{-1}, respectively, are assigned to "partially coordinated" water species.[62,77,100,131,132] The water molecules that make up these groups form between one and three hydrogen bonds, but still do not form the fully coordinated, tetrahedral structure.[62,100] The partially coordinated water population can be further classified based on the degree of hydrogen bonding.[105,124,131,133] Evidence for this is provided by Suhm and coworkers who assigned the 3550 and ~3430 cm^{-1} bands in the FTIR spectrum of thermally excited water clusters to the trimer and tetramer water species, respectively.[131] Similar band positions were observed by Dei and Grassi in the FTIR spectra of dilute water in PC. The band observed at 3570 cm^{-1} was assigned to "multimer water" that is weakly connected to its environment. Additionally, they assigned the band centered at 3450 cm^{-1} to "intermediate water" that is moderately coordinated to other water molecules, but still has distorted hydrogen bonds.[62] Based on these studies, it is clear that the band we observe at 3550 cm^{-1} results from water molecules with low coordination and the band we observe at 3480 cm^{-1} results from water that is more coordinated in comparison. Therefore, we refer to the 3550 and 3480 cm^{-1} band populations as "low coordination" and "moderate coordination" water, respectively. Here, we choose to use broad language to describe the two center sub-bands to avoid speculating on the types of water aggregates formed in PC, which we cannot determine with spectra alone. These aggregates will be further explored using MD simulations.

Beginning at χ_{water} = 0.091 up to the saturation point, a fourth Gaussian is needed for the fit. The final and lowest frequency band is centered at ~3260 cm^{-1}. Based on well-

established literature of bulk water and clusters, this band is assigned to water that forms four hydrogen bonds in an approximately tetrahedral geometry.[18,100] In water clusters, this peak is only observed for hexamers or larger cluster sizes.[131] To align with our chosen terminology, we refer to this population as "full coordination" water. The full coordination water band can be observed in Figure 6b, where a representative spectrum for the high water concentrations ($\chi_{water} = 0.232$) is plotted.

To validate the peak assignments for the deconvoluted OH-stretching sub-bands, we considered the extent of intermolecular vibrational coupling for each of the sub-bands. This was achieved through isotopic dilution, where 5% H_2O in D_2O (10% HOD) was added incrementally to PC instead of pure water. As a result, the O-H stretching mode is decoupled and can be used as a more accurate reporter of water structure.[109] The spectra of dilute O-H in PC/D_2O mixtures was deconvoluted in the same manner as the PC/H_2O spectra and the results are plotted in Figure 34 in Appendix A. To estimate the relative degree of vibrational coupling for each water assembly observed, the intensity ratio of each sub-band to the highest intensity sub-band (low coordination, ~3550 cm^{-1}) is compared before and after decoupling at a constant water concentration. In the PC/H_2O spectrum, the intensity ratios for the moderate coordination at ~3480 cm^{-1} and dangling-OH band at 3643 cm^{-1} are 1.02 and 0.38, respectively. In the decoupled spectrum, these ratios are 0.58 and 0.33, respectively. Upon removal of vibrational coupling, the relative intensity of the moderate coordination water compared to the low coordination decreases significantly whereas the relative intensity for the dangling-OH decreases only slightly. This demonstrates that the water assembly responsible for the band at ~3480 cm^{-1} experiences

more intermolecular vibrational coupling and is therefore more coordinated than those giving rise to either the ~3550 cm^{-1} or the 3643 cm^{-1} bands. Thus, our peak assignments of increasing water coordination with decreasing frequency are supported. The intensity ratio for the 3260 cm^{-1} band in the PC/H$_2$O spectrum is 0.18. This band did not have enough intensity in the decoupled spectrum to be resolved from the PC band at 3220 cm^{-1}, so an intensity ratio was not able to be obtained. However, the lack of intensity for this band in the decoupled spectrum indicates that this assembly does experience some degree of coupling and further supports our assignment. Comparison of the low (Figure 6a) and high (Figure 6b) water concentration deconvolutions reveals that the largest spectral changes due to increasing water concentration occur for the moderate and full coordination water species. The fully coordinated water peak, which is initially not present, is observed as water is added to the system. The moderate coordination water peak significantly increases in broadness and intensity, accounting for much of the changes observed in the entire O-H stretching region. The same trends were observed when the ATR-FTIR spectra of the PC/water mixtures, taken to supplement the Raman data, were deconvoluted in the same manner (see Appendix A Figure 35 & Figure 36).
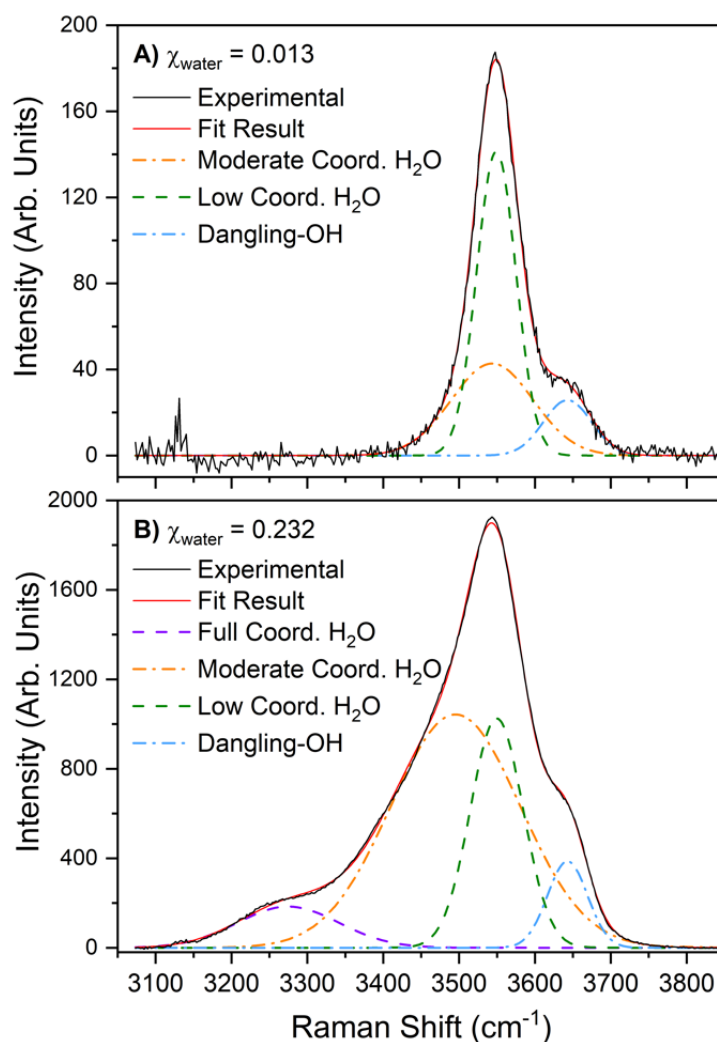
Figure 6. Gaussian deconvolution of experimental Raman O-H region for water concentrations χ_{water} = 0.013 (A) and 0.232 (B). Experimental (black) and fit (red) spectra are plotted with solid lines. Dashed lines represent Gaussian bands used to fit experimental spectra. Comparison of (A) and (B) reveals that the full coordination H_2O arrangement does not occur in PC when χ_{water} < 0.091.

Analysis of the individual deconvoluted Raman bands as a function of water concentration (Figure 7) allowed for further understanding of how the water structure in PC evolves. Upon the addition of water, the full coordination band (Figure 7a) increases in intensity and shifts significantly (Δv = −70 cm^{-1}) to lower frequencies (red-shifts). Similarly, the moderate coordination band (Figure 7b) increases in intensity and red-shifts

($\Delta v = -53$ cm^{-1}). The shifting of vibrational bands to lower frequency as a function of concentration is attributed to the strengthening of hydrogen bonds or other intermolecular interactions with the oscillator. Moreover, the O-H stretching region in Raman spectra has been shown to be sensitive to the degree of tetrahedral order within water, where the band shifts strongly to lower frequencies as the tetrahedral order is increased.[134] The observed red-shifts in the moderate and full coordination bands are consistent with the formation of ordered hydrogen bond configurations which have increasing tetrahedral character and stronger bonds.

The low coordination (Figure 7c) and dangling-OH (Figure 7d) bands behave similarly as the water concentration is increased. Both bands increase in intensity as a result of an increase in the total water molecules in the system. These Gaussian bands also do not undergo strong frequency shifts. The low coordination band increases in frequency (blue-shifts) by a total of 2 cm^{-1}. This can be attributed to intrinsic error in the fitting analysis or could be indicative of subtle weakening of the hydrogen bonds for this species. The frequency of the dangling-OH band did not change appreciably between the highest and lowest water concentration studied; therefore, it was held constant for all subsequent fittings (see Appendix A). The fact that the peak positions of the low coordination and dangling-OH bands do not change appreciably indicates that the water species that make up these populations do not undergo significant structural changes as the water concentration is increased.
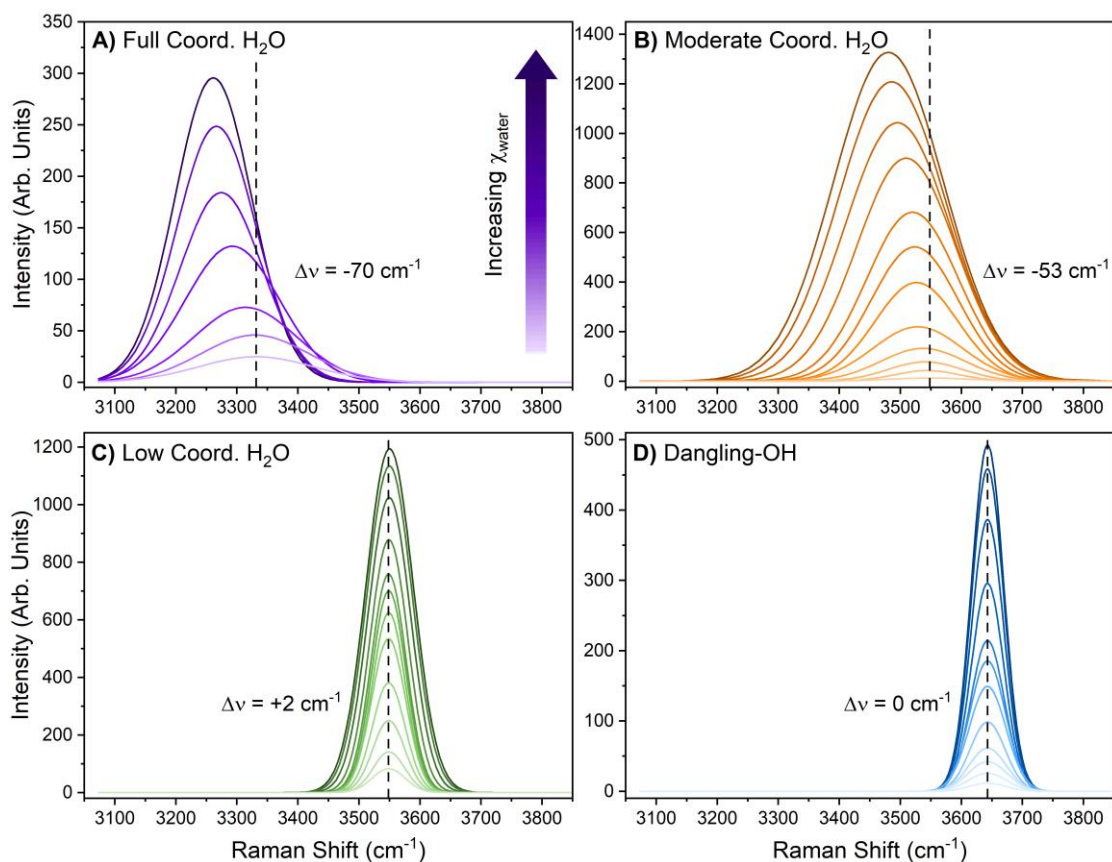
Figure 7. Evolution of the deconvoluted Gaussian bands as the water concentration in PC is increased. Each band corresponds to a different hydrogen bonded population of water; full coordination (A, violet), moderate coordination (B, orange), low coordination (C, green), and dangling-OH (D, blue). Darker colors correspond to higher water concentrations and dashed reference lines are set at peak position for lowest water concentration. The moderate and full H_2O bands undergo the largest peak shifts as the water concentration in PC is increased.

The present analysis of the Raman O-H stretching region assumes that water exists within one of four populations based on its hydrogen bonding state: dangling-OH, low coordination, moderate coordination, or full coordination. The O-H transition moment strength is assumed to remain constant across the individual solutions, therefore it follows that the total area of the O-H stretching band is the sum of the areas of the deconvoluted bands attributed to the different water population. Taking this into account, we calculated the percent of the total area taken up by the individual water populations as a function of

water concentration. In Figure 8, the percent of the total O-H stretching area taken up by each Gaussian is plotted as a function of water mole fraction. This plot demonstrates how the relative concentration of the water populations change as water is added to PC.

At the lowest water concentrations in PC, the low coordination population is present in the highest relative concentration. As water is added, the concentration of the low coordination state decreases sharply and levels off around $\chi_{water} = 0.20$ with a total decrease of 41%. Correspondingly, the moderate coordination population sharply increases in relative concentration as water is added. The total increase in the contribution of this band is 34%. The inverse trend in the relative concentration of the low and moderate coordination states demonstrates a shift in hydrogen bond structure as water is added to PC. Under very dilute conditions, water molecules exist primarily in low coordination states and do not interact strongly with one another. As water concentration is increased, water structure shifts and a greater population of water exists in moderate and full coordination states. The leveling of the relative concentration curves in Figure 8 indicates that this shift in structure is complete at $\chi_{water} = 0.20$.

The full coordination and dangling-OH populations do not experience significant changes in relative concentration. The full coordination state is not present until $\chi_{water} = 0.091$ is reached due to the low intensity of this band at more dilute concentrations. This band undergoes an overall relative concentration increase of 9%, which indicates that a larger fraction of the total water molecules exists in the most coordinated, tetrahedral state. This is only possible if water is interacting strongly with itself and forming aggregates larger than hexamers.[20] The relative concentration of the dangling-OH population remains

approximately constant at 8%. This concentration of dangling-OH is higher than in bulk water where it is ~3%.[100] We conclude that the solvating PC environment yields a water hydrogen bonding structure that is disrupted from typical bulk water organization. Instead, PC supports a higher concentration of dangling-OH groups.
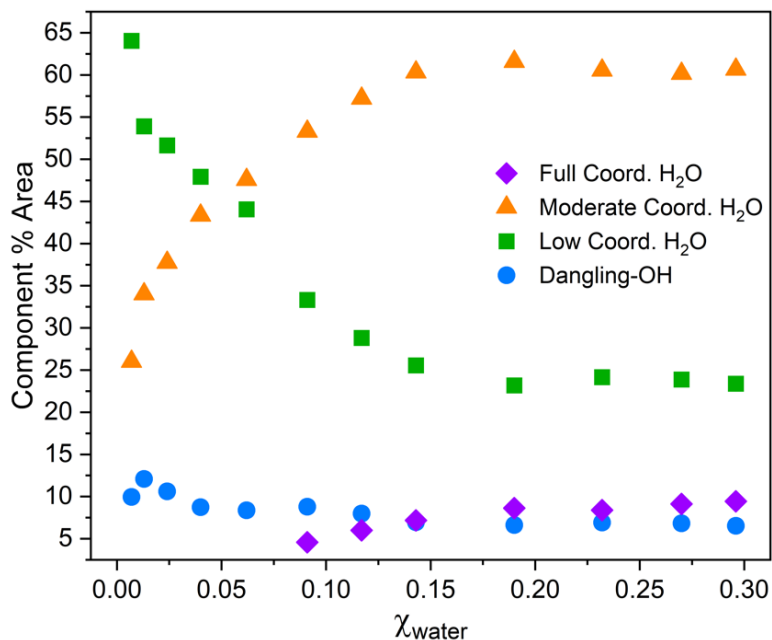
Figure 8. Percent of the total O-H stretching area taken up by each Gaussian band as a function of water concentration. When analyzing a single water concentration, the component % area of each sub-band can be interpreted as the relative concentration of each water arrangement.

Based on the observed changes to the hydrogen-bonded sub-structure, we conclude that at low concentrations of water in PC, water does not self-associate to an appreciable extent. Instead, it is primarily solvated by weaker intermolecular interactions with PC. The presence of the 3480 and 3550 cm^{-1} bands at the lowest water concentration spectra suggest that a fraction of water molecules in PC form small aggregates such as dimers up to potentially tetramers and pentamers. We also conclude that concentrations above $\chi_{water} = 0.091$, water self-associates to a greater extent, forming relatively large aggregates within the PC environment. The presence of the fully coordinated water peak indicates that a

significant portion of clusters formed have increasing tetrahedral order and must be hexamers or larger. In contrast to previous conculsions,[60,62] we observe a gradual transition from mostly solvated water molecules to primarily aggregated water molecules in PC.

Using molecular dynamics (MD) simulations carried out by collaborator Dr. David Limmer, we have quantified the degree of water clustering in PC by computing the average number of hydrogen bonds between water molecules as a function of bulk composition. Example snapshots from the MD simulations are shown in Figure 9a. These characteristic configurations show that water is well dispersed in the majority PC fluid. To accomplish this, we have employed a geometric criteria from Luzar and Chandler[135] for defining a hydrogen bond (n_{HB}) as an oxygen-oxygen separation distance of less then 3.5 Å and an angle between the oxygen-oxygen displacement vector and the oxygen-hydrogen bond vector as less then 30°. The results of these calculations are shown in Figure 9b where we enumerate the probability $P(n_{HB})$ of both the number and type of hydrogen bond. Specifically, we have differentiated molecules that are double hydrogen bond donors (DD), double acceptors (AA), single acceptor-single donors (DA), or double-donor single acceptors (DDA). At $\chi_{water} = 0.04$, water exists as a monomer 70% of the time, with the probability of dimers and trimers falling along Poisson statisics. At elevated water concentrations, the mostly likely structure becomes chains of water molecules each with two hydrogen bonds, one donated and the other accepting. The number of three and four coordinated water remains low, totalling only a combined 25% of solubilized water at the highest mole fractions considered, $\chi_{water} = 0.22$. These basic trends agree qualitatively with those in Figure 8 from the Gaussian deconvolution of the experimental Raman spectra.
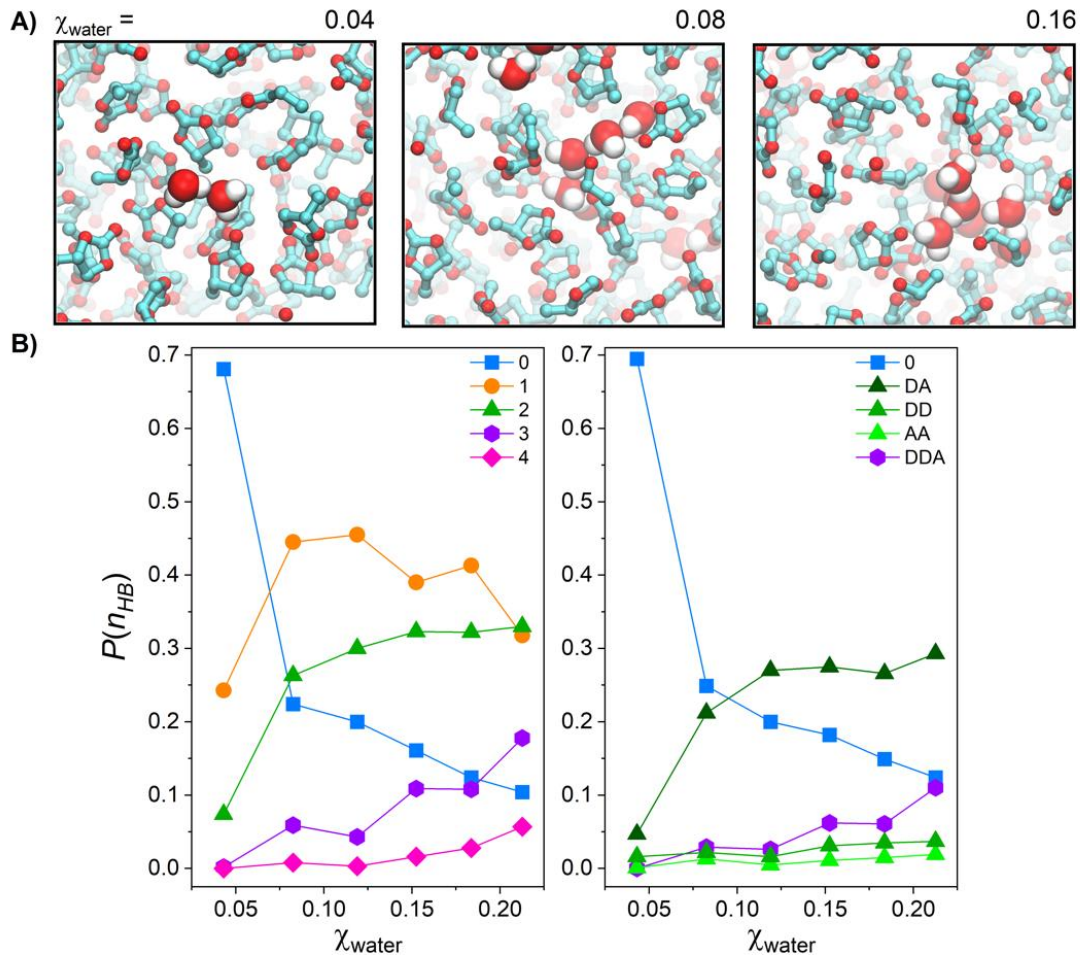
Figure 9. Molecular dynamic simulations of water-PC mixtures. A) Characteristic snapshots at different compositions. B) Probability of different hydrogen bond arrangements. Results demonstrate that water associates with itself to a greater extent at higher concentrations.

As inferred from the experimentally deconvolved Raman spectra, the simulations confirm that the O-H stretching frequency is determined by a large extent to the degree of hydrogen bonding between water molecules. To calculate the Raman spectra, we have employed a frequency map based approach.[108] Specifically, in the purely inhomogeneous broadening limit, the Raman lineshape is a probe of the local electric field, ξ along the O-H bond vector.[136] This follows from the a Stark effect and first order perturbation theory between the oscillator and the surrounding bath such that the frequency shifts are given by

$\omega - \omega_o = Q\xi$, where ω_o and Q are taken here as empirical parameters determined to best fit the lineshape. Specifically, a proceedure that has been employed by Geissler and coworkers in pure water and aqueous solutions, is to map the Raman lineshape to the distribution of electric fields acting on the hydrogen in the direction of the O-H bond vector.[121] To validate this approach, we have plotted in Figure 10a the distribution of electric fields on top of the experimentally measured O-H stretching region of the Raman lineshape for diluted HOD in D_2O/PC mixtures. Using diluted HOD in D_2O, allows us to decouple the oscillators, and mitigate effects from delocalization of the vibrations.[109,120,137,138] As observed in past simulations,[122] this simple classical perspective on the Raman lineshape allows us to identify specific molecular structures that give rise to features in the relatively broad lineshape.

The simulation and experimental lineshape for dilute HOD match well over the compositions considered, with an asymmetric shape rising quickly at high fequencies and falling slowly at low frquencies. Notably sharp features in the H_2O in PC lineshape at 3250 cm^{-1} and 3650 cm^{-1} are less pronouced in the diluted HOD spectra and the corresponding simulations, suggesting that some of the structure results from delocalization of the oscillation. Upon increasing the concentration of water, the simulated spectra from the mapped frequencies in Figure 10b show the same basic trends as those observed experimentally, namely an increased broadening in the form of a lower frequency or, equivalently, a larger magnitude electric field. In the simulations, this growing mode at lower frequency is identified as the O-H oscillator donating a hydrogen bond to another water molecule. No other motif strongly correlates with the increasing intensity, as only

45

local hydrogen bonding produces such drammatically different local electric fields (see

Appendix A Figure 38).
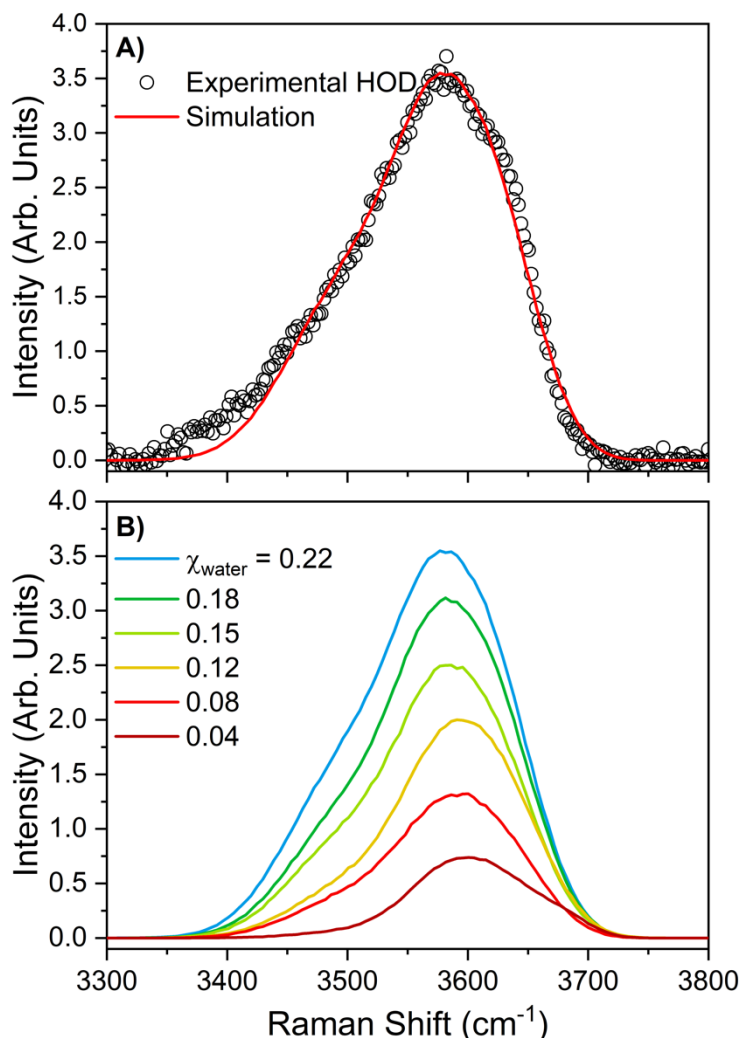
Figure 10. Raman spectra (O-H stretching region) from molecular dynamics simulations of dilute HOD. A) Comparison of experimental spectra and frequency mapped spectra for 0.22 mole fraction. B) Simulated spectra as water concentration is increased from 0.04 mole fraction (red) to 0.22 mole fraction (blue).

3.3.3 Propylene Carbonate Structure

To gain insight into the effect that the addition of water has on the bulk structure of

PC, the carbonyl region of the experimental and theoretical spectra were analyzed. The

experimental carbonyl stretch Raman spectra as a function of water concentration are

presented in Figure 11 with the theoretical spectra plotted in the inset. The carbonyl peak

for pure PC has been reported to occur in the Raman spectrum at approx. 1780 cm^{-1}, with

a Fermi resonance band causing a shoulder on the high-frequency side.[81,85,139] Here, we

observe the carbonyl band for pure PC at 1779 cm^{-1}, where it undergoes a small red-shift

(Δv = ~2 cm^{-1}) and an overall decrease in intensity as the concentration of water is

increased (Figure 11). The decrease in intensity of the band is a result of the dilution of PC

that occurs upon each addition of water. As described above, the red-shift that this band

undergoes is indicative of strengthening intermolecular interactions with the oscillator. The

carbonyl band in vibrational spectra has previously proven to be a sensitive probe for

hydration structure, producing significant shifts (upwards of Δv = 20-30 cm^{-1}) upon

changes in hydration.[48,140,141] As a result, we assert that the water concentration-dependent

red-shift of the carbonyl band is due to the formation of weak water-PC hydrogen bonding

at this molecular site. These are in agreement with the MD simulations, where the C=O

stretch is computed in an analogous manner as those of the O-H stretch in water, using the

electric field acting in the direction of the C=O bond vector.
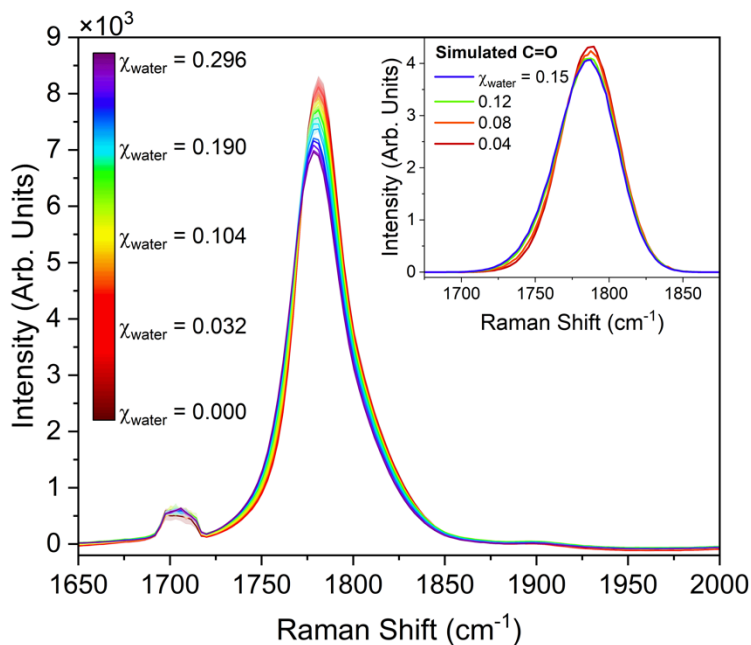
Figure 11. Raman spectra (VV polarization, carbonyl stretching region) of PC as water concentration is increased from $\chi_{water} = 0$ (red) to 0.296 (violet). Band structure occurring at ~1710 cm^{-1} is a result of an artifact in the Raman optical system and does not correspond to molecular vibrations. Theoretical C=O stretching spectra are plotted in the inset.

Further information on structural changes in PC can be gained through consideration of the polarized Raman spectra in terms of the noncoincidence effect (NCE). The noncoincidence effect refers to the frequency difference between the isotropic and anisotropic components of a polarized Raman band ($\nu_{NCE} \equiv \nu_{isotropic} - \nu_{anisotropic}$), which originates from resonant vibrational energy transfer between molecules that are intermolecularly coupled (e.g. by hydrogen bonds, permanent dipole moments, etc.).[102,142–145] Coupling between dipoles in pure propylene carbonate produces a relatively large and positive NCE in the carbonyl band, typically ~10 cm^{-1}.[81,144] In prior studies by the Allen lab and others, the NCE has been used to determine structural organization changes in dipolar liquids due to ion solvation.[81,114,142,143,146] For example, Giorgini and coworkers

demonstrated that the addition of mono- and divalent cation salts to acetone produced large, negative carbonyl NCEs due to solvent clustering around the cation.[142,146]

In this study, we have calculated the isotropic (I_{iso}) and anisotropic (I_{ansio}) components of the carbonyl stretching band using the VV and VH polarized Raman spectra and the following equations: $I_{iso} = I_{VV} - \frac{4}{3}I_{VH}$ and $I_{aniso} = \frac{4}{3}I_{VH}$.[102] In Figure 12, the carbonyl band NCE resulting from pure PC (Figure 12a) and from the PC solution with the maximum water concentration, χ_{water} = 0.296, (Figure 12b) are compared. The addition of water to PC causes a total NCE decrease of 0.5 cm^{-1}, which is consistent with the formation of weak hydrogen bonds between the carbonyl of PC and water.[143] The observed change in NCE as water is added to PC is small in comparison to previously reported carbonyl NCE changes in propylene carbonate as well as in other similar solvents.[81,139,146] Thus, we conclude that the bulk structure of PC is not significantly perturbed by the addition of water up to the solubility limit.

The symmetric and asymmetric ester stretching bands were also analyzed to provide additional information on bulk PC liquid structure as a function of water concentration. The polarized and depolarized Raman response of the ester bands is plotted in Figure 37 in Appendix A. We find that the addition of water to PC causes a small blue-shift for both ester bands where Δv is 0.50 and 0.42 cm^{-1} for the symmetric and asymmetric bands, respectively. This shift likely indicates a slight weakening of ester intermolecular forces as water is added, which supports the conclusion that the PC-water interaction occurs primarily at the carbonyl site and not the ester oxygens. Analysis of the NCE for the ester bands also supports this conclusion. The NCE for both ester bands remains

relatively unchanged from the pure PC spectrum to the highest water concentration spectrum, only changing by < 0.08 cm^{-1}. Based on our analysis of the polarized Raman response of PC molecules as a function of water concentration, we conclude that the carbonyl is the primary site of interaction with water and that this interaction does not cause the bulk PC liquid structure to rearrange to accommodate water solvation.
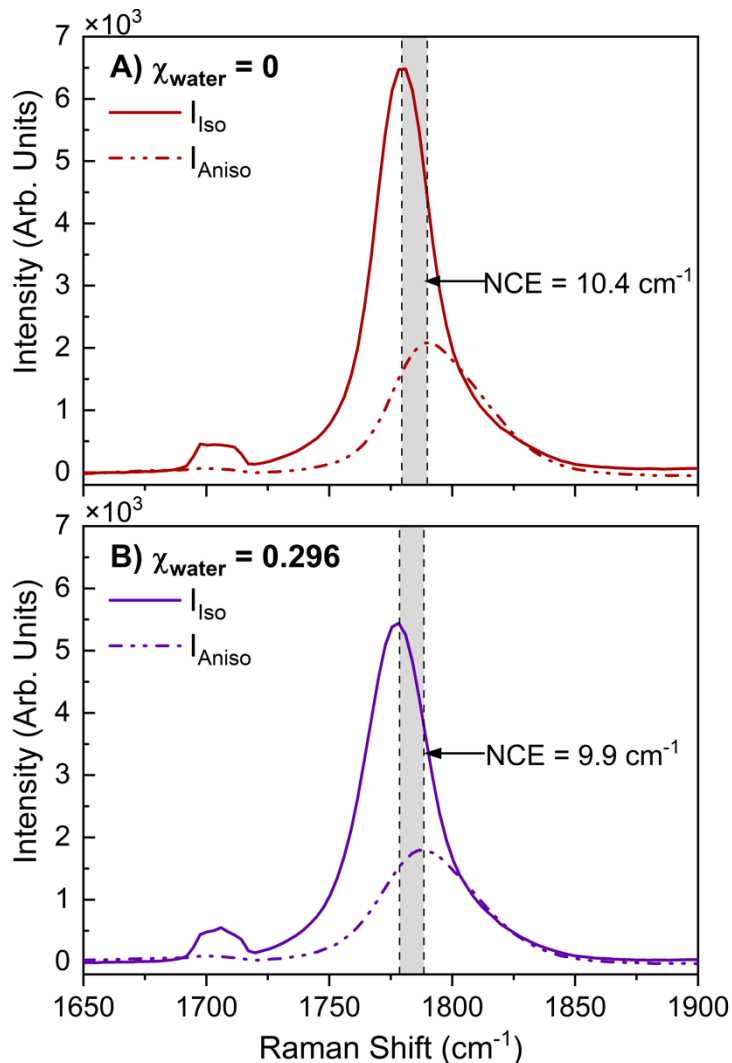
Figure 12. Isotropic (solid line) and anisotropic (dashed line) components of the polarized carbonyl Raman band for pure PC (A, red) and PC with water added to a mole fraction of 0.296 (B, violet). Dashed reference lines are included at the carbonyl peak position (determined by Gaussian fitting) for the isotropic and anisotropic components. The shaded gray area represents the noncoincidence effect (difference in isotropic and anisotropic peak positions) for each solution.

3.4 Conclusions

In this work, we characterize water concentration-dependent structural changes of a PC/water binary system using polarized Raman spectroscopy and molecular dynamics simulations. Gaussian deconvolution of the OH region in the experimental spectra reveals a water hydrogen-bond structure that consists of either three or four sub-bands that are assigned based on the degree of hydrogen bonding. For water concentrations in PC less than $\chi_{water} = 0.091$, dangling-OH, low coordination, and moderate coordination states are observed. Above this concentration, a fourth sub-band is observed, which corresponds to fully coordinated, tetrahedral water. As evidenced by the evolution of the water hydrogen bond sub-bands, water is primarily solvated by PC under dilute conditions and does not tend to form aggregates. Increasing the water concentration leads to an increase in tetrahedral water structure and indicates that water exists primarily in aggregates at higher concentrations. MD simulation results support this conclusion as well as provide additional insight into the size and type of aggregates formed. Simulations of the system where $\chi_{water} = 0.04$ reveal that water exists as monomers 70% of the time, with dimers and trimers accounting for the remaining conformations. Interestingly, the simulations find that the mostly likely water structure at elevated concentrations is chains of water molecules, each with two hydrogen bonds. Experimental and simulation results show that the hydrogen bond structure of water is distinctly different from the bulk at all concentrations, where the presence of three and four coordinate water is lower and dangling-OH is higher in comparison to bulk. The bulk structure of PC is not significantly perturbed by the addition of water as demonstrated by a change in carbonyl NCE of only 0.5 cm^{-1} from pure PC to

the highest water concentration in PC. Overall, the addition of water to PC results in a relatively unperturbed PC structure, yet water structure evolves in a highly concentration-dependent manner. This yields a distribution of hydrogen bonded states including linear chains as well as structures with more tetrahedral local order.

Chapter 4. Interfacial Carbonyl Groups of Propylene Carbonate and Diethyl Sebacate Facilitate the Reversible Binding of Nitrogen Dioxide

Clark, J.B. and Allen, H.C. In Review. *Phys. Chem. Chem. Phys*. 2024.
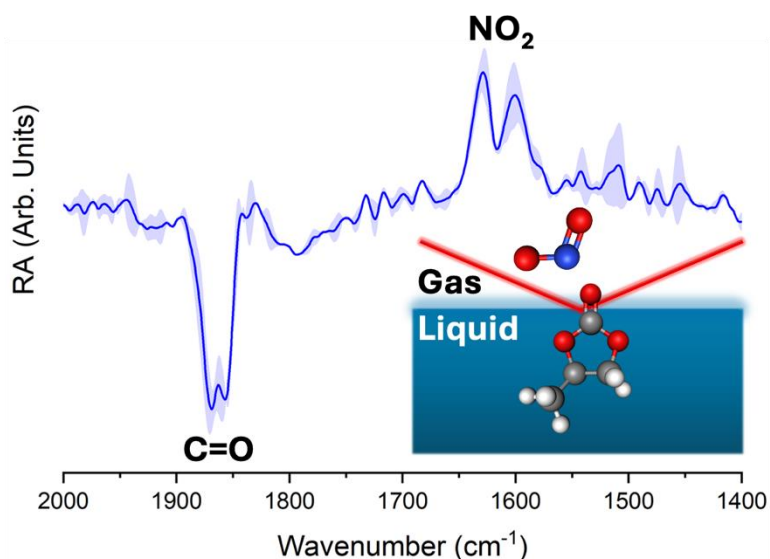
Figure 13. Graphical abstract showing that the carbonyl group of the organic liquid, propylene carbonate, facilitates the reversible binding of NO_2 molecules at the interface as demonstrated through infrared reflection-absorption spectroscopy experiments.

4.1 Introduction

Nitrogen dioxide (NO_2) is an anthropogenic atmospheric pollutant that is ubiquitous in urban environments. It is the dominant component of NO_x ($NO_x = NO + NO_2$), which in the presence of carbon monoxide and/or volatile organic compounds provides the only known anthropogenic reaction pathway for the production of tropospheric ozone (O_3).[1,2] Gas-phase reactions of NO_2 in the atmosphere have been well studied and are known to have important implications for overall air pollution and

climate.[1,2] However, consideration of these gas-phase chemical processes alone has led to inaccuracies in atmospheric modeling and predictions such as in the over prediction of HNO_3 concentrations.[147,148] Such discrepancies have been shown to result, at least in part, from the critical role that NO_2 plays in the heterogeneous chemistry occurring at the surface of aerosol particles.[19,20,22,148–153]

Heterogeneous chemistry involving aerosol particles can dramatically impact aerosol properties including their morphology, ability to act as cloud condensation nuclei, and radiation scattering efficiency.[2] The complexity of aerosol reactivity and dynamics makes these systems difficult to study experimentally, thus the breadth of these reactions and the mechanisms governing them remain an area of great research interest. In a 2021 study, Abbatt and Liu showed that the formation of sulfate aerosol particles is accelerated under polluted conditions due to the oxidation of SO_2 by NO_2 at aqueous aerosol interfaces.[19] Interfacial reactions of NO_2 also provide a pathway for reservoir species of highly-reactive radicals such as OH and Cl to be formed. For example, the reaction of NO_2 with chloride salts in marine aerosol and at the air/sea interface forms the Cl reservoir species, NOCl.[20,21] Interfacial trapping of NO_2 at air/water interfaces has also been identified as an important step in the formation of HONO, a reservoir of OH radical.[22]

NO_2 not only plays a role in the heterogeneous chemistry of aqueous aerosol but also impacts the formation and composition of organic aerosol[23–26,154,155] Organic aerosol comprises a significant portion (20-90%) of all submicron aerosol in the troposphere.[10–12] This class of aerosol can either be directly emitted into the atmosphere as primary organic aerosol or formed through the oxidation of volatile organic compounds to become

secondary organic aerosol (SOA). Recent studies have shown that the formation and composition of SOA can depend strongly on NO_x conditions.[23–27] Shiraiwa and coworkers found that α-pinene and naphthalene SOA generated under low NO_x conditions favors the formation of OH radicals and superoxide. The formation of these species was significantly reduced under high NO_x conditions where the formation of nitroaromatics and other organic nitrates were favored.[24] NO_x concentrations can also alter the mechanism of oxidation by which SOA is formed as demonstrated by Lin and coworkers who identified an epoxide intermediate in the formation of isoprene SOA under high NO_x conditions.[23]

Another area that relies on the heterogeneous interfacial chemistry of NO_2 is the development of technology to detect and remove NO_2 from the atmosphere. Exposure to high levels of NO_2 pollution have been linked to many negative health outcomes including lung cancer, heart problems, and asthma,[156–159] therefore accurate detection and efficient removal of NO_2 from the atmosphere is imperative. Materials including zeolites,[160,161] activated carbon,[162–165] silica,[166] and metal-organic frameworks[167] have shown promise in trapping NO_2 from exhaust streams. Adsorption of NO_2 on each of these substrates depends on both the physical structure and chemical moieties at their interfaces. Activated carbon interfaces provide a low-cost method that repurposes organic waste products like sawdust into NO_2 sorbent material.[162–164] Carbon surfaces can be functionalized to optimize the surface sites that will promote the greatest NO_2 adsorption.[164,165] Studies of NO_2 adsorption on sawdust activated carbon surfaces linked an increase in NO_2 adsorption capacity to an increase in surface oxygen groups.[162,163] In the development of high-performance NO_2 sensors, interactions of NO_2 with surface oxygen groups have resulted in enhancement of

55

sensing properties.[168,169] One type of organic field-effect transistor based sensor utilizing poly(methyl methracrylate) and silk fibroin as the dielectric bilayer demonstrated superior sensing abilities compared to sensors with only poly(methyl methracrylate) as the dielectric. This performance enhancement was attributed to strong interactions of NO_2 with OH groups on the silk fibroin component of the dielectric.[169]

From the studies summarized here, it is clear that the presence of oxygen-containing functional groups strongly impacts the heterogeneous chemistry of NO_2 at a variety of interfaces. This research aims to provide new fundamental information on the interfacial behavior of NO_2 in environmentally relevant systems as well as information that is critical for the development of new NO_2 detection and removal technologies. For this study, we have selected propylene carbonate (PC) as the representative organic liquid phase. PC is a polar, aprotic carbonate ester that is commonly used as a solvent in electrochemical systems[84,85,170] and in cosmetics.[171] The chemical structure of PC is depicted in Figure 14. Due to its prevalence in commercial products, PC is expected to have a significant environmental fate in the condensed phase and in the atmosphere.[171,172] Previous studies have shown that PC is mainly lost in the atmosphere through reaction with radical species such as OH and Cl.[171,173] In the condensed phase, PC has been used as a proxy for liquid-liquid phase separated aerosol where it was shown to facilitate significant partitioning of HNO_3 into the organic phase.[154] In the present work, PC also serves as an atmospheric-proxy compound. The ester functional group of PC is used as a probe to interrogate possible interaction with NO_2.

The main goal of this study is to further the understanding of the behavior of NO_2 at organic interfaces with oxygen-containing functional groups. To this end, the surface structure of PC, an environmentally relevant liquid, is characterized as a function of time before, during, and after exposure to NO_2. Infrared reflection-absorption spectroscopy (IRRAS) enables this characterization by probing vibrational changes that occur as a result of perturbations to the surface. From these studies, we determine the primary site of NO_2 interaction with PC and evaluate the recovery of the surface structure in the absence of NO_2.
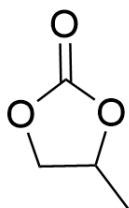
Figure 14. Chemical structure of propylene carbonate (PC).

4.2 Methods

4.2.1 Infrared Reflection-Absorption Spectroscopy

IRRAS has been previously employed by this lab to elucidate molecular changes at a variety of interfaces[40–42,44] and is employed here with modifications to allow for studies involving NO_2 gas at organic interfaces. Spectra were collected using a PerkinElmer Spectrum 3 FTIR spectrometer equipped with a custom-built mirror array within the sample compartment. In this setup, the unpolarized infrared light from the spectrometer is incident on the first of two gold mirrors (2 in. diameter), which is angled such that the incident light is directed onto the liquid surface at a 48° angle relative to the surface normal. The light that is specularly reflected off the liquid surface is collected with the second gold mirror, which directs the beam into the LN_2 cooled HgCdTe (MCT) detector. Surface-

57

sensitive infrared spectra were acquired by calculating reflectance-absorbance (*RA*) using Equation 45 as follows:

Equation 45

$$RA = -log_{10}\left(\frac{R}{R_0}\right)$$

In this equation, *R* is the reflectance of the sample surface (PC during or after exposure to NO_2) and R_0 is the reflectance of the reference surface (PC before exposure to NO_2). Through this process, the vibrational response of the liquid surface and bulk is effectively subtracted from the vibrational response of the sample after a perturbation to the surface. Both positive and negative peaks are observed in IRRAS spectra due to a convolution of the material's complex index of refraction and the nature of the subtraction of the reference. Generally, positive peaks occur when the reflectivity of the reference is greater than that of the sample, $R/R_0 < 1$. Negative peaks occur when the sample reflectance is greater than that of the reference, thus $R/R_0 > 1$. In the present study, spectra are complicated slightly due to the presence of the infrared-absorbing species NO_2 in the gas-phase. This results in vibrational bands of bulk gas-phase NO_2 that appear in the IRRAS spectra as positive peaks. IRRAS spectra in this study were taken in single-beam mode with a total 128 accumulations and 4 cm^{-1} resolution. All experiments were conducted in duplicate.

To study the interaction of NO_2 with the surface of PC using IRRAS, a Teflon cell was custom built and used for all studies. The Teflon cell consists of a baseplate that holds the liquid sample and an angled top cover that is fit with optical windows as well as the gas inlet and outlet. The baseplate holds a ~67 mm diameter glass petri dish in which the liquid sample is placed. The top cover is constructed such that the two optical windows (37.5 x 4

58

mm ZnSe, Pike Technologies) sit at a 45° angle. This allows for the spectra to be collected in the desired reflection geometry as well as minimizes reflection losses. The optical windows and the body of the Teflon cell are sealed using perfluoroelastomer (FFKM) o-rings. Gas flows enter and exit through separate Teflon Swagelok connections on the top of the cell. The Teflon cell and the IRRAS assembly are depicted in Figure 15.
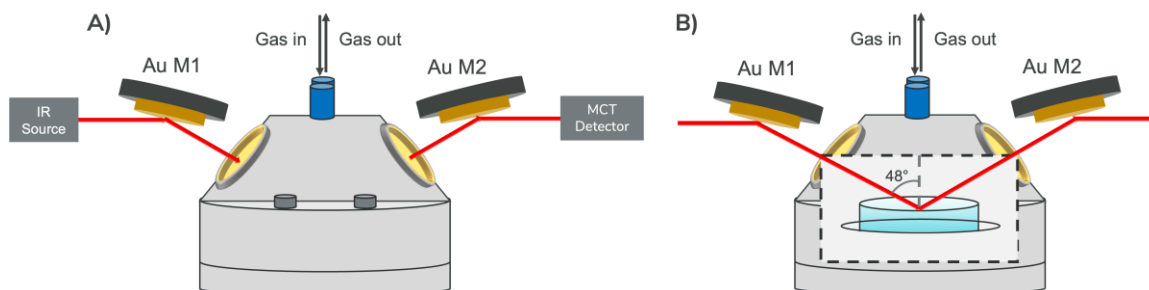
Figure 15. Schematic of the Teflon cell used for IRRAS experiments of NO_2 flowing over the PC surface. Panel A depicts the outside of the Teflon cell with the IR beam from the spectrometer being directed into the cell through the ZnSe windows. In panel B, the inside of the cell is shown and includes the IR beam reflecting off the PC interface within the petri dish.

4.2.2 Gas Flow Experiments

Propylene carbonate ($\geq$ 99.7%, anhydrous) was purchased from Sigma-Aldrich and was used as received. Due to the hygroscopic nature of PC, a single-use syringe was used to transfer all samples from the septum-sealed bottle. As a result, the water content can be reasonably assumed to be consistent with that reported by the manufacturer ($\leq$0.002 % by Karl Fischer titration).[113] At the beginning of each experiment, 20 mL of PC are placed in the petri dish within the Teflon cell. The cell is then sealed and purged with 50 mL/min N_2 (Linde, ultra-high purity 99.999%) and 5 mL/min air (Linde, Zero Grade) for at least 18 hours to remove CO_2 and limit water adsorbed to the walls of the cell. The flow rates of N_2 and air are regulated using mass flow controllers (MKS Instruments,1479A01511CS1BM), which flow the N_2 and air through KOH (Sigma-Aldrich, ACS Reagent Grade) traps to

remove excess water before flowing over the PC sample. The sample compartment of the FTIR is also sealed and purged with a separate flow of dry air (Parker Hannifin, 75-62 purge gas generator) to remove atmospheric CO_2 and limit water adsorbed to the outside of the ZnSe windows. Following the initial 18 hr purge, the N_2 flow rate within the cell is increased to 100 mL/min and allowed to equilibrate for 30 minutes before initial spectra are acquired. An initial spectrum of PC with 100 mL/min N_2 and 5 mL/min air flow is taken at the start of each trial and used as the reference (R_0) to calculate RA for all subsequent spectra taken in the trial. Following this initial spectrum, spectra are taken every 10 min for at least 30 min while still flowing 100 mL/min N_2 and 5 mL/min air. These spectra are used as controls for the PC surface before exposure to NO_2. After the initial spectra are acquired, NO_2 (Linde, 51 ppm in N_2) is set to a flow rate of 40 mL/min using a third mass flow controller (MKS Instruments, 1479A01511CS1BM). The NO_2 flows from the Mass-Flow controller through a nylon trap to remove any residual H_2O in the form of HNO_3 then joins the N_2 and air flows before entering the Teflon cell and flowing over the PC surface. The concentration of NO_2 that is delivered to the liquid surface is determined to be 5.1 ppm (see Appendix B for calculation and NO_2 gas absorption spectrum). Spectra are acquired every 10 min after turning on the NO_2 for a total elapsed time of 60 min at which point the NO_2 flow is turned off while leaving the N_2 and air flows unchanged. Spectra are then taken 5 minutes after the NO_2 flow is turned off and then in 10 min intervals for a total of 30 minutes as the NO_2 is purged from the gas cell. This set of spectra is referred to as "purge spectra" as they demonstrate changes occurring to the PC surface

as the NO$_2$ gas is purged from the system with N$_2$ and air. A schematic of the gas flow

system used in these experiments is depicted in Figure 16.
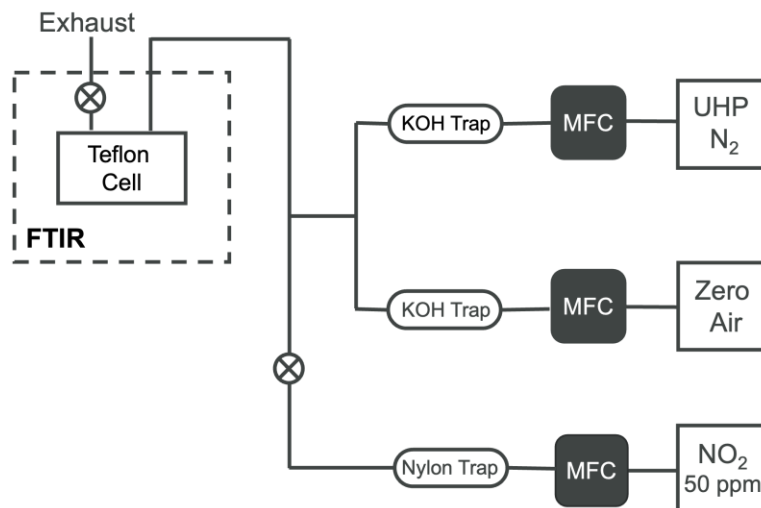
Figure 16. Schematic of gas lines used to purify and deliver gases to Teflon cell for spectroscopic measurements.

4.3 Results & Discussion

The interaction of NO$_2$ with organic interfaces is known to play a critical role in

the heterogeneous chemistry of the atmosphere as well as in the development of cutting-

edge NO$_2$ sensing and trapping technologies. The specific role that surface functional

groups play in these processes remains elusive. Here, we present an investigation into the

interaction of NO$_2$ at the interface of the organic liquid propylene carbonate (PC), a species

commonly used as representative atmospheric organic.[154,171,173] Surface-sensitive IRRAS

spectra were taken of the PC surface in three phases: before, during, and after exposure to

NO$_2$. All spectra were pre-processed by applying a Savitzky-Golay filter and fitting the

spectra to a common baseline. (Details of the spectral pre-processing can be found in

Appendix B.) In the initial phase, 100 mL/min N$_2$ and 5 mL/min air were flowed over the

PC surface and time-resolved spectra were acquired for up to 60 min before NO$_2$ was

introduced. The first spectrum acquired in this initial set of spectra was used as the reference (R_0) to calculate RA for all subsequent spectra. The IRRAS spectrum of PC after 30 min elapsed in the initial phase is plotted as spectrum A in Figure 17. No notable peaks are present in this spectrum, indicating that the flow of N_2 and air does not change the vibrational modes of PC at the surface. (See Figure 40 in Appendix B for plot of all reference spectra.)

In the second phase of the experiment, 40 mL/min of 50 ppm NO_2 was allowed to mix with the initial flow to deliver 5.1 ppm NO_2 to the PC surface. The spectrum of the PC surface with NO_2 flowing for 60 min is plotted as spectrum B in Figure 17. Comparison of spectrum A and spectrum B demonstrates that the flow of NO_2 over the PC surface causes significant changes to the interfacial vibrational modes of PC. The vibrational mode of PC that is most strongly affected by the presence of NO_2 is the carbonyl (C=O) stretch, as observed in the appearance of the intense negative band at ~1860 cm^{-1} in spectrum B. Other peaks of PC are also affected, but to a lesser extent. These peaks occur in the low frequency region of the spectrum (1100 – 1400 cm^{-1}) and are assigned to combinations of vibrations within the ring structure of PC, including O-C, C-H, and C-C modes.[85,139] Assignment of the low-frequency peaks observed in the IRRAS spectrum during NO_2 flow can be found in Appendix B. The small changes observed in the low frequency modes are expected to be a result of the strong correlation of the modes within the ring structure. Bands originating from gas-phase NO_2 can also be observed in spectrum B at 1600 and 1628 cm^{-1}.[174]

The extent of perturbation to the carbonyl stretching mode when the surface of PC is exposed to NO_2 points to a selective interaction of NO_2 with this moiety. We have

considered the possibility of this change resulting from a permanent reaction as well as from favorable non-covalent interactions between the two partially charged species. In an investigation of oleic acid monolayers exposed to 1000 ppm NO_2, there was no evidence of bond cleavage or addition across the double bond. The major effect of NO_2 on the monolayers was found to be an isomerization of the double bond.[175] It is therefore unlikely for NO_2 to cause a significant reaction with PC in the present study considering PC has similar functional groups and was exposed to a much lower NO_2 concentration. Additionally, NO_2 has been shown to have slight hydrophobic character at aqueous interfaces and tends to orient with the oxygen atoms pointed towards the air and the nitrogen toward the surface.[22,176] Considering this orientation, we are confident that the spectral changes observed here are a result of non-covalent interactions, namely Van der Waals and dipole-dipole interactions, between NO_2 and the carbonyl of PC.

To determine if this perturbation to the carbonyl persists in the absence of NO_2 flow, purge spectra were acquired. After flowing NO_2 over the PC surface for 60 min, the flow was turned off and it was purged from the sample cell with the initial flow rates of N_2 and air. The spectra of the PC surface after 5 and 30 min of purging are presented in Figure 17 as spectrum C and D, respectively. After 30 min of purging, the surface of PC completely returns to its structure before exposure to NO_2, providing evidence that the perturbations to the PC surface are reversible and the surface is not permanently altered. We then assert that the carbonyl of PC facilitates the reversible binding of NO_2 at the interface.
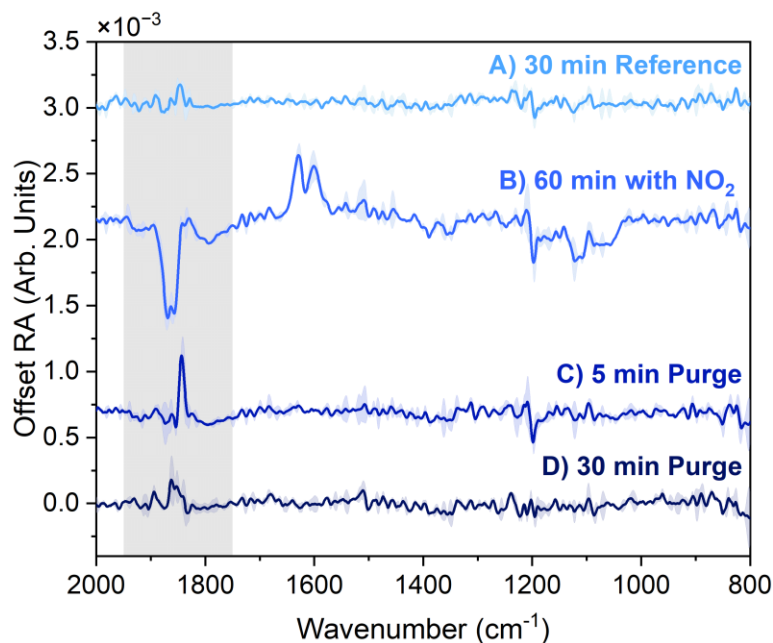
Figure 17. IRRAS spectra of the surface of PC before, during, and after exposure to 5.1 ppm NO_2. A) 30 min. reference B) 60 min with NO_2 C) 5 min of purging NO_2 with N_2 and air. D) 30 min of purging NO_2 with N_2 and air. Spectra plotted are an average of two trials and the standard deviation is plotted as shading. Spectra are offset for clarity and the carbonyl region (1950-1750 cm^{-1}) is highlighted with grey shading.

We also observe that the spectral changes induced by NO_2 at the PC surface are established within the first 5 min of exposure and are constant with time. Time-resolved spectra of the PC surface during the 60 min NO_2 exposure are presented in Figure 18a. The carbonyl band is present at the earliest time point (5 min) and does not change appreciably, in intensity or peak shape, for the duration of the exposure. The NO_2 band intensity reaches an equilibrium after 10 minutes. Combined, these observations indicate that NO_2 saturates the PC surface within 10 min and the surface structure remains constant as NO_2 continues to flow. No peaks were observed that increased in intensity over time, providing additional evidence against the formation and subsequent build-up of a reaction product over time.

To further elucidate the surface structure of PC caused by NO_2 exposure, IRRAS spectra of PC at 60 min NO_2 flow are compared to bulk ATR-FTIR spectra of PC in Figure

18b. Details of the ATR-FTIR experiment can be found in Appendix B. In the low frequency "fingerprint" region ($<$1500 cm^{-1}), the IRRAS and ATR peaks are well overlapped, supporting our previous assignment. The largest discrepancy between the bulk and interfacial spectra is in the carbonyl stretching band. In the ATR spectrum, the carbonyl band is centered at 1780 cm^{-1}, which is in agreement with previous reports of bulk FTIR spectra of PC.[85,139] In the IRRAS spectra, this peak is significantly blue-shifted and occurs at ~1860 cm^{-1}. This shift is due to several factors including convolution of the real and imaginary components of the complex index of refraction. This phenomenon occurs in reflection spectra when a material has a very strong absorption band, which causes a change in the intensity of the light as well as a change in the reflectivity of the interface. The results are differences in peak position and intensity compared to linear bulk methods.[38] The dehydration of carbonyl groups in lipid films has also been shown to induce blue-shifts in the carbonyl band.[39,177,178] For example, the dehydrated carbonyl band of 1,2-dipalmitoyl-sn-glycero-3-phosphatidic acid films on water appears 18 cm^{-1} higher than the hydrated carbonyl band.[39] It is therefore highly plausible that the blue-shift observed here is at least partially due to the disruption and subsequent rearrangement of the PC liquid structure induced by association of NO_2 with the carbonyl.
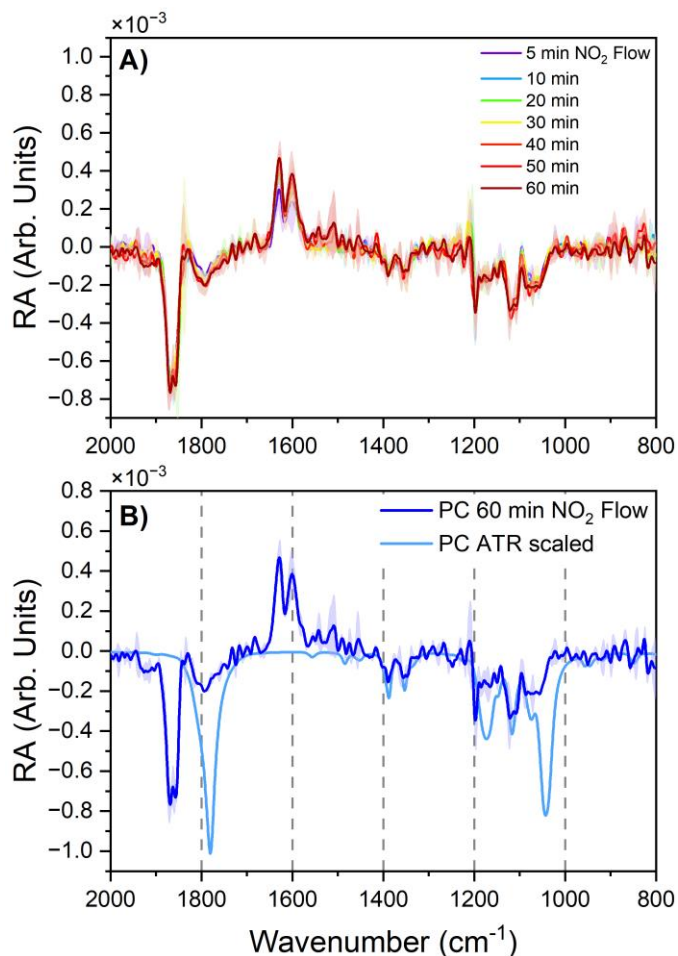
Figure 18. Time-resolved IRRAS spectra of the PC surface during flow of 5.1 ppm NO_2 (panel A). Comparison of IRRAS spectrum of PC surface exposed to NO_2 for 60 min and the bulk ATR-FTIR spectrum of pure PC (panel B). All spectra are an average of two trials and the standard deviation is plotted as shading. ATR spectrum is scaled by 10^{-3} in order to plot on same scale as IRRAS spectrum. Dashed vertical reference lines are included every 200 cm^{-1} in panel B to aid in the comparison.

Exposure of the PC surface to NO_2 also causes the carbonyl band in the IRRAS spectra to take on a different peak shape in comparison to the bulk solution spectrum. In the ATR spectra that reports on the solution phase, the observed carbonyl band consists of a single, sharp peak centered at 1780 cm^{-1}. A weaker band assigned to a combination of symmetric ring stretching and carbonate stretching modes causes a broadening of this peak on the high frequency side.[139] In contrast, the carbonyl band observed in the IRRAS spectra

66

during NO$_2$ flow has a doublet peak structure, with peaks of nearly equal intensity centered at 1869 and 1857 cm^{-1}. Similar splitting of carbonyl bands in FTIR spectra has been observed for systems in which the carbonyl experiences a distribution of interactions (e.g. hydrogen bonding and ion solvation) causing changes to the vibrational environment.[177–179] Propylene carbonate exhibits a 15 – 40 cm^{-1} splitting of the carbonyl band as a result of solvating various ions.[179] Brooksby and Fawcett show that the carbonyl band of pure PC is a single peak at 1795 cm^{-1} in the ATR-FTIR spectrum. Association of Li$^+$ ions with the carbonyl in solution results in the splitting of the band into two peaks centered at 1770 and 1792 cm^{-1}.[180] We expect that the carbonyl doublet peak structure observed in these experiments is due to NO$_2$ binding to the carbonyl in different symmetries. It is also possible that this splitting is due to two populations of carbonyl groups: one that is directly associated with NO$_2$ and another that is not but has a disrupted solvation structure due to the presence of NO$_2$.

This carbonyl peak structure was also observed when NO$_2$ was flowed over a different organic, diethyl sebacate (DES), during control studies. DES was selected for comparison as it contains similar functional groups to PC (diester) but is a linear molecule. Additionally, DES has been used as a model ester-containing molecule for previous studies of atmospheric heterogeneous reactions.[29,181] Structural changes of the DES surface induced by NO$_2$ were observed in two of the four total trials. Despite the lack of reproducibility, the average of the first two trials are presented here to provide support to the PC experiments which were reproducible in all cases. The IRRAS spectrum of the DES surface during 40 min flow of NO$_2$ is presented in Figure 19 as spectrum A. The IRRAS

spectrum of the PC surface during exposure to NO_2 is included in Figure 19 as spectrum B

for comparison. When the DES is exposed to NO_2, the carbonyl stretch is the only mode

that is affected as indicated by the appearance of the intense positive band at ~1740 cm^{-1}.

This band also exhibits the same doublet peak structure as PC when exposed to NO_2. These

results provide additional support for carbonyl-specific interactions of NO_2 at organic ester

interfaces. See Figure 42 in Appendix B for the additional two trials that did not exhibit

changes to the carbonyl in the presence of NO_2.
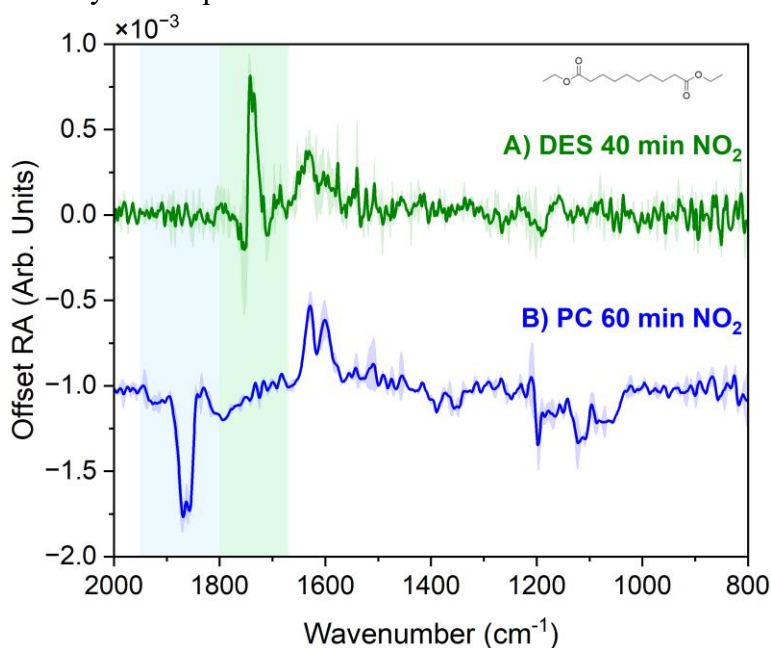
Figure 19. IRRAS spectrum of the DES surface during 40 min flow of 5.1 ppm NO_2 (green, A). IRRAS spectrum of the PC surface during 60 min flow of 5.1 ppm NO_2 is included for comparison (B, blue). Spectra plotted are an average of two trials and the standard deviation is plotted as shading. Spectra are offset for clarity and the carbonyl region of DES and PC are highlighted with green and blue shading, respectively.

The flow of NO_2 has been shown in previous works to repel water from the surface

of 1,4 dioxane/water solutions due to the mildly hydrophobic nature of the gas.[176] Here, we

have taken careful measures to limit water contamination in the pure PC solutions and

confirmed using Raman spectra that the OH stretch was below the limit of detection (Figure

43 in Appendix B). However, PC has also been shown to facilitate microscopic aggregation of water within the solvent,[62,182] therefore there is a slight possibility of very small amounts of water contamination. We then consider the possibility that the spectral changes observed when the PC surface is exposed to NO_2 are a result of dehydration. To test this possibility, the spectral changes resulting from flowing 100 mL/min N_2 and 5 mL/min air over a 0.091 mole fraction (χ_{water}) water in PC solution were investigated. Spectra were acquired in 10 min increments for 120 min. *RA* was calculated for every time point using the initial spectrum as R_0 and the result is plotted in Figure 20a. As a result, these spectra demonstrate changes to PC vibrational modes as water is removed from the surface due to the N_2 and air flow. All PC modes undergo significant changes that increase in intensity over time. Comparison of the changes in the carbonyl band caused by exposure to NO_2 and by dehydration (Figure 20b), shows that NO_2 causes a significantly different peak shape that is blue-shifted from the peak caused by dehydration. Thus, it is clear the changes to the PC interfacial structure when NO_2 is present are not simply caused by dehydration. Exposure of the PC/water interface to NO_2 was also studied and any changes that may have been caused by NO_2 were obscured by the large changes caused by dehydration (Figure 44 in Appendix B). The results support our conclusions that the spectral changes induced by the presence of NO_2 over the PC surface are a result of NO_2 forming strong interactions with the carbonyl of PC.
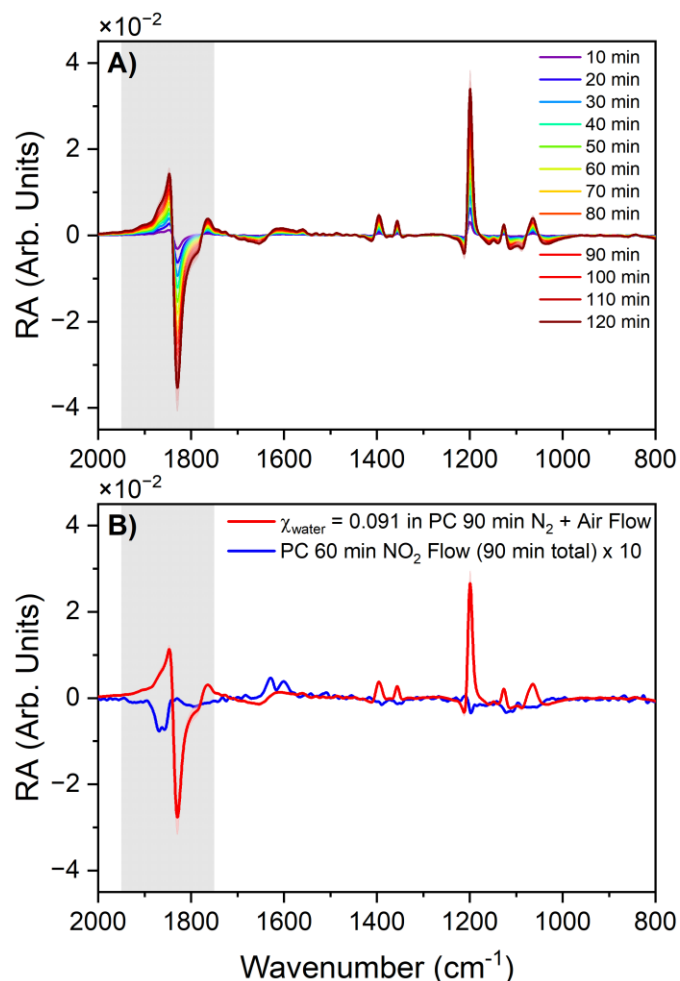
Figure 20. Time-resolved IRRAS spectra of a 0.091 mole fraction water/PC solution as N_2 and air flows over the surface (panel A). Comparison of the PC spectral changes resulting from 90 min of dehydration of the water/PC solution interface (panel B, red) with those caused by 60 min NO_2 flow at the pure PC surface (panel B, blue). All spectra are an average of two trials and the standard deviation is plotted as shading. The 60 min NO_2 flow spectrum (panel B, blue) is scaled by 10 for comparison. The carbonyl region (1950-1750 cm^{-1}) is highlighted with grey shading.

5.4 Conclusions

In this work, we characterize the structural changes that occur as 5.1 ppm NO_2 is flowed over the surface of propylene carbonate using surface-sensitive infrared reflection-absorption spectroscopy. IRRAS spectra reveal large changes to the interfacial vibrational modes of PC upon introduction of NO_2. The carbonyl stretching mode of PC is most affected by this perturbation, resulting in an intense negative band with a doublet peak

70

structure. Interfacial changes induced by PC were shown to be constant over time and NO_2 was shown to saturate the PC surface within 10 min. The surface of PC recovers fully within 30 min of stopping the NO_2 flow. These observations lead to the conclusion that the carbonyl of PC facilitates reversible non-covalent interactions with NO_2 at the gas/liquid interface. Binding of NO_2 at the surface induces a disruption of the PC liquid structure at the interface and establishes a distribution of binding symmetries. Here, diethyl sebacate, was also studied and showed the same reversible carbonyl-specific interactions with NO_2 at the air/liquid interface.

Chapter 5. Progress Toward N_2O_5 Synthesis and Reaction at Organic Interfaces

5.1 Introduction

The nocturnal chemistry of the lower atmosphere is dominated by reactions involving the nitrogen oxide species, NO_3 and N_2O_5.[1] The lack of photolysis at night enables NO_3, formed by the reaction of NO_2 with O_3, to persist long enough to form N_2O_5 through subsequent reaction with NO_2. Of particular interest are heterogeneous reactions of N_2O_5 at aerosol surfaces, as they have been shown to provide a major sink for NO_x species and impact ozone production.[2]

Many studies have been conducted with the goal of understanding the extent to which N_2O_5 is taken up by various interfaces relevant to aerosol.[28,30,31,34,183–186] Measurements of the reactive uptake of N_2O_5 at vapor/liquid interfaces reveals that the presence of organics at the liquid surface greatly impacts the uptake coefficient.[30,33,185] Bertram et al. demonstrates that the presence of insoluble organic monolayers spread on water decreases the N_2O_5 uptake coefficient by factors ranging from 17 to 61 in comparison to the bare water interface.[30] Additionally, the morphology and composition of the film have been shown to greatly alter the uptake coefficient.[30,31] Computational studies have led to breakthrough discoveries on the mechanism of N_2O_5 uptake and hydrolysis at vapor/liquid interfaces. Galib and Limmer report that the hydrolysis of N_2O_5 occurs within the topmost 20 Å of the liquid surface and requires an initial internal charge separation of

the NO_2^+ and NO_3^- species to be stabilized in order to proceed.[28] As a result, the local dielectric environment can strongly influence the energetic favorability of this process. It is then the aim of this work to understand how differing dielectric environments at the vapor/organic liquid interface drives the charge separation stabilization of N_2O_5.

In this work, the dielectric of the liquid surface will be tuned by choosing organic liquids with similar functional groups, but vastly different dielectric constants (ε). Propylene carbonate (PC, $\varepsilon = 66$) and diethyl sebacate (DES, $\varepsilon = 5$) are selected as the organic liquid phases. The reactive uptake of N_2O_5 at the surface of PC and DES has been measured in previous studies using chemical ionization mass spectrometry (CIMS). The uptake coefficients reported for PC[187] and DES[29] are $\sim 10^{-2}$ and 0.51×10^{-4}, respectively. The majority of N_2O_5 uptake measurements are conducted using CIMS, as it is highly selective and sensitive to N_2O_5. These studies measure the extent to which N_2O_5 is taken up at the interface but do not inform on the specific interactions between the gas and liquid species. Here, we employ the surface-sensitive spectroscopic technique, infrared reflection-absorption spectroscopy (IRRAS) to reveal molecular-level gas-liquid interactions at the interface. The vibrational modes of intact N_2O_5 vs. the charge separated NO_2^+ and NO_3^- species will reveal the ability of each interface to stabilize charge separation. Greater intensities of the charge separated species compared to intact N_2O_5 is an indication of greater charge separation stabilization. N_2O_5 gas will be synthesized through the reaction of O_3 with NO_2, which follows the scheme:

$$(1)\ O_2 + h\nu \rightarrow 2\ O$$

$$(2)\ O_2 + O + M \rightarrow O_3 + M$$

73

$$(3) \ NO_2 + O_3 \rightarrow NO_3 + O_2$$

$$(4) \ NO_3 + NO_2 \rightarrow N_2O_5$$
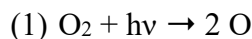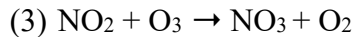
In the following sections, the design and construction of the N_2O_5 synthesis system is described. Initial experiments are conducted with the goal of characterizing the gas flow produced and identifying and potential issues with the experimental design. These studies reveal that KBr is not a suitable choice for optical windows and that there is significant H_2O contamination, leading to greater HNO_3 impurities than expected. Potential solutions are discussed. Studies of the N_2O_5 gas flow over the PC and DES surface reveal carbonyl-specific interactions with the gas molecules at the interface. These results should inform future computational and experimental studies.

5.2 Methods

5.2.1 N₂O₅ Synthesis System Design

The design of the N_2O_5 gas synthesis system in this lab is based on the design reported by Kregel et al.[188] Notable changes to the design are made to improve efficiency, including using mass-flow controllers to set the flow rate of all reagent gases used. The gas-synthesis system constructed in this lab consists of compressed cylinders of zero grade air (Linde), nitrogen (Linde, ultra-high purity 99.999%), and NO_2 (Linde, 51 ppm in N_2) that are fitted with proper regulators and used as gas supply to a glass reaction chamber. Mass-flow controllers (MKS Instruments, 1479A01511CS1BM) are connected immediately following the cylinders to set the flow rates of each of the three reagent gases. N_2, NO_2, and zero air flow rates are 100, 40, and 5 sccm (mL/min), respectively during synthesis of N_2O_5.

Following the mass-flow controllers, each reagent gas is purified. Excess water in the form of HNO_3 is removed from the NO_2 supply by flowing through a glass bubbler fitted with 100% nylon mesh. N_2 and zero air are dried by flowing through separate glass bubbler traps filled with KOH pellets (Sigma-Aldrich, ACS Reagent Grade). Once dried, zero air and N_2 flows join and then flow through an ozone generator (Jelight, model 610), which uses a Hg pen lamp to photolyze the low concentration of O_2 to form O_3. The concentration of O_3 is measured using an OceanOptics UV spectrometer. Details of this procedure can be found in Appendix C. The flow of N_2, O_2, and O_3 is then joined with the purified NO_2 flow. Gases flow immediately into a 12 in. x 2 in. glass reaction chamber (V = 529 cm^3) to form N_2O_5. Residence/mixing time in the reaction chamber is approximately 5.3 min. Initial concentrations of the reagent gases give an estimated N_2O_5 concentration of 2.4 ppm. The N_2O_5 gas then flows either to exhaust or through to the detection cell. All tubing used in this gas synthesis system is 0.25 in. OD x 0.125 in. ID Teflon tubing connected using PFA Swagelok fittings and valves. A list of all materials used to build this system can be found in Appendix C. A schematic of the N_2O_5 synthesis system is presented in Figure 21 and a photograph of the system with each component labeled is presented in Figure 22.
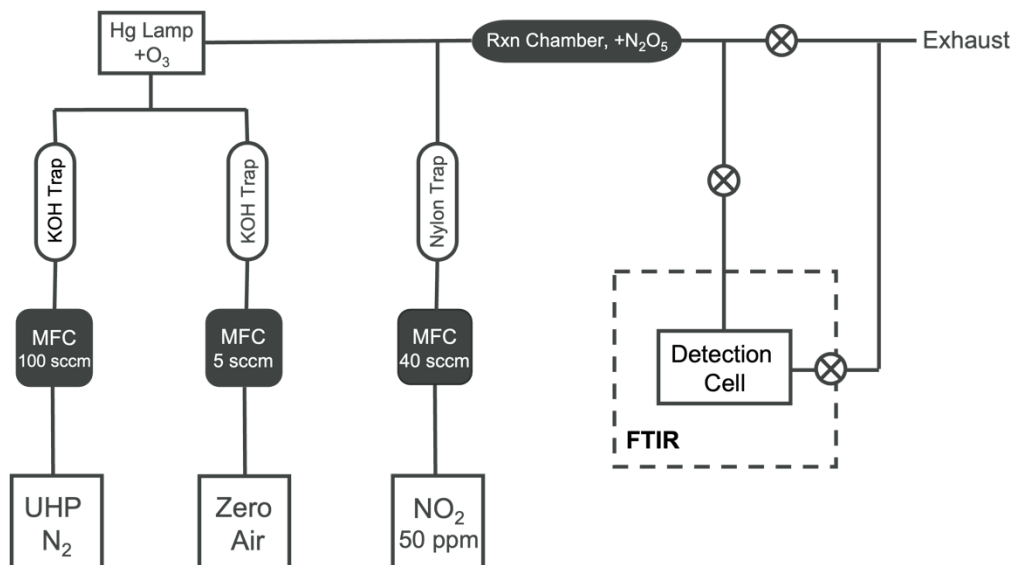
Figure 21. Schematic of the gas system built to synthesize N_2O_5 and deliver it to organic interfaces for spectroscopic analysis.
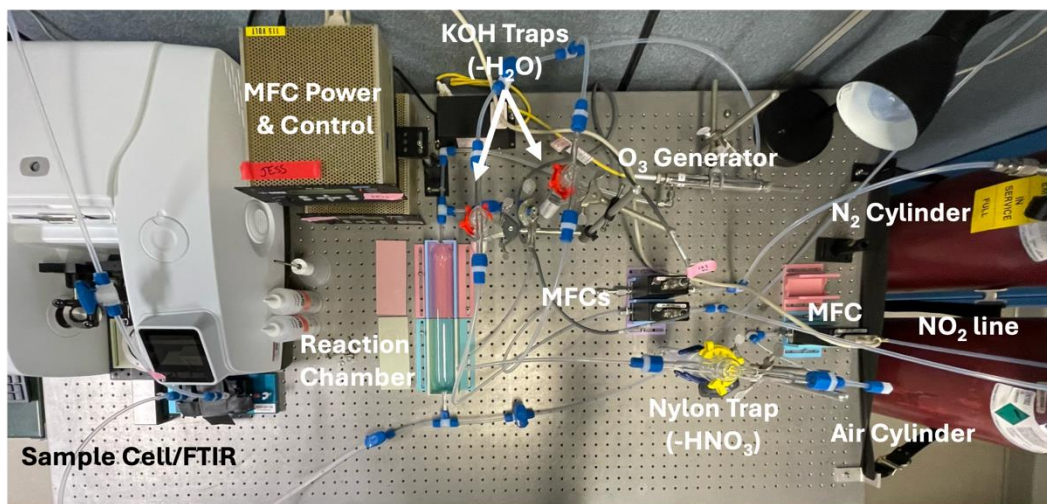
Figure 22. Picture of N_2O_5 synthesis system as built in the Allen lab. All major components of the system are labeled. The NO_2 cylinder is not visible here as it is stored inside of a gas cabinet to the right of the nitrogen and zero air cylinders. The NO_2 line that connects the cylinder to the mass-flow controller is visible.

The detection method employed here also differs from that of Kregel et al. who uses mass spectrometry to select the reaction products of N_2O_5 flowing over aqueous surfaces. Here, IRRAS is used to detect N_2O_5 and its reaction products at the interface of organic liquids. To enable these studies, the gas synthesis system is coupled with a Teflon

optical cell. This cell is described in Chapter 4 and a schematic is included in Figure 15. Briefly, the Teflon cell consists of a baseplate that holds the liquid sample and an angled top cover that is fit with optical windows as well as the gas inlet and outlet. The top cover is constructed such that the two optical windows (37.5 x 4 mm ZnSe, Pike Technologies) sit at a 45° angle. This allows for the spectra to be collected in the desired reflection geometry as well as minimizes reflection losses. The optical windows and the body of the Teflon cell are sealed using perfluoroelastomer (FFKM) o-rings. Gas flows enter and exit through separate Teflon Swagelok connections on the top of the cell.

5.2.2 N_2O_5 Flow Experiments

Before conducting any experiments using this system, all lines must be purged by flowing the reagent gases through the system to exhaust for at least 1 week. Positive pressure or continuous flow must be maintained throughout the entire course of data acquisition in order to limit water contamination. The flow rates of N_2, air, and NO_2 are 50, 5, and 2 mL/min, respectively when N_2O_5 is not being produced. Prior to setting up an experiment, the valve that separates the NO_2 line from the rest of the system is closed while NO_2 is still flowing at its purge rate. The valve on the NO_2 regulator is then closed and the remaining pressure of NO_2 gas is allowed to fill the closed off portion of the gas line until the NO_2 flow rate on the controller reads 0 mL/min. The mass-flow controller for NO_2 is then closed. This process is carried out to establish positive pressure in the NO_2 line while the rest of the gas system is purged through the Teflon cell after the organic sample is placed. Care is taken not to over pressurize the line and break the seal on the nylon trap. At

least 30 minutes are allowed for the N_2 and air flows to purge any remaining NO_2 from the sample cell before it is opened.

Experiments are then conducted by first placing a 20 mL sample of the chosen organic (either DES or PC) in the petri dish within the Teflon cell. The cell is then sealed and N_2 and air are flowed over the surface at 50 and 5 mL/min, respectively for ~18 hr. to remove CO_2 and water vapor. Following the initial 18 hr. purge, the N_2 flow rate is increased to 100 mL/min and allowed to equilibrate for 30 min. before initial spectra are acquired. An initial spectrum of the organic surface with 100 mL/min N_2 and 5 mL/min air flow is taken at the start of each trial and used as the reference (R_0) to calculate RA for all subsequent spectra taken in the trial. Following this initial spectrum, spectra are taken every 10 min for at least 30 min while still flowing 100 mL/min N_2 and 5 mL/min air. These spectra are used as controls for the organic surface before exposure to N_2O_5. After the initial spectra are acquired, the NO_2 flow rate is set to 40 mL/min and the Hg lamp is turned on to begin production of O_3 and subsequently, N_2O_5. Spectra of the organic surface during exposure to N_2O_5 are taken at 10 min. intervals for at least 90 min. Following N_2O_5 exposure, the NO_2 flow is stopped, and the Hg lamp is turned off while leaving the N_2 and air flows unchanged. The N_2O_5 gas is purged from the system and spectra are taken at 10 min. intervals for at least 30 min.

5.3 Results

The charge separation stabilization capability of unique organic interfaces is of significant fundamental and applied interest. Here, we present the preliminary investigations into ability of two representative organic phases, propylene carbonate (PC)

and diethyl sebacate (DES), to stabilize the charge separation of the gas-phase probe molecule, N_2O_5. In the first stage of experiments, KBr windows were used in the Teflon IRRAS cell instead of ZnSe. N_2O_5 flow experiments were conducted for both PC and DES using this setup. Figure 23 depicts the time-resolved IRRAS spectra of the PC (Figure 23a) and DES (Figure 23c) surfaces during N_2O_5 exposure. The time-resolved spectra of both PC and DES reveal that the presence of N_2O_5 causes a band between 1300 and 1500 cm^{-1} to grow in as a function of time. One possibility for the origin of these peaks is that the flow of the gas changes the surface structure of the organic surface over time, causing intensity changes of their vibrational bands. To explore this possibility, the ATR-FTIR spectra of bulk PC (Figure 23b) and DES (Figure 23d) before gas exposure are compared to the IRRAS spectra after flowing N_2O_5 over the surface for 90 min. For PC, the ATR and IRRAS peaks in this region are well-overlapped, therefore it is reasonable to conclude that the changes observed in the IRRAS spectra result from changes to PC's vibrational modes. In contrast, the ATR and IRRAS peaks for DES are not well-overlapped. DES has some structure in the 1300 and 1500 cm^{-1} region; however, no peaks distinctly correspond to those observed in the IRRAS spectrum. Additionally, the peak positions and shape of the bands that grow in as a function of N_2O_5 exposure are very similar for both PC and DES despite their differing bulk structure. This observation points to the peaks having the same origin. As a result, the comparison of the ATR and IRRAS spectra for PC and DES does not conclusively demonstrate that the changes observed in the IRRAS spectra originate from unique changes to the liquid surface.
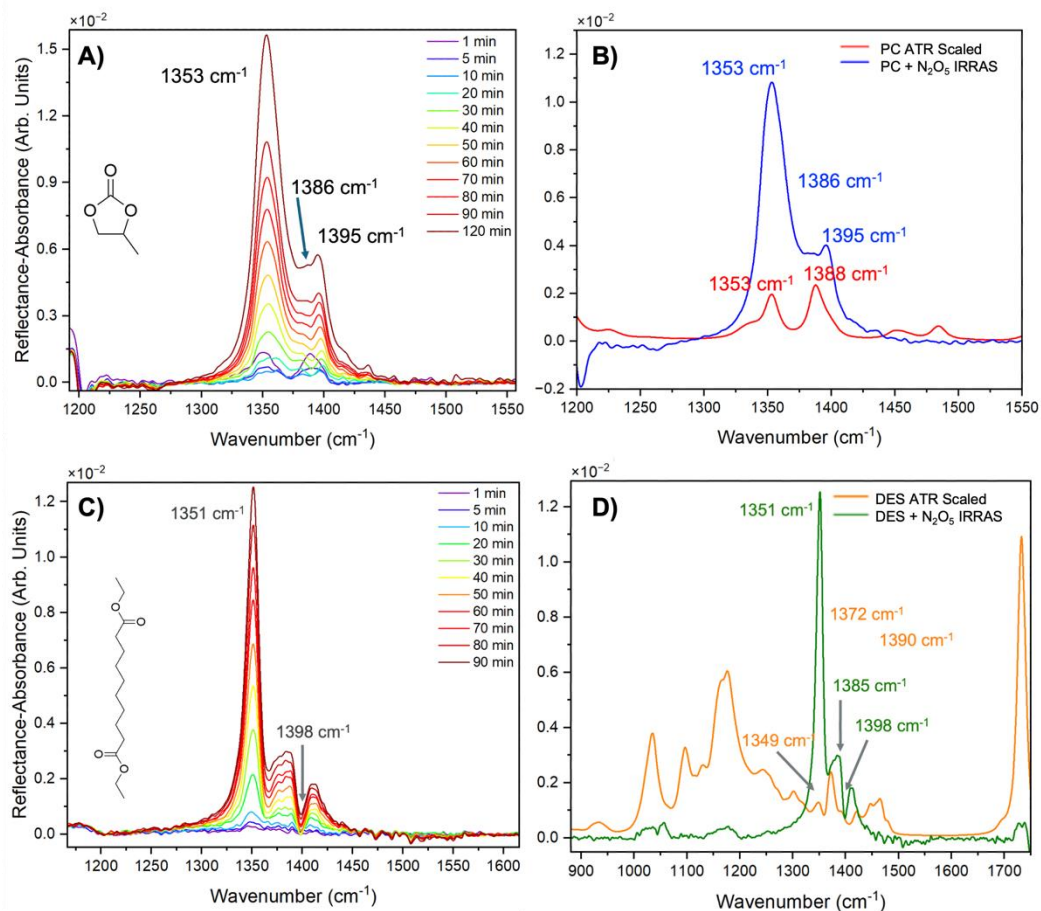
Figure 23. Time-resolved IRRAS spectra of N_2O_5 flowing over the PC (A) and DES (C) surfaces for initial experiments in which KBr windows were used. IRRAS spectra after 90 min N_2O_5 flow are compared to the ATR-FTIR spectra of bulk PC (B) and bulk DES (D).

We then explore the possibility that these peaks are due to a build-up of adsorbed species. This is achieved by replacing the liquid sample in the Teflon cell with a gold mirror having the same surface height of the liquid samples. The N_2O_5 flow experiments are repeated, and the resulting spectra sample gas-phase species as well as any adsorbed species. The time-resolved spectra of the gold mirror during N_2O_5 flow experiments are presented in Figure 24. The lack of the liquid interface allows for the peaks belonging to the reactant species to be observed. These bands occur in the spectra between 900 and 1300 cm^{-1}. Control experiments wherein the individual reagent gases are flowed over the gold

mirror aid in the assignment of peaks belonging to the reagent gas flows as demonstrated by the boxes in Figure 24. These peaks do not change as a function of time, which is expected for species that flow continuously through the system and do not build up over time. In contrast, a band grows in between 1300 and 1500 cm^{-1} as a function of N_2O_5 flowing over the gold mirror with time. This band is at the same position and has a similar doublet structure as the bands observed when N_2O_5 is flowed over both PC and DES. It is then concluded that this species is either adsorbed to the reflecting surface (gold mirror or organic liquid) or the optical windows.
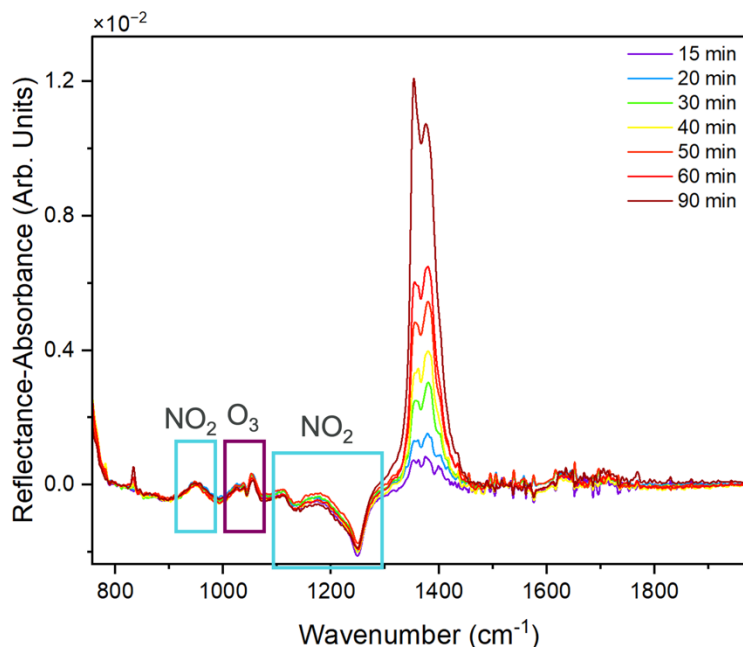
Figure 24. Time-resolved IRRAS spectra of N_2O_5 flow over a gold mirror within the Teflon cell. Peaks in the spectra that do not change as a function of time are identified from control experiments of the individual gas flows as belonging to O_3 and the flow of NO_2.

To conclusively determine if the adsorbed species is present on the KBr windows, spectra of the PC surface were taken with and without the KBr windows in place. Subtraction of these spectra leave only the peaks belonging to the windows as the liquid response is removed. The subtracted spectrum is presented in Figure 25 along with the

IRRAS spectrum of N_2O_5 flowing over PC for 90 min. From the spectrum of the KBr windows after the N_2O_5 flow experiments, it is clear that the species responsible for the band occurring between 1300 and 1500 cm^{-1} in the IRRAS spectra of PC, DES, and the gold mirror is from a species adsorbed to the KBr windows. This species builds up over time and does not decrease with purging. Previous studies by Finlayson-Pitts and coworkers have shown that $BrNO_2$ is formed when N_2O_5 is flowed over solid NaBr.[189] FTIR peaks of this product are observed at 787, 1292, and 1660 cm^{-1}. It is therefore highly likely that $BrNO_2$ is formed by the reaction of N_2O_5 with the KBr window surface, resulting in the spectral changes observed here. KBr is also known to be highly hygroscopic. Despite our best efforts to dry the gas line, it is nearly impossible to remove all water adsorbed to the windows at atmospheric temperature and pressure. The hydrolysis of N_2O_5 produces HNO_3, therefore any residual water on the window surface could form this product. The IR peaks of HNO_3 occur in the $1300 - 1400$ cm^{-1} region of the spectrum.[190] The most likely cause of the band observed in our IRRAS spectra is HNO_3 that forms on the KBr window surface and gets trapped there. As a result, the KBr windows are replaced with ZnSe windows for all subsequent experiments.
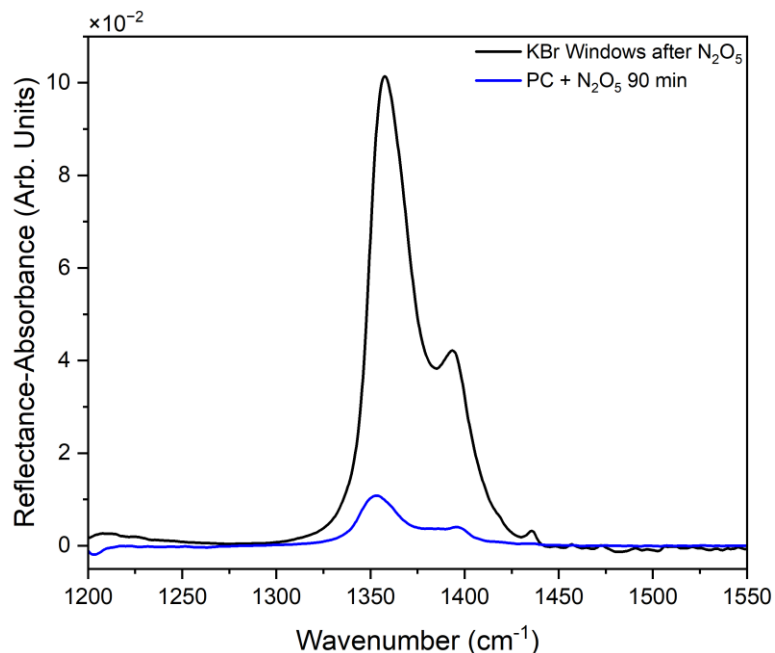
Figure 25. Difference spectrum showing peaks from KBr windows after N_2O_5 flow experiments (black) compared to the IRRAS spectrum of the PC surface during 90 min. exposure to N_2O_5 (blue).

After replacing the KBr windows with ZnSe, the IRRAS spectrum of N_2O_5 flowing over the gold mirror surface was taken again to ensure that the same band did not appear. This spectrum is depicted in Figure 26, where the same experiment conducted with KBr windows is included for comparison. The low-frequency region of the spectrum (< 1300 cm^{-1}) is unchanged upon switching to ZnSe windows. As predicted, the band between 1300 and 1500 cm^{-1} is not present in the N_2O_5 gold mirror spectrum acquired with ZnSe windows. The choice of ZnSe as the optimal window material for N_2O_5 flow experiments is therefore confirmed.
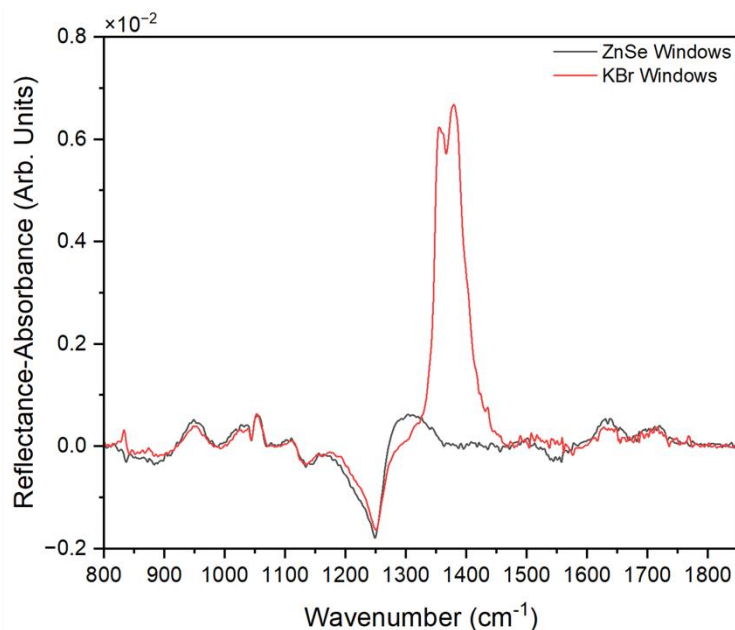
Figure 26. IRRAS spectra of N_2O_5 flowing over a gold mirror collected using ZnSe windows (black) compared to that collected using KBr windows (red). The spectra indicate that ZnSe is a suitable window material as the adsorbed species formed at the KBr surface is not observed for ZnSe.

After the suitable choice of optical window material was determined, the IRRAS spectra of NO_2 and N_2O_5 flowing over the gold mirror surface were carried out to fully assign the peaks observed. These spectra are presented in Figure 27 along with the spectrum acquired 20 minutes after the production of N_2O_5 was stopped and the cell was purged with 100 mL/min N_2 and 5 mL/min air. The spectrum of the NO_2 flow (red trace in Figure 27) contains negative peaks at 900, 1150, and 1250 cm^{-1} and positive peaks at 975, 1600, and 1630 cm^{-1}. The positive peaks at 1600 and 1630 cm^{-1} are assigned to the asymmetric stretch of gas-phase NO_2 based on literature observations.[174] The remaining peaks are not observed in previous FTIR studies of gas-phase NO_2, therefore we expect that they result from adsorbed species, possibly on the gold mirror surface. Additionally, when NO_2 is consumed to form N_2O_5, only the bands at 1600 and 1630 cm^{-1} decrease in intensity as can be observed by comparing the red and black traces in Figure 27. This

provides further evidence that the peaks occurring at 900, 975, 1150, and 1250 cm^{-1} in the NO$_2$ flow spectrum are not from free gas-phase NO$_2$. The spectrum of N$_2$O$_5$ flowing over the gold mirror (black trace in Figure 27) contains the same peaks observed in the NO$_2$ spectrum along with four additional peaks: a positive band from 1000-1100 cm^{-1} assigned to O$_3$ gas, a broad positive band centered at 1326 cm^{-1}, a weak negative band at 1550 cm^{-1}, and a positive band at 1710 cm^{-1}. In previous FTIR measurements of N$_2$O$_5$ gas, peaks observed at 743, 1246, and 1720 cm^{-1} were assigned to vibrations of N$_2$O$_5$ and a peak observed at 1326 cm^{-1} was assigned to HNO$_3$ impurities.[174] Comparing these assignments to our IRRAS spectra of N$_2$O$_5$ indicates that a significant fraction of the gas flow is HNO$_3$ and a small amount of N$_2$O$_5$ may still remain intact, producing the peak observed at 1710 cm^{-1}. Upon purging N$_2$O$_5$ from the cell (blue trace in Figure 27), all peaks are removed from the spectrum with the exception of the band at 1326 cm^{-1}. This observation provides further support to the assignment of this band to HNO$_3$.
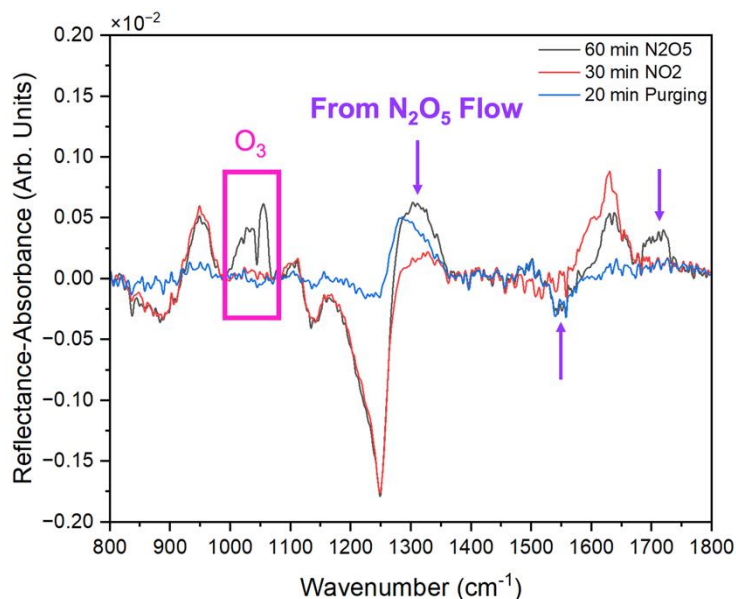
Figure 27. IRRAS spectra of NO_2 (red) and N_2O_5 (black) flowing over a gold mirror within the Teflon cell equipped with ZnSe windows. The spectrum recorded after purging N_2O_5 from the cell for 20 min (blue) is also included for comparison.

To remove convolution possibly caused by NO_2 adsorption on the gold mirror surface and increase the signal-to-noise ratio of the spectra, the Teflon reflection cell was replaced with a linear gas flow cell (Pike Technologies, 10 cm path length) equipped with ZnSe windows and the FTIR absorption spectrum of N_2O_5 was acquired. Time-resolved FTIR spectra of the N_2O_5 flow through the linear cell was acquired and is plotted in Figure 28. To aid in peak assignment, Table 1 summarizes the peaks observed in the FTIR spectrum of the N_2O_5 flow in this work as well as gas-phase N_2O_5 and HNO_3 peaks from previous studies. The peaks observed in this work align closely to the fundamental modes of HNO_3, therefore it is concluded that there is substantial H_2O contamination in the gas line such that the majority of N_2O_5 that is produced is quickly converted to HNO_3. Evidence of small amounts of unreacted N_2O_5 is observed in the low-frequency shoulder of the 1310 cm^{-1} peak and in the broadness of the 1710 cm^{-1} peak. There are two peaks in the N_2O_5

FTIR spectrum that cannot be accounted for by comparing to previous reports of N_2O_5 and HNO_3. These peaks occur as a negative band at 1560 cm^{-1} and a positive band at 1495 cm^{-1}. As demonstrated in Figure 46 in Appendix C, these peaks remain unchanged upon purging N_2O_5 from the cell. We then hypothesize that these peaks result from adsorbed species on the ZnSe windows due to the high concentrations of HNO_3. Another notable observation from Figure 28 is that the negative bands observed at 900, 1150, and 1250 cm^{-1} in the IRRAS spectrum of N_2O_5 over the gold mirror are absent in the linear spectra. This observation supports the conclusion that these bands were due to adsorbed NO_2 on the gold mirror surface.
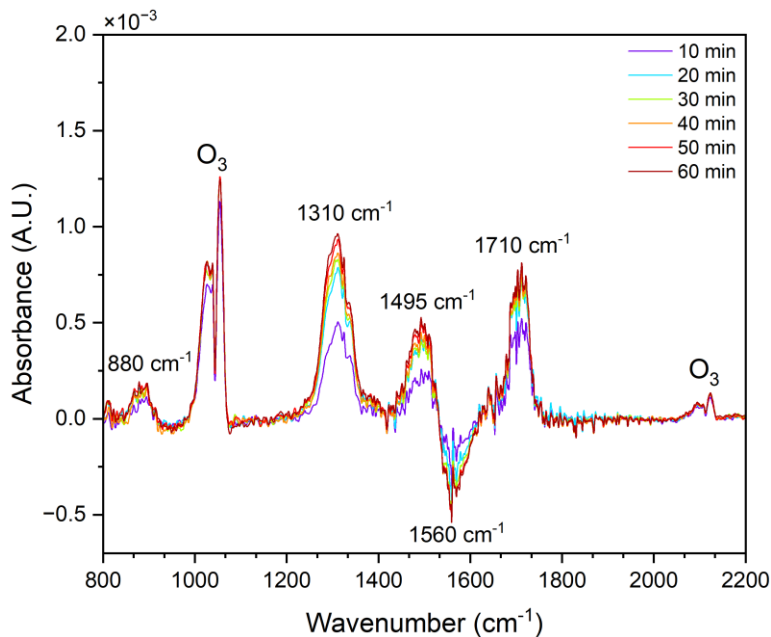
Figure 28. Time-resolved FTIR spectra N_2O_5 flow through the linear absorption cell equipped with ZnSe windows.

Table 1. Summary of the peaks observed in the linear FTIR spectrum of N_2O_5 in this work as well as in previous literature. The normal modes of HNO_3 from previous studies are included as well.

This Work (cm^{-1})	N_2O_5[189,191,192] (cm^{-1})	Assignment	HNO_3[190,193] (cm^{-1})	Assignment
880	743	NO_2 def.	879	NO_2 bend
1310	1246	N-O sym. str.	1303	H-ON bend
1495	1420	NO_2^+	1326	NO_2 sym. str.
1560 (neg.)	2386	NO_3^-	1710	NO_2 asym. str
1710	1720	N-O asym. str.		

The FTIR spectrum in Figure 28 demonstrates that there is significant water contamination within the gas system, leading to the formation of more HNO_3 than expected. As a result, the spectroscopic signatures of N_2O_5 cannot be resolved from those belonging to HNO_3. The concentration of HNO_3 must be significantly reduced in order for the charge separation stabilization at organic interfaces to be accurately determined. It is expected that the pressurization of the NO_2 line when it is not in use is a strong contributor to the excess water within the system. One solution to this issue is to replace the two-way valve that currently connects the NO_2 line to the reaction chamber with a three-way valve and directly connect the NO_2 line to exhaust. The NO_2 could then be continuously flowed through the lines to exhaust without flowing over the liquid surface during purging. Another potential solution for excess water in the system is wrapping the Teflon tubing and glass traps with heat tape to elevate the temperature, facilitating the evaporation and removal of adsorbed water. The temperature instability of N_2O_5 should be considered when using this method and appropriate temperatures should be chosen, or the heating should only be used during purging. Previous efforts have been taken to dry the NO_2 flow including replacing the nylon in the HNO_3 trap with 3Å molecular sieves. As demonstrated

in Figure 47 in Appendix C, the sieves adsorbed both water and NO_2, therefore they are not a viable solution.

The interaction of the HNO_3/N_2O_5 gas flow generated from this setup with the liquid surfaces of PC and DES was investigated. Experiments were carried out in the same manner as described above for the initial studies where KBr windows were used. Figure 29a shows the IRRAS spectrum of the DES surface during 60 min of N_2O_5 flow (green). To aid in the assignment of the peaks observed in the IRRAS spectrum, the linear FTIR spectrum of the gas flow is overlaid on the IRRAS spectrum (purple). All of the peaks observed in the linear FTIR spectrum of the gas flow also occur, albeit at much lower intensities, in the IRRAS spectrum of DES. The observation of these peaks in the IRRAS spectrum could be due to their presence in the gas phase, interfacial trapping of the gas molecules at the liquid surface, adsorption to the optical windows, or a convolution of all three. It is difficult to conclusively determine the origin, however the spectrum after 90 minutes of purging N_2O_5 from the system provides some insight (Figure 29b, light green). The peaks at 1310, 1495, and 1560 cm^{-1} do not decrease in intensity upon purging the HNO_3/N_2O_5 gas from the system. This observation indicates that these species are either adsorbed to the windows or chemisorbed to the liquid surface. The 1710 cm^{-1} peak, which has a very low intensity in the IRRAS spectrum does appear to decrease upon purging, indicating a species in the gas phase or physisorbed to the liquid surface. The band centered at ~1030 cm^{-1} in the IRRAS spectrum of DES + N_2O_5 is conclusively assigned to gas-phase O_3 and decreases completely upon purging. An additional peak is observed in the DES IRRAS spectrum during N_2O_5 flow that is not observed in the spectrum of the gas alone.

89

This peak is centered at ~ 1750 cm^{-1} and has a doublet structure. It is assigned to the carbonyl mode of DES and occurs in the IRRAS spectrum due to the interaction of the gas molecules with the interface. This perturbation is also observed when NO$_2$ is flowed over the DES surface and is discussed in Chapter 4 of this document.
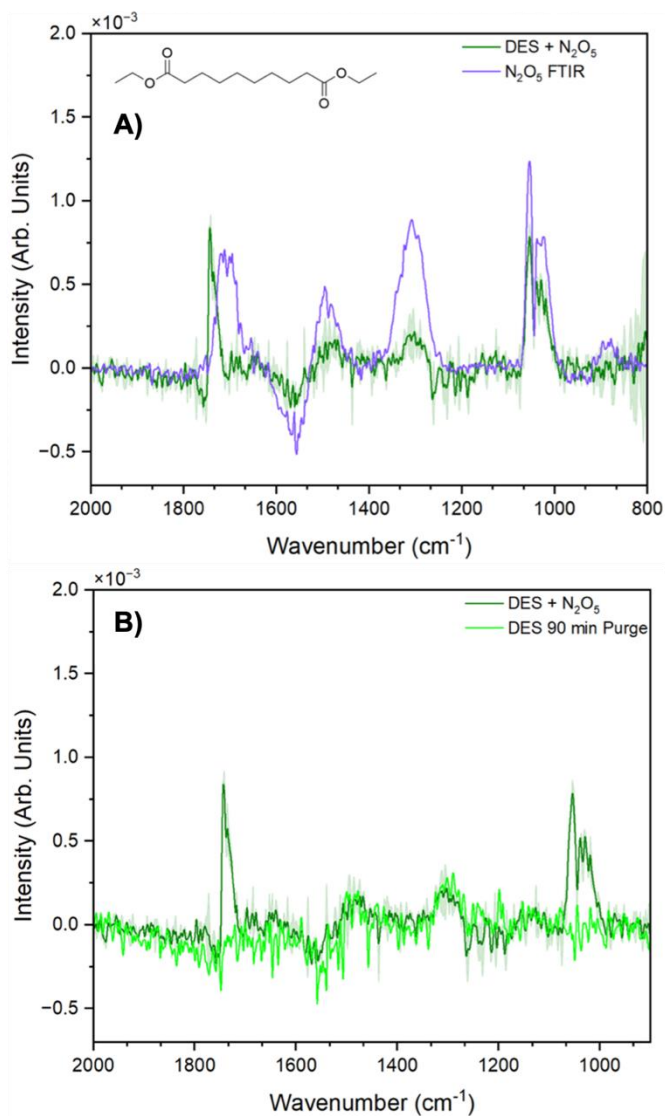
Figure 29. IRRAS spectrum of the DES surface after 60 min HNO$_3$/N$_2$O$_5$ flow (panels A & B, dark green). The linear FTIR spectrum of the gas mixture is included in panel A (purple) for comparison. The IRRAS spectrum of the DES surface after the gas mixture had been purged from the system with N$_2$ and air for 90 min is plotted in panel B (light green). Spectra are an average of two replicates and the standard deviation is plotted as shading.

The IRRAS spectrum of the PC surface during 60 min flow of the HNO_3/N_2O_5 gas mixture is given in Figure 30 (blue). The DES IRRAS spectrum from Figure 29 is also included for comparison (green). When the HNO_3/N_2O_5 gas mixture interacts with the liquid surface, the same peaks are observed in the IRRAS spectrum for both PC and DES. The carbonyl band for PC is blue-shifted from that of DES in the bulk and in the IRRAS spectrum. These results demonstrate that the HNO_3/N_2O_5 gas mixture interacts primarily with the carbonyl group of both organics. Future work should focus on this interaction after purification of the N_2O_5 gas flow as it could have implications in the charge separation stabilization and reactive uptake of N_2O_5 at carbonyl-containing organic interfaces.
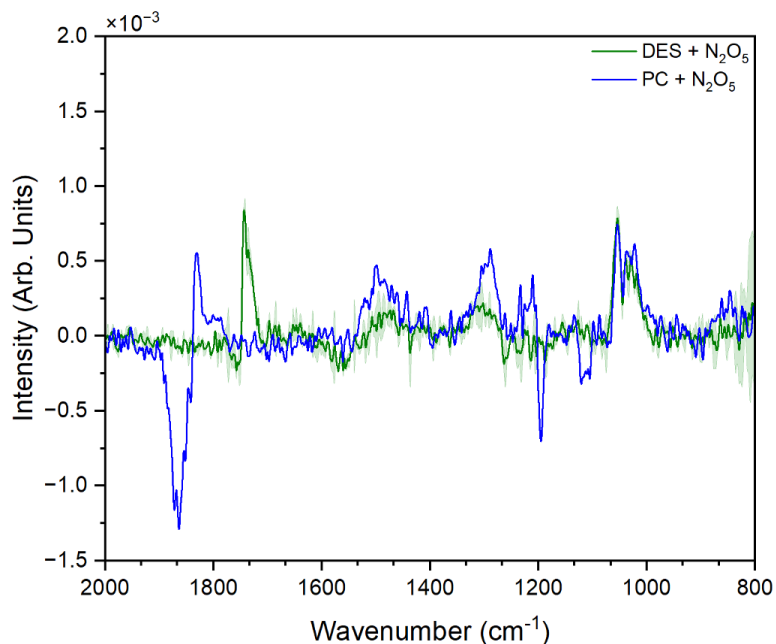
Figure 30. IRRAS spectrum of the PC surface after 60 min HNO_3/N_2O_5 flow (blue). The IRRAS spectrum of the DES surface after 60 min HNO_3/N_2O_5 flow (green) is included for comparison.

5.4 Conclusions

This work describes the progress made towards synthesizing N_2O_5 and reacting it at select organic interfaces with the goal of understanding interfacial charge separation

stabilization. The design and construction of the novel gas synthesis system is described in detail. Initial experiments were conducted to characterize the gas flow produced and identify the ability of IRRAS to inform on perturbations to the liquid surface by the gas-phase molecules. The KBr windows initially used in the IRRAS cell were shown to react with the N_2O_5 gas flow, likely forming and accumulating both $BrNO_2$ and HNO_3. ZnSe was identified as the suitable material for the optical windows based on literature and experiments. A linear FTIR cell was used to characterize the N_2O_5 flow, and it was determined that the flow consists primarily of HNO_3, with small amounts of unreacted N_2O_5. The extent of HNO_3 production is due to water contamination within the gas lines and the sample cell. Potential solutions to eliminate this contamination are discussed. Preliminary observations of the N_2O_5 flow over the surface of PC and DES demonstrate a reversible perturbation to the carbonyl mode, much like that observed when the liquid are exposed to NO_2 as reported in Chapter 4. The interaction of N_2O_5 with surface carbonyl groups should be further explored in future works.

References

(1)   Finlayson-Pitts, B. J.; Pitts, J. N. *Chemistry of the Upper and Lower Atmosphere: Theory, Experiments, and Applications*; Academic Press: San Diego, CA, 2000.

(2)   Ritchie, G. *Atmospheric Chemistry: From The Surface To The Stratosphere*; World Scientific Publishing: New Jersey, 2016.

(3)   Huang, Y.; Mahrt, F.; Xu, S.; Shiraiwa, M.; Zuend, A.; Bertram, A. K. Coexistence of Three Liquid Phases in Individual Atmospheric Aerosol Particles. *PNAS* **2021**, *118* (16). https://doi.org/10.1073/pnas.2102512118.

(4)   Lohmann, U.; Feichter, J. Global Indirect Aerosol Effects: A Review. *Atmospheric Chemistry and Physics* **2005**, *5* (3), 715–737. https://doi.org/10.5194/acp-5-715-2005.

(5)   Morawska, L.; Allen, J.; Bahnfleth, W.; Bluyssen, P. M.; Boerstra, A.; Buonanno, G.; Cao, J.; Dancer, S. J.; Floto, A.; Franchimon, F.; Greenhalgh, T.; Haworth, C.; Hogeling, J.; Isaxon, C.; Jimenez, J. L.; Kurnitski, J.; Li, Y.; Loomans, M.; Marks, G.; Marr, L. C.; Mazzarella, L.; Melikov, A. K.; Miller, S.; Milton, D. K.; Nazaroff, W.; Nielsen, P. V.; Noakes, C.; Peccia, J.; Prather, K.; Querol, X.; Sekhar, C.; Seppänen, O.; Tanabe, S.; Tang, J. W.; Tellier, R.; Tham, K. W.; Wargocki, P.; Wierzbicka, A.; Yao, M. A Paradigm Shift to Combat Indoor Respiratory Infection. *Science* **2021**, *372* (6543), 689–691. https://doi.org/10.1126/science.abg2025.

(6)   Pöschl, U. Atmospheric Aerosols: Composition, Transformation, Climate and Health Effects. *Angewandte Chemie International Edition* **2005**, *44* (46), 7520–7540. https://doi.org/10.1002/anie.200501122.

(7)   Bernstein, J. A.; Alexis, N.; Barnes, C.; Bernstein, I. L.; Nel, A.; Peden, D.; Diaz-Sanchez, D.; Tarlo, S. M.; Williams, P. B.; Bernstein, J. A. Health Effects of Air Pollution. *Journal of Allergy and Clinical Immunology* **2004**, *114* (5), 1116–1123. https://doi.org/10.1016/j.jaci.2004.08.030.

(8)   Lee, L. A.; Reddington, C. L.; Carslaw, K. S. On the Relationship between Aerosol Model Uncertainty and Radiative Forcing Uncertainty. *PNAS* **2016**, *113* (21), 5820–5827. https://doi.org/10.1073/pnas.1507050113.

(9)   Visioni, D.; MacMartin, D. G.; Kravitz, B.; Boucher, O.; Jones, A.; Lurton, T.; Martine, M.; Mills, M. J.; Nabat, P.; Niemeier, U.; Séférian, R.; Tilmes, S. Identifying the Sources of Uncertainty in Climate Model Simulations of Solar Radiation Modification with the G6sulfur and G6solar Geoengineering Model Intercomparison Project (GeoMIP) Simulations. *Atmospheric Chemistry and Physics* **2021**, *21* (13), 10039–10063. https://doi.org/10.5194/acp-21-10039-2021.

(10) Murphy, D. M.; Cziczo, D. J.; Froyd, K. D.; Hudson, P. K.; Matthew, B. M.; Middlebrook, A. M.; Peltier, R. E.; Sullivan, A.; Thomson, D. S.; Weber, R. J.

Single-Particle Mass Spectrometry of Tropospheric Aerosol Particles. *Journal of Geophysical Research: Atmospheres* **2006**, *111* (D23). https://doi.org/10.1029/2006JD007340.

(11) Zhang, Q.; Jimenez, J. L.; Canagaratna, M. R.; Allan, J. D.; Coe, H.; Ulbrich, I.; Alfarra, M. R.; Takami, A.; Middlebrook, A. M.; Sun, Y. L.; Dzepina, K.; Dunlea, E.; Docherty, K.; DeCarlo, P. F.; Salcedo, D.; Onasch, T.; Jayne, J. T.; Miyoshi, T.; Shimono, A.; Hatakeyama, S.; Takegawa, N.; Kondo, Y.; Schneider, J.; Drewnick, F.; Borrmann, S.; Weimer, S.; Demerjian, K.; Williams, P.; Bower, K.; Bahreini, R.; Cottrell, L.; Griffin, R. J.; Rautiainen, J.; Sun, J. Y.; Zhang, Y. M.; Worsnop, D. R. Ubiquity and Dominance of Oxygenated Species in Organic Aerosols in Anthropogenically-Influenced Northern Hemisphere Midlatitudes. *Geophysical Research Letters* **2007**, *34* (13). https://doi.org/10.1029/2007GL029979.

(12) Kanakidou, M.; Seinfeld, J. H.; Pandis, S. N.; Barnes, I.; Dentener, F. J.; Facchini, M. C.; Van Dingenen, R.; Ervens, B.; Nenes, A.; Nielsen, C. J.; Swietlicki, E.; Putaud, J. P.; Balkanski, Y.; Fuzzi, S.; Horth, J.; Moortgat, G. K.; Winterhalter, R.; Myhre, C. E. L.; Tsigaridis, K.; Vignati, E.; Stephanou, E. G.; Wilson, J. Organic Aerosol and Global Climate Modelling: A Review. *Atmospheric Chemistry and Physics* **2005**, *5* (4), 1053–1123. https://doi.org/10.5194/acp-5-1053-2005.

(13) Schmedding, R.; Rasool, Q. Z.; Zhang, Y.; Pye, H. O. T.; Zhang, H.; Chen, Y.; Surratt, J. D.; Lopez-Hilfiker, F. D.; Thornton, J. A.; Goldstein, A. H.; Vizuete, W. Predicting Secondary Organic Aerosol Phase State and Viscosity and Its Effect on Multiphase Chemistry in a Regional-Scale Air Quality Model. *Atmospheric Chemistry and Physics* **2020**, *20* (13), 8201–8225. https://doi.org/10.5194/acp-20-8201-2020.

(14) You, Y.; Smith, M. L.; Song, M.; Martin, S. T.; Bertram, A. K. Liquid–Liquid Phase Separation in Atmospherically Relevant Particles Consisting of Organic Species and Inorganic Salts. *International Reviews in Physical Chemistry* **2014**, *33* (1), 43–77. https://doi.org/10.1080/0144235X.2014.890786.

(15) Song, M.; Marcolli, C.; Krieger, U. K.; Zuend, A.; Peter, T. Liquid-Liquid Phase Separation in Aerosol Particles: Dependence on O:C, Organic Functionalities, and Compositional Complexity. *Geophysical Research Letters* **2012**, *39* (19). https://doi.org/10.1029/2012GL052807.

(16) Corti, H. R.; Appignanesi, G. A.; Barbosa, M. C.; Bordin, J. R.; Calero, C.; Camisasca, G.; Elola, M. D.; Franzese, G.; Gallo, P.; Hassanali, A.; Huang, K.; Laria, D.; Menéndez, C. A.; de Oca, J. M. M.; Longinotti, M. P.; Rodriguez, J.; Rovere, M.; Scherlis, D.; Szleifer, I. Structure and Dynamics of Nanoconfined Water and Aqueous Solutions. *Eur. Phys. J. E* **2021**, *44* (11), 136. https://doi.org/10.1140/epje/s10189-021-00136-4.

(17) Fayer, M. D.; Levinger, N. E. Analysis of Water in Confined Geometries and at Interfaces. *Annual Review of Analytical Chemistry* **2010**, *3* (1), 89–107. https://doi.org/10.1146/annurev-anchem-070109-103410.

(18) Crupi, V.; Interdonato, S.; Longo, F.; Majolino, D.; Migliardo, P.; Venuti, V. A New Insight on the Hydrogen Bonding Structures of Nanoconfined Water: A Raman

Study. *Journal of Raman Spectroscopy* **2008**, *39* (2), 244–249. https://doi.org/10.1002/jrs.1857.

(19) Liu, T.; Abbatt, J. P. D. Oxidation of Sulfur Dioxide by Nitrogen Dioxide Accelerated at the Interface of Deliquesced Aerosol Particles. *Nat. Chem.* **2021**, *13* (12), 1173–1177. https://doi.org/10.1038/s41557-021-00777-0.

(20) Weis, D. D.; Ewing, G. E. The Reaction of Nitrogen Dioxide with Sea Salt Aerosol. *J. Phys. Chem. A* **1999**, *103* (25), 4865–4873. https://doi.org/10.1021/jp984488q.

(21) Finlayson-Pitts, B. J. Reaction of NO2 with NaCl and Atmospheric Implications of NOCl Formation. *Nature* **1983**, *306* (5944), 676–677. https://doi.org/10.1038/306676a0.

(22) Murdachaew, G.; Varner, M. E.; Phillips, L. F.; Finlayson-Pitts, B. J.; Gerber, R. B. Nitrogen Dioxide at the Air–Water Interface: Trapping, Absorption, and Solvation in the Bulk and at the Surface. *Phys. Chem. Chem. Phys.* **2012**, *15* (1), 204–212. https://doi.org/10.1039/C2CP42810E.

(23) Lin, Y.-H.; Zhang, H.; Pye, H. O. T.; Zhang, Z.; Marth, W. J.; Park, S.; Arashiro, M.; Cui, T.; Budisulistiorini, S. H.; Sexton, K. G.; Vizuete, W.; Xie, Y.; Luecken, D. J.; Piletic, I. R.; Edney, E. O.; Bartolotti, L. J.; Gold, A.; Surratt, J. D. Epoxide as a Precursor to Secondary Organic Aerosol Formation from Isoprene Photooxidation in the Presence of Nitrogen Oxides. *Proceedings of the National Academy of Sciences* **2013**, *110* (17), 6718–6723. https://doi.org/10.1073/pnas.1221150110.

(24) Edwards, K. C.; Klodt, A. L.; Galeazzo, T.; Schervish, M.; Wei, J.; Fang, T.; Donahue, N. M.; Aumont, B.; Nizkorodov, S. A.; Shiraiwa, M. Effects of Nitrogen Oxides on the Production of Reactive Oxygen Species and Environmentally Persistent Free Radicals from α-Pinene and Naphthalene Secondary Organic Aerosols. *J. Phys. Chem. A* **2022**, *126* (40), 7361–7372. https://doi.org/10.1021/acs.jpca.2c05532.

(25) Zang, X.; Zhang, Z.; Zhao, Y.; Li, G.; Xie, H.; Zhang, W.; Wu, G.; Yang, X.; Jiang, L. Effects of NO2 and SO2 on the Secondary Organic Aerosol Formation from β-Pinene Photooxidation. *Journal of Environmental Sciences* **2024**, *136*, 151–160. https://doi.org/10.1016/j.jes.2022.10.040.

(26) Ziemann, P. J.; Atkinson, R. Kinetics, Products, and Mechanisms of Secondary Organic Aerosol Formation. *Chem. Soc. Rev.* **2012**, *41* (19), 6582–6605. https://doi.org/10.1039/C2CS35122F.

(27) Zhao, D.; Schmitt, S. H.; Wang, M.; Acir, I.-H.; Tillmann, R.; Tan, Z.; Novelli, A.; Fuchs, H.; Pullinen, I.; Wegener, R.; Rohrer, F.; Wildt, J.; Kiendler-Scharr, A.; Wahner, A.; Mentel, T. F. Effects of NO_x and SO_2 on the Secondary Organic Aerosol Formation from Photooxidation of *α*-Pinene and Limonene. *Atmospheric Chemistry and Physics* **2018**, *18* (3), 1611–1628. https://doi.org/10.5194/acp-18-1611-2018.

(28) Galib, M.; Limmer, D. T. Reactive Uptake of N_2O_5 by Atmospheric Aerosol Is Dominated by Interfacial Processes. *Science* **2021**, *371* (6532), 921–925. https://doi.org/10.1126/science.abd7716.

(29) Gross, S.; Iannone, R.; Xiao, S.; Bertram, A. K. Reactive Uptake Studies of NO3 and N2O5 on Alkenoic Acid, Alkanoate, and Polyalcohol Substrates to Probe

Nighttime Aerosol Chemistry. *Phys. Chem. Chem. Phys.* **2009**, *11* (36), 7792–7803. https://doi.org/10.1039/B904741G.

(30) Cosman, L. M.; Knopf, D. A.; Bertram, A. K. N2O5 Reactive Uptake on Aqueous Sulfuric Acid Solutions Coated with Branched and Straight-Chain Insoluble Organic Surfactants. *J. Phys. Chem. A* **2008**, *112* (11), 2386–2396. https://doi.org/10.1021/jp710685r.

(31) Cosman, L. M.; Bertram, A. K. Reactive Uptake of N2O5 on Aqueous H2SO4 Solutions Coated with 1-Component and 2-Component Monolayers. *J. Phys. Chem. A* **2008**, *112* (20), 4625–4635. https://doi.org/10.1021/jp8005469.

(32) Park, S.-C.; Burden, D. K.; Nathanson, G. M. The Inhibition of N2O5 Hydrolysis in Sulfuric Acid by 1-Butanol and 1-Hexanol Surfactant Coatings. *J. Phys. Chem. A* **2007**, *111* (15), 2921–2929. https://doi.org/10.1021/jp068228h.

(33) Iannone, R.; Xiao, S.; Bertram, A. K. Potentially Important Nighttime Heterogeneous Chemistry: NO3 with Aldehydes and N2O5 with Alcohols. *Phys. Chem. Chem. Phys.* **2011**, *13* (21), 10214–10223. https://doi.org/10.1039/C1CP20294D.

(34) Griffiths, P. T.; Badger, C. L.; Cox, R. A.; Folkers, M.; Henk, H. H.; Mentel, T. F. Reactive Uptake of N2O5 by Aerosols Containing Dicarboxylic Acids. Effect of Particle Phase, Composition, and Nitrate Content. *J. Phys. Chem. A* **2009**, *113* (17), 5082–5090. https://doi.org/10.1021/jp8096814.

(35) Hollas, J. M. *Modern Spectroscopy*, 4th ed.; Wiley, 2004.

(36) Skoog, D. A.; Holler, F. J.; Crouch, S. R. *Principles of Instrumental Analysis*, 7th ed.; Cengage Learning: Boston, MA, 2018.

(37) Ingle Jr., J. D.; Crouch, S. R. *Spectrochemical Analysis*; Prentice Hall: Upper Saddle River, New Jersey, 1988.

(38) Mirabella, F. *Modern Techniques in Applied Molecular Spectroscopy*; Techniques in Analytical Chemistry; Wiley: New York, NY, 1998.

(39) Neal, J. F.; Zhao, W.; Grooms, A. J.; Flood, A. H.; Allen, H. C. Arginine–Phosphate Recognition Enhanced in Phospholipid Monolayers at Aqueous Interfaces. *J. Phys. Chem. C* **2018**, *122* (46), 26362–26371. https://doi.org/10.1021/acs.jpcc.8b03531.

(40) Vazquez de Vasquez, M. G.; Carter-Fenk, K. A.; McCaslin, L. M.; Beasley, E. E.; Clark, J. B.; Allen, H. C. Hydration and Hydrogen Bond Order of Octadecanoic Acid and Octadecanol Films on Water at 21 and 1 °C. *J. Phys. Chem. A* **2021**, *125* (46), 10065–10078. https://doi.org/10.1021/acs.jpca.1c06101.

(41) Enders, A. A.; Clark, J. B.; Elliott, S. M.; Allen, H. C. New Insights into Cation- and Temperature-Driven Protein Adsorption to the Air–Water Interface through Infrared Reflection Studies of Bovine Serum Albumin. *Langmuir* **2023**, *39* (15), 5505–5513. https://doi.org/10.1021/acs.langmuir.3c00249.

(42) Voss, L. F.; Bazerbashi, M. F.; Beekman, C. P.; Hadad, C. M.; Allen, H. C. Oxidation of Oleic Acid at Air/Liquid Interfaces. *Journal of Geophysical Research: Atmospheres* **2007**, *112* (D6). https://doi.org/10.1029/2006JD007677.

(43) North, N. M.; Enders, A. A. A.; Clark, J. B.; Duah, K. A.; Allen, H. C. Saccharide Concentration Prediction from Proxy Ocean Samples Analyzed Via Infrared

Spectroscopy and Quantitative Machine Learning. *ACS Earth Space Chem.* **2024**. https://doi.org/10.1021/acsearthspacechem.3c00310.

(44) Auvil, N. C.; Vazquez de Vasquez, M. G.; Allen, H. C. Zinc–Carboxylate Binding in Mixed Octadecanoic Acid and Octadecanol Monolayers on Proxy Seawater Solution Surfaces. *ACS Earth Space Chem.* **2021**, *5* (10), 2947–2956. https://doi.org/10.1021/acsearthspacechem.1c00272.

(45) Mendelsohn, R.; Mao, G.; Flach, C. R. Infrared Reflection–Absorption Spectroscopy: Principles and Applications to Lipid–Protein Interaction in Langmuir Films. *Biochimica et Biophysica Acta (BBA) - Biomembranes* **2010**, *1798* (4), 788–800. https://doi.org/10.1016/j.bbamem.2009.11.024.

(46) Flach, C. R.; Gericke, A.; Mendelsohn, R. Quantitative Determination of Molecular Chain Tilt Angles in Monolayer Films at the Air/Water Interface: Infrared Reflection/Absorption Spectroscopy of Behenic Acid Methyl Ester. *J. Phys. Chem. B* **1997**, *101* (1), 58–65. https://doi.org/10.1021/jp962288d.

(47) Gericke, A.; Flach, C. R.; Mendelsohn, R. Structure and Orientation of Lung Surfactant SP-C and L-Alpha-Dipalmitoylphosphatidylcholine in Aqueous Monolayers. *Biophys J* **1997**, *73* (1), 492–499.

(48) Carter-Fenk, K. A.; Dommer, A. C.; Fiamingo, M. E.; Kim, J.; Amaro, R. E.; Allen, H. C. Calcium Bridging Drives Polysaccharide Co-Adsorption to a Proxy Sea Surface Microlayer. *Phys. Chem. Chem. Phys.* **2021**, *23* (30), 16401–16416. https://doi.org/10.1039/D1CP01407B.

(49) Meinders, M. B.; van den Bosch, G. G.; de Jongh, H. H. Adsorption Properties of Proteins at and near the Air/Water Interface from IRRAS Spectra of Protein Solutions. *Eur Biophys J* **2001**, *30* (4), 256–267. https://doi.org/10.1007/s002490000124.

(50) Horn, A. B.; Koch, T.; Chesters, M. A.; McCoustra, M. R. S.; Sodeau, J. R. A Low-Temperature Infrared Study of the Reactions of the Stratospheric NOy Reservoir Species Dinitrogen Pentoxide with Water Ice, 80-160 K. *J. Phys. Chem.* **1994**, *98* (3), 946–951. https://doi.org/10.1021/j100054a034.

(51) Born, M.; Wolf, E. *Principles of Optics: Electromagnetic Theory of Propagation, Interference, and Diffraction of Light*, 5th ed.; Pergamom Press: Oxford, New York, 1975.

(52) Ball, P. Water — an Enduring Mystery. *Nature* **2008**, *452* (7185), 291–292. https://doi.org/10.1038/452291a.

(53) Nilsson, A.; Pettersson, L. G. M. The Structural Origin of Anomalous Properties of Liquid Water. *Nat Commun* **2015**, *6* (1), 8998. https://doi.org/10.1038/ncomms9998.

(54) Shultz, M. J.; Baldelli, S.; Schnitzer, C.; Simonelli, D. Water Confined at the Liquid-Air Interface. In *Water in Confining Geometries*; Buch, V., Devlin, J. P., Eds.; Springer Series in Cluster Physics; Springer: Berlin, Heidelberg, 2003; pp 249–273. https://doi.org/10.1007/978-3-662-05231-0_12.

(55) Plastinin, I. V.; Burikov, S. A.; Dolenko, T. A. Laser Diagnostics of Reverse Microemulsions: Influence of the Size and Shape of Reverse Micelles on the Raman Spectrum on the Example of Water/AOT/Cyclohexane System. *Journal of*

Molecular Liquids **2021**, *325*, 115153. https://doi.org/10.1016/j.molliq.2020.115153.

(56) Agrawal, K. V.; Shimizu, S.; Drahushuk, L. W.; Kilcoyne, D.; Strano, M. S. Observation of Extreme Phase Transition Temperatures of Water Confined inside Isolated Carbon Nanotubes. *Nat Nanotechnol* **2017**, *12* (3), 267–273. https://doi.org/10.1038/nnano.2016.254.

(57) Ma, X.; Cambré, S.; Wenseleers, W.; Doorn, S. K.; Htoon, H. Quasiphase Transition in a Single File of Water Molecules Encapsulated in (6,5) Carbon Nanotubes Observed by Temperature-Dependent Photoluminescence Spectroscopy. *Phys. Rev. Lett.* **2017**, *118* (2), 027402. https://doi.org/10.1103/PhysRevLett.118.027402.

(58) Rieth, A. J.; Hunter, K. M.; Dincă, M.; Paesani, F. Hydrogen Bonding Structure of Confined Water Templated by a Metal-Organic Framework with Open Metal Sites. *Nat Commun* **2019**, *10* (1), 4771. https://doi.org/10.1038/s41467-019-12751-z.

(59) Hunter, K. M.; Wagner, J. C.; Kalaj, M.; Cohen, S. M.; Xiong, W.; Paesani, F. Simulation Meets Experiment: Unraveling the Properties of Water in Metal–Organic Frameworks through Vibrational Spectroscopy. *J. Phys. Chem. C* **2021**, *125* (22), 12451–12460. https://doi.org/10.1021/acs.jpcc.1c03145.

(60) Cogley, D. R.; Falk, M.; Butler, J. N.; Grunwald, E. Solvation and Self-Association of Water in Propylene Carbonate. *J. Phys. Chem.* **1972**, *76* (6), 855–864. https://doi.org/10.1021/j100650a011.

(61) Scherer, J. R.; Go, M. K.; Kint, S. Raman Spectra and Structure of Water in Dimethyl Sulfoxide. *J. Phys. Chem.* **1973**, *77* (17), 2108–2117. https://doi.org/10.1021/j100636a016.

(62) Dei, L.; Grassi, S. Peculiar Properties of Water as Solute. *J. Phys. Chem. B* **2006**, *110* (24), 12191–12197. https://doi.org/10.1021/jp060633l.

(63) Silva, P. L.; Bastos, E. L.; El Seoud, O. A. Solvation in Binary Mixtures of Water and Polar Aprotic Solvents: Theoretical Calculations of the Concentrations of Solvent−Water Hydrogen-Bonded Species and Application to Thermosolvatochromism of Polarity Probes. *J. Phys. Chem. B* **2007**, *111* (22), 6173–6180. https://doi.org/10.1021/jp068596l.

(64) Abe, H.; Yoshiichi, Y.; Hirano, T.; Ohkubo, T.; Kishimura, H. Hydrogen Bonding of Nanoconfined Water in Ionic Liquids. *Journal of Molecular Liquids* **2022**, 120383. https://doi.org/10.1016/j.molliq.2022.120383.

(65) Abe, H.; Takekiyo, T.; Yoshimura, Y.; Shimizu, A. Static and Dynamic Properties of Nano-Confined Water in Room-Temperature Ionic Liquids. *Journal of Molecular Liquids* **2019**, *290*, 111216. https://doi.org/10.1016/j.molliq.2019.111216.

(66) Yoshimura, Y.; Mori, T.; Kaneko, K.; Nogami, K.; Takekiyo, T.; Masuda, Y.; Shimizu, A. Confirmation of Local Water Structure Confined in Ionic Liquids Using H/D Exchange. *Journal of Molecular Liquids* **2019**, *286*, 110874. https://doi.org/10.1016/j.molliq.2019.04.151.

(67) Zhang, Z.; Zhang, Y.; Du, B.; Peng, Z. Liquid-like Poly(Ionic Liquid) as Electrolyte for Thermally Stable Lithium-Ion Battery. *ACS Omega* **2018**, *3* (9), 10564–10571. https://doi.org/10.1021/acsomega.8b01539.

(68)   Mukherjee, K.; Palchowdhury, S.; Maroncelli, M. OH Stretching and Libration Bands of Solitary Water in Ionic Liquids and Dipolar Solvents Share a Single Dependence on Solvent Polarity. *J. Phys. Chem. B* **2022**, *126* (24), 4584–4598. https://doi.org/10.1021/acs.jpcb.2c02445.

(69)   Palchowdhury, S.; Mukherjee, K.; Maroncelli, M. Rapid Water Dynamics Structures the OH-Stretching Spectra of Solitary Water in Ionic Liquids and Dipolar Solvents. *The Journal of Chemical Physics* **2022**, *157* (8), 084502. https://doi.org/10.1063/5.0107348.

(70)   Zhong, X.; Fan, Z.; Liu, Z.; Cao, D. Local Structure Evolution and Its Connection to Thermodynamic and Transport Properties of 1-Butyl-3-Methylimidazolium Tetrafluoroborate and Water Mixtures by Molecular Dynamics Simulations. *J. Phys. Chem. B* **2012**, *116* (10), 3249–3263. https://doi.org/10.1021/jp3001543.

(71)   Hayes, R.; Imberti, S.; Warr, G. G.; Atkin, R. How Water Dissolves in Protic Ionic Liquids. *Angewandte Chemie International Edition* **2012**, *51* (30), 7468–7471. https://doi.org/10.1002/anie.201201973.

(72)   Dickens, B.; Dickens, S. H. Estimation of Concentration and Bonding Environment of Water Dissolved in Common Solvents Using Near Infrared Absorptivity. *J Res Natl Inst Stand Technol* **1999**, *104* (2), 173–183.

(73)   Ivanov, E. V.; Lebedeva, E. Yu. Volumetric Properties of H2O and D2O Solutions in Propylene Carbonate at T=(278.15, 288.15, 298.15, 308.15, and 318.15) K under Atmospheric Pressure. *Journal of Molecular Liquids* **2011**, *159* (2), 124–131. https://doi.org/10.1016/j.molliq.2010.12.009.

(74)   Bonner, O. D.; Choi, Y. S. Hydrogen Bonding of Water in Organic Solvents. II. Change of Water Structure with Composition. *J. Phys. Chem.* **1974**, *78* (17), 1727–1731. https://doi.org/10.1021/j100610a010.

(75)   Johnson, J. R.; Christian, S. D.; Affsprung, H. E. The Molecular Complexity of Water in Organic Solvents. Part III. *J. Chem. Soc. A* **1967**, No. 0, 1924–1928. https://doi.org/10.1039/J19670001924.

(76)   Christian, S. D.; Taha, A. A.; Gash, B. W. Molecular Complexes of Water in Organic Solvents and in the Vapour Phase. *Q. Rev., Chem. Soc.* **1970**, *24* (1), 20. https://doi.org/10.1039/qr9702400020.

(77)   Glew, D. N.; Rath, N. S. H2O, HDO, and CH3OH Infrared Spectra and Correlation with Solvent Basicity and Hydrogen Bonding. *Can. J. Chem.* **1971**, *49* (6), 837–856. https://doi.org/10.1139/v71-142.

(78)   Kuo, M.; Kamelamela, N.; Shultz, M. J. Rotational Structure of Water in a Hydrophobic Environment: Carbon Tetrachloride. *J. Phys. Chem. A* **2008**, *112* (6), 1214–1218. https://doi.org/10.1021/jp7097284.

(79)   Liang, C.; Kwak, K.; Cho, M. Revealing the Solvation Structure and Dynamics of Carbonate Electrolytes in Lithium-Ion Batteries by Two-Dimensional Infrared Spectrum Modeling. *J. Phys. Chem. Lett.* **2017**, *8* (23), 5779–5784. https://doi.org/10.1021/acs.jpclett.7b02623.

(80)   Hayes, R.; Warr, G. G.; Atkin, R. Structure and Nanostructure in Ionic Liquids. *Chem. Rev.* **2015**, *115* (13), 6357–6426. https://doi.org/10.1021/cr500411q.

(81) Giorgini, M. G.; Futamatagawa, K.; Torii, H.; Musso, M.; Cerini, S. Solvation Structure around the Li+ Ion in Mixed Cyclic/Linear Carbonate Solutions Unveiled by the Raman Noncoincidence Effect. *J. Phys. Chem. Lett.* **2015**, *6* (16), 3296–3302. https://doi.org/10.1021/acs.jpclett.5b01524.

(82) Naji, A.; Ghanbaja, J.; Willmann, P.; Billaud, D. New Halogenated Additives to Propylene Carbonate-Based Electrolytes for Lithium-Ion Batteries. *Electrochimica Acta* **2000**, *45* (12), 1893–1899. https://doi.org/10.1016/S0013-4686(99)00410-7.

(83) Tasaki, K.; Goldberg, A.; Winter, M. On the Difference in Cycling Behaviors of Lithium-Ion Battery Cell between the Ethylene Carbonate- and Propylene Carbonate-Based Electrolytes. *Electrochimica Acta* **2011**, *56* (28), 10424–10435. https://doi.org/10.1016/j.electacta.2011.05.112.

(84) Aurbach, D.; Zaban, A. Impedance Spectroscopy of Lithium Electrodes: Part 1. General Behavior in Propylene Carbonate Solutions and the Correlation to Surface Chemistry and Cycling Efficiency. *Journal of Electroanalytical Chemistry* **1993**, *348* (1), 155–179. https://doi.org/10.1016/0022-0728(93)80129-6.

(85) Battisti, D.; Nazri, G. A.; Klassen, B.; Aroca, R. Vibrational Studies of Lithium Perchlorate in Propylene Carbonate Solutions. *J. Phys. Chem.* **1993**, *97* (22), 5826–5830. https://doi.org/10.1021/j100124a007.

(86) Xuan, X.; Wang, J.; Tang, J.; Qu, G.; Lu, J. A Vibrational Spectroscopic Study of Ion Solvation in Lithium Perchlorate/Propylene Carbonate Electrolyte. *Physics and Chemistry of Liquids* **2001**, *39* (3), 327–342. https://doi.org/10.1080/00319100108031666.

(87) Brennan, M. D.; Breedon, M.; Best, A. S.; Morishita, T.; Spencer, M. J. S. Surface Reactions of Ethylene Carbonate and Propylene Carbonate on the Li(001) Surface. *Electrochimica Acta* **2017**, *243*, 320–330. https://doi.org/10.1016/j.electacta.2017.04.163.

(88) Fulfer, K. D.; Kuroda, D. G. Solvation Structure and Dynamics of the Lithium Ion in Organic Carbonate-Based Electrolytes: A Time-Dependent Infrared Spectroscopy Study. *J. Phys. Chem. C* **2016**, *120* (42), 24011–24022. https://doi.org/10.1021/acs.jpcc.6b08607.

(89) Fulfer, K. D.; Galle Kankanamge, S. R.; Chen, X.; Woodard, K. T.; Kuroda, D. G. Elucidating the Mechanism behind the Infrared Spectral Features and Dynamics Observed in the Carbonyl Stretch Region of Organic Carbonates Interacting with Lithium Ions. *J. Chem. Phys.* **2021**, *154* (23), 234504. https://doi.org/10.1063/5.0049742.

(90) Stich, M.; Göttlinger, M.; Kurniawan, M.; Schmidt, U.; Bund, A. Hydrolysis of LiPF6 in Carbonate-Based Electrolytes for Lithium-Ion Batteries and in Aqueous Media. *J. Phys. Chem. C* **2018**, *122* (16), 8836–8842. https://doi.org/10.1021/acs.jpcc.8b02080.

(91) Li, W.; Lucht, B. L. Inhibition of the Detrimental Effects of Water Impurities in Lithium-Ion Batteries. *Electrochem. Solid-State Lett.* **2007**, *10* (4), A115. https://doi.org/10.1149/1.2458913.

(92) Hwang, S.; Kim, D.-H.; Shin, J. H.; Jang, J. E.; Ahn, K. H.; Lee, C.; Lee, H. Ionic Conduction and Solution Structure in LiPF6 and LiBF4 Propylene Carbonate

Electrolytes. *J. Phys. Chem. C* **2018**, *122* (34), 19438–19446. https://doi.org/10.1021/acs.jpcc.8b06035.

(93) Wang, J.; Gu, W.; Chen, X.; Yang, M.; Chen, J.; Zhao, M.; Liu, Q.-S. Electrical Conductivity and Refractive Index of Binary Ionic Liquid Mixtures with Diethyl Carbonate, Dimethyl Carbonate and Propylene Carbonate. *Journal of Molecular Liquids* **2023**, *378*, 121598. https://doi.org/10.1016/j.molliq.2023.121598.

(94) Stoppa, A.; Hunger, J.; Buchner, R. Conductivities of Binary Mixtures of Ionic Liquids with Polar Solvents. *J. Chem. Eng. Data* **2009**, *54* (2), 472–479. https://doi.org/10.1021/je800468h.

(95) Matsumoto, R.; Thompson, M. W.; Cummings, P. T. Ion Pairing Controls Physical Properties of Ionic Liquid-Solvent Mixtures. *J. Phys. Chem. B* **2019**, *123* (46), 9944–9955. https://doi.org/10.1021/acs.jpcb.9b08509.

(96) Canongia Lopes, J. N.; Costa Gomes, M. F.; Husson, P.; Pádua, A. A. H.; Rebelo, L. P. N.; Sarraute, S.; Tariq, M. Polarity, Viscosity, and Ionic Conductivity of Liquid Mixtures Containing [C4C1im][Ntf2] and a Molecular Component. *J. Phys. Chem. B* **2011**, *115* (19), 6088–6099. https://doi.org/10.1021/jp2012254.

(97) Muhuri, P. K.; Ghosh, S. K.; Hazra, D. K. Solubilities of Some Alkali-Metal Salts, Tetraphenylarsonium Chloride, and Tetraphenylphosphonium Bromide in Propylene Carbonate at 25.Degree.C Using the Ion-Selective Electrode Technique. *J. Chem. Eng. Data* **1993**, *38* (2), 242–244. https://doi.org/10.1021/je00010a014.

(98) Carey, D. M.; Korenowski, G. M. Measurement of the Raman Spectrum of Liquid Water. *J. Chem. Phys.* **1998**, *108* (7), 2669–2675. https://doi.org/10.1063/1.475659.

(99) Wang, Z.; Pakoulev, A.; Pang, Y.; Dlott, D. D. Vibrational Substructure in the OH Stretching Band of Water. *Chemical Physics Letters* **2003**, *378* (3), 281–288. https://doi.org/10.1016/S0009-2614(03)01267-3.

(100) Sun, Q. The Raman OH Stretching Bands of Liquid Water. *Vibrational Spectroscopy* **2009**, *51* (2), 213–217. https://doi.org/10.1016/j.vibspec.2009.05.002.

(101) Liu, D.; Ma, G.; Levering, L. M.; Allen, H. C. Vibrational Spectroscopy of Aqueous Sodium Halide Solutions and Air−Liquid Interfaces: Observation of Increased Interfacial Depth. *J. Phys. Chem. B* **2004**, *108* (7), 2252–2260. https://doi.org/10.1021/jp036169r.

(102) Kecki, Z.; Sokołowska, A. Crossing of Anisotropic and Isotropic Raman Components in the Intermolecular Resonance Coupling of Vibrations. IV— Methanol Solutions in Acetone. *Journal of Raman Spectroscopy* **1996**, *27* (5), 429–432. https://doi.org/10.1002/(SICI)1097-4555(199605)27:5<429::AID-JRS981>3.0.CO;2-O.

(103) Nicodemus, R. A.; Ramasesha, K.; Roberts, S. T.; Tokmakoff, A. Hydrogen Bond Rearrangements in Water Probed with Temperature-Dependent 2D IR. *J. Phys. Chem. Lett.* **2010**, *1* (7), 1068–1072. https://doi.org/10.1021/jz100138z.

(104) Burikov, S.; Dolenko, T.; Patsaeva, S.; Starokurov, Y.; Yuzhakov, V. Raman and IR Spectroscopy Research on Hydrogen Bonding in Water-Ethanol Systems. *Mol. Phys.* **2010**, *108* (18), 2427–2436. https://doi.org/10.1080/00268976.2010.516277.

(105) Sun, Q. Local Statistical Interpretation for Water Structure. *Chemical Physics Letters* **2013**, *568–569*, 90–94. https://doi.org/10.1016/j.cplett.2013.03.065.

(106) Sun, Q.; Qin, C. Raman OH Stretching Band of Water as an Internal Standard to Determine Carbonate Concentrations. *Chemical Geology* **2011**, *283* (3), 274–278. https://doi.org/10.1016/j.chemgeo.2011.01.025.

(107) Hendrikse, R. L.; Bayly, A. E.; Jimack, P. K.; Lai, X. Using Raman Spectroscopy and Molecular Dynamics to Study Conformation Changes of Sodium Lauryl Ether Sulfate Molecules. *J. Phys. Chem. B* **2023**, *127* (20), 4676–4686. https://doi.org/10.1021/acs.jpcb.3c02022.

(108) Auer, B.; Kumar, R.; Schmidt, J. R.; Skinner, J. L. Hydrogen Bonding and Raman, IR, and 2D-IR Spectroscopy of Dilute HOD in Liquid D2O. *Proceedings of the National Academy of Sciences* **2007**, *104* (36), 14215–14220. https://doi.org/10.1073/pnas.0701482104.

(109) Corcelli, S. A.; Skinner, J. L. Infrared and Raman Line Shapes of Dilute HOD in Liquid H2O and D2O from 10 to 90 C. *The Journal of Physical Chemistry A* **2005**, *109* (28), 6154–6165.

(110) Devlin, J. P.; Sadlej, J.; Buch, V. Infrared Spectra of Large H2O Clusters: New Understanding of the Elusive Bending Mode of Ice. *J. Phys. Chem. A* **2001**, *105* (6), 974–983. https://doi.org/10.1021/jp003455j.

(111) Perakis, F.; De Marco, L.; Shalit, A.; Tang, F.; Kann, Z. R.; Kühne, T. D.; Torre, R.; Bonn, M.; Nagata, Y. Vibrational Spectroscopy and Dynamics of Water. *Chem. Rev.* **2016**, *116* (13), 7590–7607. https://doi.org/10.1021/acs.chemrev.5b00640.

(112) Paesani, F.; Xantheas, S. S.; Voth, G. A. Infrared Spectroscopy and Hydrogen-Bond Dynamics of Liquid Water from Centroid Molecular Dynamics with an Ab Initio-Based Force Field. *J. Phys. Chem. B* **2009**, *113* (39), 13118–13130. https://doi.org/10.1021/jp907648y.

(113) *Propylene carbonate anhydrous, 99.7 108-32-7.* https://www.sigmaaldrich.com/US/en/product/sial/310328?gclid=Cj0KCQiAyracB hDoARIsACGFcS7weCHAT5_OlIWtLy6JvNcz06-j4DeGkq5UR4t4DxbnhJnzKzSJ-YMaAmauEALw_wcB&gclsrc=aw.ds (accessed 2022-12-05).

(114) Baumler, S. M.; V, W. H. H.; Allen, H. C. Hydration of Ferric Chloride and Nitrate in Aqueous Solutions: Water-Mediated Ion Pairing Revealed by Raman Spectroscopy. *Phys. Chem. Chem. Phys.* **2019**, *21* (35), 19172–19180. https://doi.org/10.1039/C9CP01392J.

(115) Berendsen, H. J. C.; Grigera, J. R.; Straatsma, T. P. The Missing Term in Effective Pair Potentials. *J. Phys. Chem.* **1987**, *91* (24), 6269–6271. https://doi.org/10.1021/j100308a038.

(116) Schuler, L. D.; Daura, X.; van Gunsteren, W. F. An Improved GROMOS96 Force Field for Aliphatic Hydrocarbons in the Condensed Phase. *Journal of Computational Chemistry* **2001**, *22* (11), 1205–1218. https://doi.org/10.1002/jcc.1078.

(117) Parrinello, M.; Rahman, A. Polymorphic Transitions in Single Crystals: A New Molecular Dynamics Method. *Journal of Applied Physics* **1981**, *52* (12), 7182–7190. https://doi.org/10.1063/1.328693.

(118) Martyna, G. J.; Tobias, D. J.; Klein, M. L. Constant Pressure Molecular Dynamics Algorithms. *The Journal of Chemical Physics* **1994**, *101* (5), 4177–4189. https://doi.org/10.1063/1.467468.

(119) Andersen, H. C. Rattle: A "Velocity" Version of the Shake Algorithm for Molecular Dynamics Calculations. *Journal of Computational Physics* **1983**, *52* (1), 24–34. https://doi.org/10.1016/0021-9991(83)90014-1.

(120) Eaves, J. D.; Loparo, J. J.; Fecko, C. J.; Roberts, S. T.; Tokmakoff, A.; Geissler, P. L. Hydrogen Bonds in Liquid Water Are Broken Only Fleetingly. *Proceedings of the National Academy of Sciences* **2005**, *102* (37), 13019–13022. https://doi.org/10.1073/pnas.0505125102.

(121) Geissler, P. L. Water Interfaces, Solvation, and Spectroscopy. *Annual Review of Physical Chemistry* **2013**, *64* (1), 317–337. https://doi.org/10.1146/annurev-physchem-040412-110153.

(122) Smith, J. D.; Saykally, R. J.; Geissler, P. L. The Effects of Dissolved Halide Anions on Hydrogen Bonding in Liquid Water. *J. Am. Chem. Soc.* **2007**, *129* (45), 13847–13856. https://doi.org/10.1021/ja071933z.

(123) Hess, B.; van der Vegt, N. F. A. Hydration Thermodynamic Properties of Amino Acid Analogues: A Systematic Comparison of Biomolecular Force Fields and Water Models. *J. Phys. Chem. B* **2006**, *110* (35), 17616–17626. https://doi.org/10.1021/jp0641029.

(124) Tomlinson-Phillips, J.; Davis, J.; Ben-Amotz, D.; Spångberg, D.; Pejov, L.; Hermansson, K. Structure and Dynamics of Water Dangling OH Bonds in Hydrophobic Hydration Shells. Comparison of Simulation and Experiment. *J. Phys. Chem. A* **2011**, *115* (23), 6177–6183. https://doi.org/10.1021/jp111346s.

(125) Stirnemann, G.; Rossky, P. J.; Hynes, J. T.; Laage, D. Water Reorientation, Hydrogen-Bond Dynamics and 2D-IR Spectroscopy next to an Extended Hydrophobic Surface. *Faraday Discuss.* **2010**, *146* (0), 263–281. https://doi.org/10.1039/B925673C.

(126) Perera, P. N.; Fega, K. R.; Lawrence, C.; Sundstrom, E. J.; Tomlinson-Phillips, J.; Ben-Amotz, D. Observation of Water Dangling OH Bonds around Dissolved Nonpolar Groups. *Proceedings of the National Academy of Sciences* **2009**, *106* (30), 12230–12234. https://doi.org/10.1073/pnas.0903675106.

(127) Ma, G.; Chen, X.; Allen, H. C. Dangling OD Confined in a Langmuir Monolayer. *J. Am. Chem. Soc.* **2007**, *129* (45), 14053–14057. https://doi.org/10.1021/ja075806e.

(128) Scatena, L. F.; Brown, M. G.; Richmond, G. L. Water at Hydrophobic Surfaces: Weak Hydrogen Bonding and Strong Orientation Effects. *Science* **2001**, *292* (5518), 908–912.

(129) Medders, G. R.; Paesani, F. Dissecting the Molecular Structure of the Air/Water Interface from Quantum Simulations of the Sum-Frequency Generation Spectrum. *Journal of the American Chemical Society* **2016**, *138* (11), 3912–3919.

(130) Sun, S.; Tang, F.; Imoto, S.; Moberg, D. R.; Ohto, T.; Paesani, F.; Bonn, M.; Backus, E. H.; Nagata, Y. Orientational Distribution of Free OH Groups of Interfacial Water Is Exponential. *Physical review letters* **2018**, *121* (24), 246101.

(131) Zischang, J.; Suhm, M. A. The OH Stretching Spectrum of Warm Water Clusters. *J. Chem. Phys.* **2014**, *140* (6), 064312. https://doi.org/10.1063/1.4865130.

(132) Buck, U.; Pradzynski, C. C.; Zeuch, T.; Dieterich, J. M.; Hartke, B. A Size Resolved Investigation of Large Water Clusters. *Phys. Chem. Chem. Phys.* **2014**, *16* (15), 6859–6871. https://doi.org/10.1039/C3CP55185G.

(133) Senanayake, H. S.; Greathouse, J. A.; Ilgen, A. G.; Thompson, W. H. Simulations of the IR and Raman Spectra of Water Confined in Amorphous Silica Slit Pores. *J. Chem. Phys.* **2021**, *154* (10), 104503. https://doi.org/10.1063/5.0040739.

(134) Morawietz, T.; Marsalek, O.; Pattenaude, S. R.; Streacker, L. M.; Ben-Amotz, D.; Markland, T. E. The Interplay of Structure and Dynamics in the Raman Spectrum of Liquid Water over the Full Frequency and Temperature Range. *J. Phys. Chem. Lett.* **2018**, *9* (4), 851–857. https://doi.org/10.1021/acs.jpclett.8b00133.

(135) Luzar, A.; Chandler, D. Effect of Environment on Hydrogen Bond Dynamics in Liquid Water. *Phys Rev Lett* **1996**, *76* (6), 928–931. https://doi.org/10.1103/PhysRevLett.76.928.

(136) Fecko, C. J.; Eaves, J. D.; Loparo, J. J.; Tokmakoff, A.; Geissler, P. L. Ultrafast Hydrogen-Bond Dynamics in the Infrared Spectroscopy of Water. *Science* **2003**, *301* (5640), 1698–1702. https://doi.org/10.1126/science.1087251.

(137) Asbury, J. B.; Steinel, T.; Stromberg, C.; Corcelli, S. A.; Lawrence, C. P.; Skinner, J. L.; Fayer, M. D. Water Dynamics: Vibrational Echo Correlation Spectroscopy and Comparison to Molecular Dynamics Simulations. *J. Phys. Chem. A* **2004**, *108* (7), 1107–1119. https://doi.org/10.1021/jp036266k.

(138) Corcelli, S. A.; Lawrence, C. P.; Skinner, J. L. Combined Electronic Structure/Molecular Dynamics Approach for Ultrafast Infrared Spectroscopy of Dilute HOD in Liquid H_2O and D_2O. *The Journal of Chemical Physics* **2004**, *120* (17), 8107–8117. https://doi.org/10.1063/1.1683072.

(139) Janz, G. J.; Ambrose, J.; Coutts, J. W.; Downey, J. R. Raman Spectrum of Propylene Carbonate. *Spectrochimica Acta Part A: Molecular Spectroscopy* **1979**, *35* (2), 175–179. https://doi.org/10.1016/0584-8539(79)80181-6.

(140) Dreier, L. B.; Bonn, M.; Backus, E. H. G. Hydration and Orientation of Carbonyl Groups in Oppositely Charged Lipid Monolayers on Water. *J Phys Chem B* **2019**, *123* (5), 1085–1089. https://doi.org/10.1021/acs.jpcb.8b12297.

(141) Edington, S. C.; Flanagan, J. C.; Baiz, C. R. An Empirical IR Frequency Map for Ester C═O Stretching Vibrations. *J. Phys. Chem. A* **2016**, *120* (22), 3888–3896. https://doi.org/10.1021/acs.jpca.6b02887.

(142) Giorgini, M. G.; Torii, H.; Musso, M.; Venditti, G. Influence of Ions on the Structural Organization of Dipolar Liquids Probed by the Noncoincidence Effect: Experimental and Quantum Chemical Results. *J. Phys. Chem. B* **2008**, *112* (25), 7506–7514. https://doi.org/10.1021/jp800252n.

(143) Vazquez de Vasquez, M. G.; Wellen Rudd, B. A.; Baer, M. D.; Beasley, E. E.; Allen, H. C. Role of Hydration in Magnesium versus Calcium Ion Pairing with Carboxylate: Solution and the Aqueous Interface. *J. Phys. Chem. B* **2021**, *125* (40), 11308–11319. https://doi.org/10.1021/acs.jpcb.1c06108.

(144) Brodin, A.; Jacobsson, P. Dipolar Interaction and Molecular Ordering in Liquid Propylene Carbonate: Anomalous Dielectric Susceptibility and Raman Non-Coincidence Effect. *Journal of Molecular Liquids* **2011**, *164* (1), 17–21. https://doi.org/10.1016/j.molliq.2011.08.001.

(145) Ladanyi, B. M.; Geiger, L. C.; Zerda, T. W.; Song, X.; Jonas, J. Experimental and Molecular Dynamics Study of the Pressure Dependence of Raman Spectra of Oxygen. *The Journal of Chemical Physics* **1988**, *89* (2), 660–672. https://doi.org/10.1063/1.455241.

(146) Giorgini, M. G.; Torii, H.; Musso, M. The Influence of Alkaline Earth Ions on the Structural Organization of Acetone Probed by the Noncoincidence Effect of the ν(CO) Band: Experimental and Quantum Chemical Results. *Phys. Chem. Chem. Phys.* **2009**, *12* (1), 183–192. https://doi.org/10.1039/B912164A.

(147) Chatfield, R. B. Anomalous HNO3/NOx Ratio of Remote Tropospheric Air: Conversion of Nitric Acid to Formic Acid and NOx? *Geophysical Research Letters* **1994**, *21* (24), 2705–2708. https://doi.org/10.1029/94GL02659.

(148) Underwood, G. M.; Miller, T. M.; Grassian, V. H. Transmission FT-IR and Knudsen Cell Study of the Heterogeneous Reactivity of Gaseous Nitrogen Dioxide on Mineral Oxide Particles. *J. Phys. Chem. A* **1999**, *103* (31), 6184–6190. https://doi.org/10.1021/jp991586i.

(149) Stemmler, K.; Ndour, M.; Elshorbany, Y.; Kleffmann, J.; D'Anna, B.; George, C.; Bohn, B.; Ammann, M. Light Induced Conversion of Nitrogen Dioxide into Nitrous Acid on Submicron Humic Acid Aerosol. *Atmospheric Chemistry and Physics* **2007**, *7* (16), 4237–4248. https://doi.org/10.5194/acp-7-4237-2007.

(150) Kolb, C. E.; Cox, R. A.; Abbatt, J. P. D.; Ammann, M.; Davis, E. J.; Donaldson, D. J.; Garrett, B. C.; George, C.; Griffiths, P. T.; Hanson, D. R.; Kulmala, M.; McFiggans, G.; Pöschl, U.; Riipinen, I.; Rossi, M. J.; Rudich, Y.; Wagner, P. E.; Winkler, P. M.; Worsnop, D. R.; O' Dowd, C. D. An Overview of Current Issues in the Uptake of Atmospheric Trace Gases by Aerosols and Clouds. *Atmospheric Chemistry and Physics* **2010**, *10* (21), 10561–10605. https://doi.org/10.5194/acp-10-10561-2010.

(151) Li, L.; Hoffmann, M. R.; Colussi, A. J. Role of Nitrogen Dioxide in the Production of Sulfate during Chinese Haze-Aerosol Episodes. *Environ. Sci. Technol.* **2018**, *52* (5), 2686–2693. https://doi.org/10.1021/acs.est.7b05222.

(152) Phillips, L. F. Atmospheric Reactions on Electrically Charged Surfaces. *Phys. Chem. Chem. Phys.* **2013**, *15* (26), 10749–10752. https://doi.org/10.1039/C3CP51171E.

(153) Rubasinghege, G.; H. Grassian, V. Role(s) of Adsorbed Water in the Surface Chemistry of Environmental Interfaces. *Chemical Communications* **2013**, *49* (30), 3071–3094. https://doi.org/10.1039/C3CC38872G.

(154) Deming, B. L.; Ziemann, P. J. Measurements of the Partitioning of Nitric Acid and Sulfuric Acid in Aqueous/Organic Phase-Separated Systems. *Environ. Sci.: Atmos.* **2021**, *1* (2), 93–103. https://doi.org/10.1039/D0EA00003E.

(155) Shrivastava, M.; Cappa, C. D.; Fan, J.; Goldstein, A. H.; Guenther, A. B.; Jimenez, J. L.; Kuang, C.; Laskin, A.; Martin, S. T.; Ng, N. L.; Petaja, T.; Pierce, J. R.; Rasch,

P. J.; Roldin, P.; Seinfeld, J. H.; Shilling, J.; Smith, J. N.; Thornton, J. A.; Volkamer, R.; Wang, J.; Worsnop, D. R.; Zaveri, R. A.; Zelenyuk, A.; Zhang, Q. Recent Advances in Understanding Secondary Organic Aerosol: Implications for Global Climate Forcing. *Reviews of Geophysics* **2017**, *55* (2), 509–559. https://doi.org/10.1002/2016RG000540.

(156) Hamra, G. B.; Laden, F.; Cohen, A. J.; Raaschou-Nielsen, O.; Brauer, M.; Loomis, D. Lung Cancer and Exposure to Nitrogen Dioxide and Traffic: A Systematic Review and Meta-Analysis. *Environmental Health Perspectives* **2015**, *123* (11), 1107–1112. https://doi.org/10.1289/ehp.1408882.

(157) Favarato, G.; Anderson, H. R.; Atkinson, R.; Fuller, G.; Mills, I.; Walton, H. Traffic-Related Pollution and Asthma Prevalence in Children. Quantification of Associations with Nitrogen Dioxide. *Air Qual Atmos Health* **2014**, *7* (4), 459–466. https://doi.org/10.1007/s11869-014-0265-8.

(158) Larkin, A.; Geddes, J. A.; Martin, R. V.; Xiao, Q.; Liu, Y.; Marshall, J. D.; Brauer, M.; Hystad, P. Global Land Use Regression Model for Nitrogen Dioxide Air Pollution. *Environ. Sci. Technol.* **2017**, *51* (12), 6957–6964. https://doi.org/10.1021/acs.est.7b01148.

(159) Brook, R. D.; Rajagopalan, S.; Pope, C. A.; Brook, J. R.; Bhatnagar, A.; Diez-Roux, A. V.; Holguin, F.; Hong, Y.; Luepker, R. V.; Mittleman, M. A.; Peters, A.; Siscovick, D.; Smith, S. C.; Whitsel, L.; Kaufman, J. D. Particulate Matter Air Pollution and Cardiovascular Disease. *Circulation* **2010**, *121* (21), 2331–2378. https://doi.org/10.1161/CIR.0b013e3181dbece1.

(160) Goupil, J.-M.; Hemidy, J.-F.; Cornet, D. Adsorption of NO2 on Modified Y Zeolites. *Zeolites* **1982**, *2* (1), 47–50. https://doi.org/10.1016/S0144-2449(82)80040-7.

(161) Triebe, R. W.; Tezel, F. H. Adsorption of Nitrogen, Carbon Monoxide, Carbon Dioxide and Nitric Oxide on Molecular Sieves. *Gas Separation & Purification* **1995**, *9* (4), 223–230. https://doi.org/10.1016/0950-4214(95)00017-6.

(162) Pietrzak, R. Sawdust Pellets from Coniferous Species as Adsorbents for NO2 Removal. *Bioresource Technology* **2010**, *101* (3), 907–913. https://doi.org/10.1016/j.biortech.2009.09.017.

(163) Nowicki, P.; Pietrzak, R. Carbonaceous Adsorbents Prepared by Physical Activation of Pine Sawdust and Their Application for Removal of NO2 in Dry and Wet Conditions. *Bioresource Technology* **2010**, *101* (15), 5802–5807. https://doi.org/10.1016/j.biortech.2010.02.098.

(164) Jeguirim, M.; Belhachemi, M.; Limousy, L.; Bennici, S. Adsorption/Reduction of Nitrogen Dioxide on Activated Carbons: Textural Properties versus Surface Chemistry – A Review. *Chemical Engineering Journal* **2018**, *347*, 493–504. https://doi.org/10.1016/j.cej.2018.04.063.

(165) Belhachemi, M.; Jeguirim, M.; Limousy, L.; Addoun, F. Comparison of NO2 Removal Using Date Pits Activated Carbon and Modified Commercialized Activated Carbon via Different Preparation Methods: Effect of Porosity and Surface Chemistry. *Chemical Engineering Journal* **2014**, *253*, 121–129. https://doi.org/10.1016/j.cej.2014.05.004.

(166) Levasseur, B.; Ebrahim, A. M.; Bandosz, T. J. Interactions of NO2 with Amine-Functionalized SBA-15: Effects of Synthesis Route. *Langmuir* **2012**, *28* (13), 5703–5714. https://doi.org/10.1021/la300371m.

(167) Han, X.; Godfrey, H. G. W.; Briggs, L.; Davies, A. J.; Cheng, Y.; Daemen, L. L.; Sheveleva, A. M.; Tuna, F.; McInnes, E. J. L.; Sun, J.; Drathen, C.; George, M. W.; Ramirez-Cuesta, A. J.; Thomas, K. M.; Yang, S.; Schröder, M. Reversible Adsorption of Nitrogen Dioxide within a Robust Porous Metal–Organic Framework. *Nature Mater* **2018**, *17* (8), 691–696. https://doi.org/10.1038/s41563-018-0104-7.

(168) Ding, Q.; Zhou, Z.; Wang, H.; Wu, Z.; Tao, K.; Yang, B.-R.; Xie, X.; Fu, J.; Wu, J. Self-Healable, Recyclable, Ultrastretchable, and High-Performance NO2 Sensors Based on an Organohydrogel for Room and Sub-Zero Temperature and Wireless Operation. *SmartMat* **2023**, *4* (1), e1141. https://doi.org/10.1002/smm2.1141.

(169) Li, X.; Shi, W.; Yu, X.; Yu, J. Performance Improvement of Organic Field-Effect Transistor Based Nitrogen Dioxide Gas Sensor Using Biocompatible PMMA/Silk Fibroin Bilayer Dielectric. *J Mater Sci: Mater Electron* **2015**, *26* (10), 7948–7954. https://doi.org/10.1007/s10854-015-3448-7.

(170) Kondo, K.; Sano, M.; Hiwara, A.; Omi, T.; Fujita, M.; Kuwae, A.; Iida, M.; Mogi, K.; Yokoyama, H. Conductivity and Solvation of Li+ Ions of LiPF6 in Propylene Carbonate Solutions. *J. Phys. Chem. B* **2000**, *104* (20), 5040–5044. https://doi.org/10.1021/jp000142f.

(171) Barnes, I.; Wiesen, P.; Gallus, M. Kinetics and Mechanism of the OH-Radical and Cl-Atom Oxidation of Propylene Carbonate. *RSC Advances* **2016**, *6* (100), 98234–98242. https://doi.org/10.1039/C6RA21952G.

(172) PubChem. *Propylene Carbonate*. https://pubchem.ncbi.nlm.nih.gov/compound/7924.

(173) Mai, T. V.-T.; Nguyen, H. T.; Huynh, L. K. Atmospheric Chemistry of the Reaction between Propylene Carbonate and OH Radical: An *Ab Initio* RRKM-Based Master Equation Study. *Chemical Physics Letters* **2020**, *739*, 137020. https://doi.org/10.1016/j.cplett.2019.137020.

(174) Wängberg, I.; Etzkorn, T.; Barnes, I.; Platt, U.; Becker, K. H. Absolute Determination of the Temperature Behavior of the NO2 + NO3 +(M) ↔ N2O5 + (M) Equilibrium. *J. Phys. Chem. A* **1997**, *101* (50), 9694–9698. https://doi.org/10.1021/jp972203o.

(175) King, M. D.; Rennie, A. R.; Pfrang, C.; Hughes, A. V.; Thompson, K. C. Interaction of Nitrogen Dioxide (NO2) with a Monolayer of Oleic Acid at the Air–Water Interface – A Simple Proxy for Atmospheric Aerosol. *Atmospheric Environment* **2010**, *44* (14), 1822–1825. https://doi.org/10.1016/j.atmosenv.2010.01.031.

(176) Murdachaew, G.; Varner, M. E.; van der Veer, W. E.; Gerber, R. B.; Phillips, L. F. Raman Spectroscopy of Solutions and Interfaces Containing Nitrogen Dioxide, Water, and 1,4 Dioxane: Evidence for Repulsion of Surface Water by NO2 Gas. *The Journal of Chemical Physics* **2014**, *140* (18), 184702. https://doi.org/10.1063/1.4874640.

(177) Lewis, R. N.; McElhaney, R. N.; Pohle, W.; Mantsch, H. H. Components of the Carbonyl Stretching Band in the Infrared Spectra of Hydrated 1,2-

Diacylglycerolipid Bilayers: A Reevaluation. *Biophysical Journal* **1994**, *67* (6), 2367–2375. https://doi.org/10.1016/S0006-3495(94)80723-4.

(178) Blume, A.; Huebner, W.; Messner, G. Fourier Transform Infrared Spectroscopy of 13C:O Labeled Phospholipids Hydrogen Bonding to Carbonyl Groups. *Biochemistry* **1988**, *27* (21), 8239–8249. https://doi.org/10.1021/bi00421a038.

(179) Yeager, H. L.; Fedyk, J. D.; Parker, R. J. Spectroscopic Studies of Ionic Solvation in Propylene Carbonate. *J. Phys. Chem.* **1973**, *77* (20), 2407–2410. https://doi.org/10.1021/j100639a008.

(180) Brooksby, P. A.; Fawcett, W. R. Infrared (Attenuated Total Reflection) Study of Propylene Carbonate Solutions Containing Lithium and Sodium Perchlorate. *Spectrochimica Acta Part A: Molecular and Biomolecular Spectroscopy* **2006**, *64* (2), 372–382. https://doi.org/10.1016/j.saa.2005.07.033.

(181) Xiao, S.; Bertram, A. K. Reactive Uptake Kinetics of NO3 on Multicomponent and Multiphase Organic Mixtures Containing Unsaturated and Saturated Organics. *Phys. Chem. Chem. Phys.* **2011**, *13* (14), 6628–6636. https://doi.org/10.1039/C0CP02682D.

(182) Clark, J. B.; Bowling-Charles, T.; Jabeen Proma, S.; Biswas, B.; Limmer, D. T.; Allen, H. C. Structural Evolution of Water-in-Propylene Carbonate Mixtures Revealed by Polarized Raman Spectroscopy and Molecular Dynamics. *Physical Chemistry Chemical Physics* **2023**, *25* (35), 23963–23976. https://doi.org/10.1039/D3CP02181E.

(183) Badger, C. L.; Griffiths, P. T.; George, I.; Abbatt, J. P. D.; Cox, R. A. Reactive Uptake of N2O5 by Aerosol Particles Containing Mixtures of Humic Acid and Ammonium Sulfate. *J. Phys. Chem. A* **2006**, *110* (21), 6986–6994. https://doi.org/10.1021/jp0562678.

(184) George, C.; Ponche, J. L.; Mirabel, P.; Behnke, W.; Scheer, V.; Zetzsch, C. Study of the Uptake of N2O5 by Water and NaCl Solutions. *J. Phys. Chem.* **1994**, *98* (35), 8780–8784. https://doi.org/10.1021/j100086a031.

(185) Ryder, O. S.; Campbell, N. R.; Morris, H.; Forestieri, S.; Ruppel, M. J.; Cappa, C.; Tivanski, A.; Prather, K.; Bertram, T. H. Role of Organic Coatings in Regulating N2O5 Reactive Uptake to Sea Spray Aerosol. *J. Phys. Chem. A* **2015**, *119* (48), 11683–11692. https://doi.org/10.1021/acs.jpca.5b08892.

(186) Ryder, O. S.; Ault, A. P.; Cahill, J. F.; Guasco, T. L.; Riedel, T. P.; Cuadra-Rodriguez, L. A.; Gaston, C. J.; Fitzgerald, E.; Lee, C.; Prather, K. A.; Bertram, T. H. On the Role of Particle Inorganic Mixing State in the Reactive Uptake of N2O5 to Ambient Aerosol Particles. *Environ. Sci. Technol.* **2014**, *48* (3), 1618–1627. https://doi.org/10.1021/es4042622.

(187) Dao, A. K. Probing N2O5 Reactive Uptake in Organic Solvents Using a Flow Reactor and Chemical Ionization Mass Spectrometry, University of Wisconsin-Madison, 2020.

(188) Kregel, S. J.; Derrah, T. F.; Moon, S.; Limmer, D. T.; Nathanson, G. M.; Bertram, T. H. Weak Temperature Dependence of the Relative Rates of Chlorination and Hydrolysis of N2O5 in NaCl–Water Solutions. *J. Phys. Chem. A* **2023**, *127* (7), 1675–1685. https://doi.org/10.1021/acs.jpca.2c06543.

(189) Finlayson-Pitts, B. J.; Livingston, F. E.; Berko, H. N. Synthesis and Identification by Infrared Spectroscopy of Gaseous Nitryl Bromide, BrNO2. *J. Phys. Chem.* **1989**, *93* (11), 4397–4400. https://doi.org/10.1021/j100348a005.

(190) Feierabend, K. J.; Havey, D. K.; Vaida, V. Gas Phase Spectroscopy of HNO3 in the Region 2000–8500cm−1. *Spectrochimica Acta Part A: Molecular and Biomolecular Spectroscopy* **2004**, *60* (12), 2775–2781. https://doi.org/10.1016/j.saa.2004.01.016.

(191) Lovejoy, R. W.; Chackerian, C.; Boese, R. W. Integrated Band Intensities of Gaseous N2O5. *Appl. Opt., AO* **1980**, *19* (5), 744–748. https://doi.org/10.1364/AO.19.000744.

(192) Hisatsune, I. C.; Devlin, J. P.; Wada, Y. Vibrational Spectrum and Structure of N2O5. *Spectrochimica Acta* **1962**, *18* (12), 1641–1653. https://doi.org/10.1016/0371-1951(62)80028-9.

(193) Perrin, A. Recent Progress in the Analysis of HNO3 Spectra. *Spectrochimica Acta Part A: Molecular and Biomolecular Spectroscopy* **1998**, *54* (3), 375–393. https://doi.org/10.1016/S1386-1425(97)00257-6.

Appendix A. Supplemental Information for Chapter 3

A.1 Spectral Preprocessing

To account for small baseline shifts that occurred between replicates, the Raman spectra were aligned to a common baseline by taking the average of the final 50 intensity values ($3750–3850$ cm^{-1}) in each spectrum where there are no spectral features. The average value was then subtracted from the intensity of the corresponding spectrum. Following this baseline alignment, the average of the replicates was acquired. The O-H stretching region of the Raman spectra following the baseline adjustment and averaging of replicates is depicted in Figure 31.
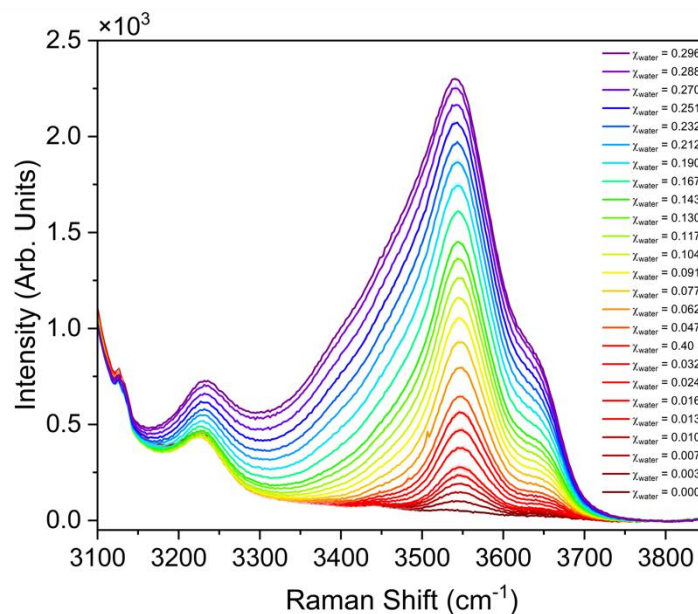
Figure 31. Raman spectra in the O-H stretching region for propylene carbonate with increasing water concentrations (red $\chi_{water} = 0$ to violet $\chi_{water} = 0.296$). Spectra are plotted as the average of two replicates following baseline adjustment and the standard deviation is plotted as shading.

Due to overlap with the intense C-H stretching modes that originate from PC, the O-H stretching region has a steeply sloped baseline and is convoluted with the C-H stretching mode from PC at 3220 cm^{-1}. To deconvolute the spectral contributions of water and propylene carbonate in the O-H stretching region, an intensity normalization and subtraction of the pure propylene carbonate spectrum is performed. For the intensity normalization, a scaling factor, f, is calculated for each of the water concentrations studied. This is accomplished by dividing the intensity of the symmetric CH$_2$ stretching peak (2938 cm^{-1}) in the specific water + PC spectrum by the intensity (at the same peak position) in the pure PC spectrum. The entire pure PC spectrum was then scaled by the resulting ratio and subtracted from the corresponding water + PC spectrum. This process is carried out mathematically for $\chi_{water} = 0.296$ as follows:

Equation 46

$$f = \left(\frac{I_{\chi=0.296}(2938\ cm^{-1})}{I_{\chi=0}(2938\ cm^{-1})} \right)$$

Equation 47

$$Corrected\ Spectrum = I_{\chi=0.296} - \left(f \cdot I_{\chi=0} \right)$$

Figure 32 demonstrates the result of scaling the pure PC spectrum to the intensity of the $\chi_{water} = 0.296$ spectrum as well as the resulting difference ("corrected") spectrum.
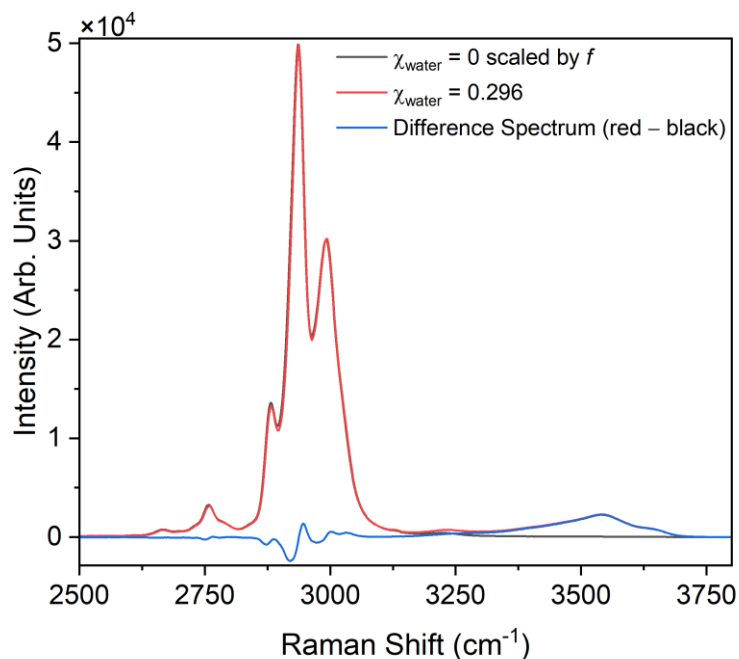
Figure 32. Raman Spectrum of PC + χ_{water} = 0.296 (red), Pure PC (χ_{water} = 0) scaled by the calculated scaling factor, f (black), and the resulting spectrum obtained from their subtraction (blue). Subtraction carried out to remove spectral contributions of pure PC from the O-H stretching region.

The symmetric CH_2 stretching peak was chosen as the reference point because it is the most intense peak in each of the individual spectra and because the scaling factor obtained using this peak is approximately the average scaling factor obtained when the same process was carried out using the symmetric CH_3 and asymmetric CH_2 stretching peaks as the reference point. After the intensity normalization and subtraction procedure, the spectral contributions from pure PC in the O-H stretching region have been removed. The resulting O-H stretching bands originating from water are plotted in Chapter 3.

A.2 Raman Gaussian Deconvolution

To characterize the hydrogen bond structure of water as a function of its concentration in PC, the O-H stretching region was fit using a Gaussian deconvolution procedure in Origin Pro 2023. The deconvolution was carried out for 12 of the 25 total

spectra, which includes the mole fractions χ_{water} = 0.007, 0.013, 0.024, 0.040, 0.062, 0.091, 0.117, 0.143, 0.190, 0.232, 0.270, and 0.296. The Fit Peaks (Pro) function in Origin Lab was used to parametrize and carry out the Gaussian fitting for the O-H stretching region between 3073 and 3847 cm^{-1} in each of the 12 spectra. The first step in the parametrization process is defining a baseline for the curve by choosing anchor points along the baseline and an appropriate function to connect the anchor points, effectively fitting the baseline of the data. The wavenumber values 3077, 3096, 3814, and 3843 cm^{-1} were chosen as anchor points for all spectra that were fit. These anchor points were then connected by a linear function. Following this, initial values for the Gaussian peak positions were chosen based on Origin Lab's built-in peak-finding function. Once the initialization parameters were set, the Gaussian fitting was carried out until a chi-squared convergence tolerance of 1×10^{-6} was reached. All parameters of the fit were allowed to vary freely apart from the baseline and the peak position of the highest frequency Gaussian. The decision to set the position of the highest frequency Gaussian to a constant value was made after the χ_{water} = 0.143, 0.190, 0.232, 0.270, and 0.296 spectra were initially fit without fixing this parameter. In these fits, the peak position of this Gaussian remained approximately constant, only changing by $\pm$ 0.2 cm^{-1}, which is much smaller that the resolution of the Raman instrument. Therefore, the position of this band was set as a fixed parameter for all subsequent fittings. The fit result of the highest water concentration spectrum was used to determine the constant value of the peak position to be 3642.85 cm^{-1}. The lowest frequency band in the O-H stretching region did not have a high enough intensity to carry out the fitting (did not converge within 500 iterations) until the concentration χ_{water} = 0.091 was reached, therefore

113

only the seven highest concentration spectra were able to be fit to four total bands. The lower water concentration spectra are only fit to three bands. In Figure 33, the O-H stretching region of the Raman spectra are plotted with the fit result overlaid on the corresponding spectrum. Table 2 contains the converged parameters for all deconvoluted spectra.
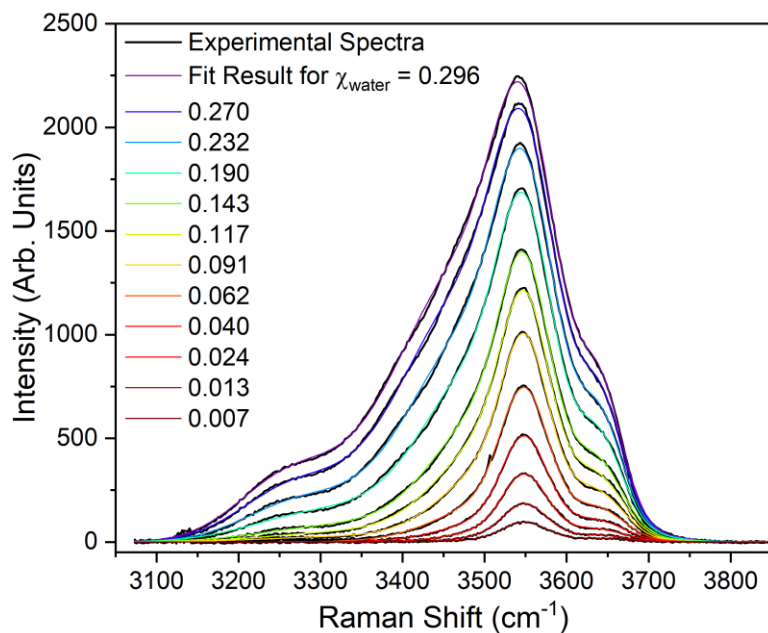
Figure 33. Result of Gaussian fitting to the O-H stretching Raman spectra of PC as a function of increasing water concentration. Experimental spectra are plotted in black and calculated (fit) results are in color.

χ_{water}	Center (cm^{-1})	Area	Max. Intensity	FWHM

Table 2. Peak center (cm^{-1}), area, intensity (arb. units), and full-width-half-max (FWHM) values obtained from the Gaussian fits of the O-H stretching region in the Raman spectra of PC/water.

χ_{water}	Center (cm^{-1})	Area	Max. Intensity	FWHM
Peak 1				
0.091	3331.549	5871.516	24.767	222.712
0.117	3329.720	10168.207	45.819	208.482
0.143	3313.961	15339.471	72.718	198.169
0.190	3292.773	25583.312	132.021	182.046
0.232	3274.531	30960.326	184.085	158.000
0.270	3266.546	40439.966	248.489	152.887
0.296	3261.367	46670.106	295.524	148.359
Peak 2				
0.007	3548.494	2272.982	12.437	171.694
0.013	3543.662	5779.104	42.771	126.935
0.024	3540.814	12003.970	77.994	144.588
0.040	3537.119	23089.416	132.327	163.920
0.062	3528.579	40341.990	219.315	172.805
0.091	3526.457	68049.167	397.876	160.673
0.117	3523.554	96854.100	541.741	167.956
0.143	3520.025	128609.003	681.587	177.263
0.190	3509.432	182358.176	899.519	190.451
0.232	3495.311	223349.016	1042.904	201.190
0.270	3485.685	266098.194	1207.844	206.966
0.296	3480.473	299576.228	1326.595	212.147
Peak 3				
0.007	3548.535	5596.160	83.026	63.320
0.013	3549.036	9158.259	141.291	60.893
0.024	3548.803	16421.794	250.442	61.600
0.040	3548.677	25529.054	380.962	62.954
0.062	3548.473	37362.355	534.077	65.720
0.091	3548.915	42541.617	624.894	63.955
0.117	3548.901	48777.053	700.712	65.395
0.143	3548.627	54480.111	758.554	67.471
0.190	3549.084	68665.483	878.296	73.446
0.232	3549.617	89078.920	1024.946	81.647
0.270	3550.014	105598.410	1134.446	87.446
0.296	3550.152	115507.264	1194.283	90.859
Peak 4				
0.007	3642.851	869.162	11.494	71.036
0.013	3642.851	2051.773	25.740	74.885
0.024	3642.851	3372.969	42.166	75.148
0.040	3642.851	4657.074	61.421	71.230
0.062	3642.851	7091.936	98.528	67.620
0.091	3642.851	11228.184	149.198	70.699
0.117	3642.851	13517.129	185.393	68.495
0.143	3642.851	14812.833	214.231	64.957
0.190	3642.851	19628.678	295.670	62.366
0.232	3642.851	25542.695	386.414	62.099
0.270	3642.851	30208.874	458.577	61.886
0.296	3642.851	32249.766	492.302	61.541

To aid in the assignment of the deconvoluted O-H stretching bands, isotopic dilution spectra (10% HOD in D_2O) were deconvoluted in the same manner of the H_2O spectra. The HOD spectrum for the highest D_2O concentration is plotted in Figure 34 along with the deconvoluted Gaussian bands. Table 3 contains the converged parameters for the deconvoluted $\chi_{water} = 0.23$ spectrum.
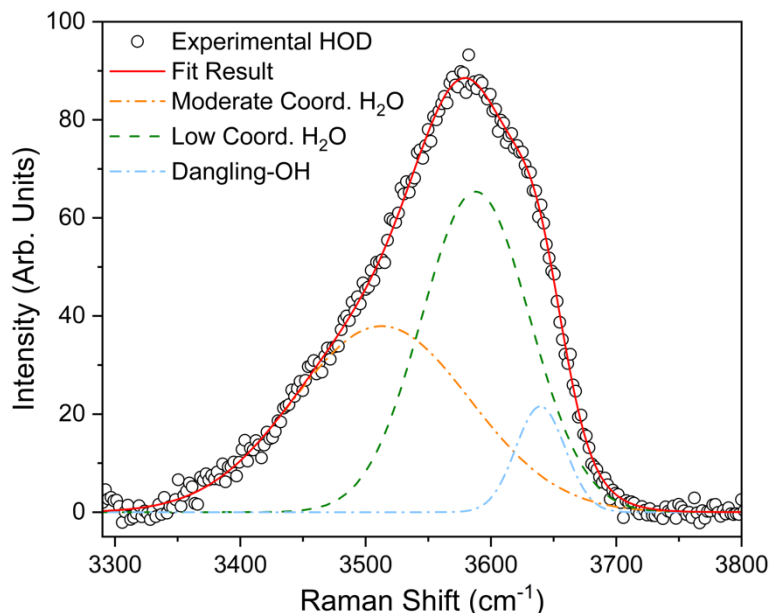
Figure 34. Gaussian deconvolution results for the isotopic dilution experiment where $\chi_{water} = 0.23$. Experimental data is plotted in black circles and the fit plotted as a red solid line. Dashed lines represent Gaussian bands used to fit experimental spectra.

Table 3. Peak center (cm^{-1}), area, intensity (arb. units), and full-width-half-max (FWHM) values obtained from the Gaussian fitting of the O-H stretching region in the Raman spectra of the isotopically diluted PC/D_2O mixtures.				
Peak	**Center (cm^{-1})**	**Area**	**Max. Intensity**	**FWHM**
2	3512.755	6689.334	37.935	165.656
3	3587.795	7074.990	65.350	101.707
4	3639.476	1066.919	21.581	46.443

A.3 Attenuated Total Reflectance (ATR)-FTIR Spectra

ATR-FTIR spectra were taken to complement the Raman spectra of dilute water in PC. The ATR-FTIR spectra of the O-H stretching region for a selection of concentrations matching those in the Raman spectra are plotted in Figure 35. The χ_{water} = 0.013 and 0.223 spectra were deconvoluted in the same manner as the Raman spectra. The results are plotted in Figure 36 to demonstrate the evolution of the deconvoluted bands with water concentration. Table 4 contains the converged parameters for the deconvoluted χ_{water} = 0.013 and 0.223 ATR-FTIR spectra.
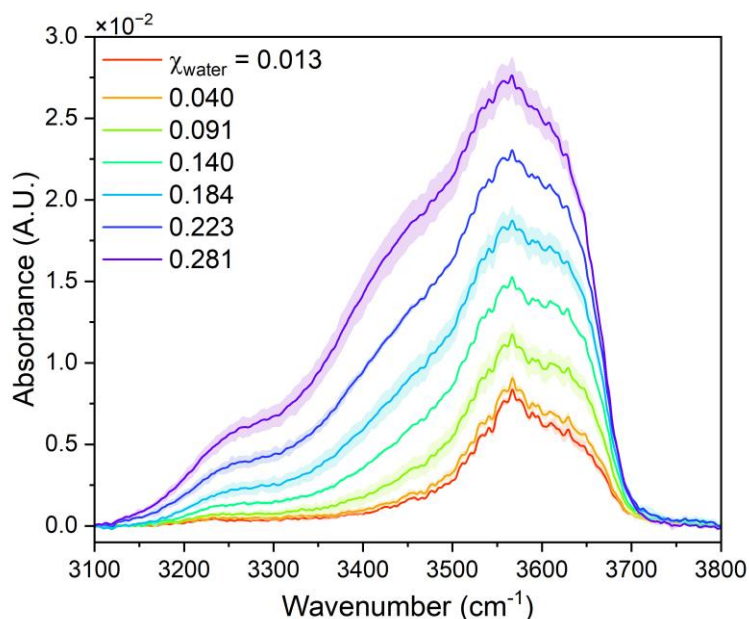
Figure 35. O-H stretching region in the ATR-FTIR spectra of increasing concentrations of water in PC. The spectra are an average of two trials and the standard deviation is included as shading around the solid line.
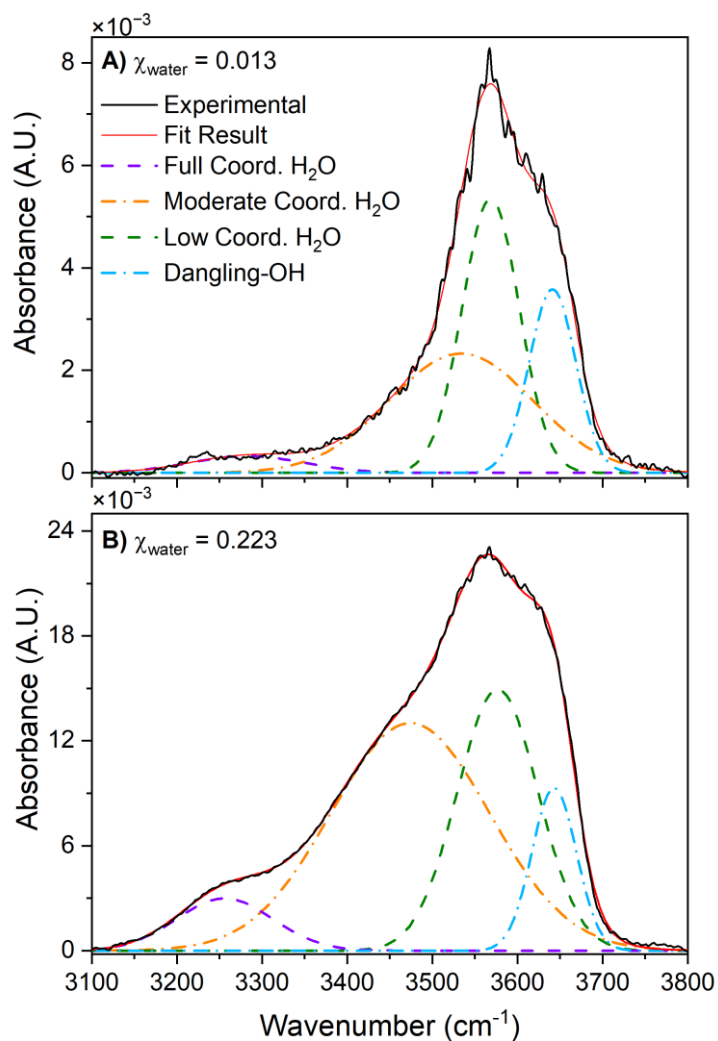
Figure 36. Gaussian deconvolution of experimental ATR-FTIR O-H region for water concentrations χ_{water} = 0.013 (A) and 0.223 (B). Experimental (black) and fit (red) spectra are plotted with solid lines. Dashed lines represent Gaussian bands used to fit experimental spectra.

Table 4. Peak center (cm⁻¹), area, intensity (arb. units), and full-width-half-max (FWHM) values obtained from the Gaussian fits of the O-H stretching region in the ATR-FTIR spectra of the PC/water mixtures.

χ_{water}	Center (cm^{-1})	Area	Max. Intensity	FWHM
Peak 1				
0.013	3282.312	0.055	0.0003	156.755
0.223	3256.119	0.426	0.003	133.945
Peak 2				
0.013	3533.883	0.493	0.002	198.987
0.223	3474.114	3.033	0.013	218.946
Peak 3				
0.013	3568.560	0.449	0.005	78.881
0.223	3576.849	1.785	0.015	112.215
Peak 4				
0.013	3641.142	0.246	0.004	64.631
0.223	3643.126	0.609	0.009	61.600

A.4 Raman Ester Band Analysis

The symmetric and asymmetric ester group stretching bands from PC are reported to occur at 959 and 1228 cm⁻¹, respectively in Raman spectra.[139] Here, we observe these bands at 952.79 and 1224.31 cm⁻¹ in the VV polarized Raman spectrum of pure PC. These bands are analyzed in order to determine bulk PC structure as a function of water concentration. The Raman spectra showing the ester bands for the $\chi_{water} = 0$ (pure PC) and $\chi_{water} = 0.296$ solutions are plotted in Figure 37. Both the VV and VH polarized responses are included for determination of the non-coincidence effect (NCE). The NCEs for the symmetric ester band when $\chi_{water} = 0$ and 0.296 are 0.39 and 0.32 cm⁻¹, respectively. The NCEs for the asymmetric ester band when $\chi_{water} = 0$ and 0.296 are -0.31 and -0.32 cm⁻¹, respectively. Peak positions for the symmetric and asymmetric polarized bands were determined through Gaussian fitting and the results are included in Table 5.
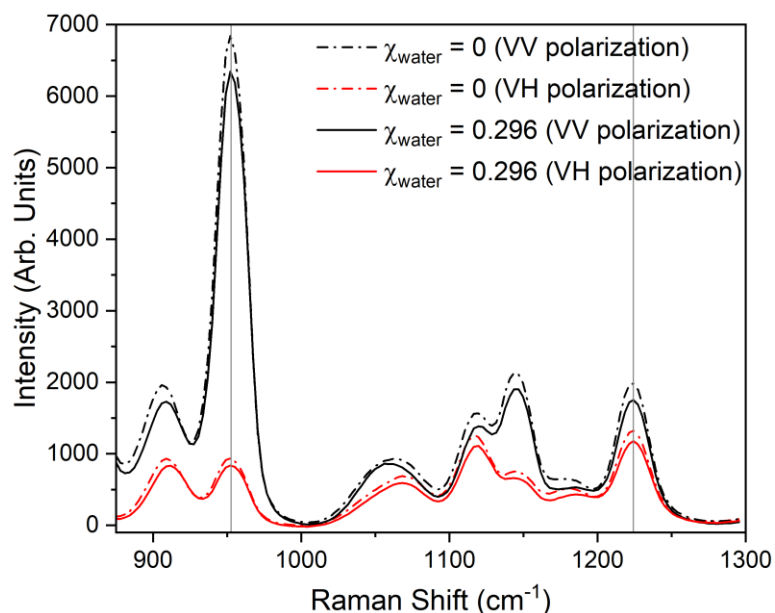
Figure 37. Raman spectra of the symmetric and asymmetric ester stretching bands of PC for the $\chi_{water} = 0$ (dashed lines) and $\chi_{water} = 0.296$ solutions (solid lines). The VV (black) and VH (red) polarized spectra are both included. Gray reference lines are plotted at the peak positions of the symmetric (952.8 cm^{-1}) and asymmetric (1224.3 cm^{-1}) VV polarized ester bands in the $\chi_{water} = 0$ spectrum.

Spectrum	Center (cm^{-1})	Area	Max. Intensity	FWHM
Table 5. Peak center (cm^{-1}), area, intensity (arb. units), and full-width-half-max (FWHM) values obtained from the Gaussian fitting of the ester stretching bands in the Raman spectra of the PC/water mixtures.				
Symmetric Ester Band				
$\chi_{water} = 0$ (VV pol.)	952.791	163119.432	6611.649	23.177
$\chi_{water} = 0$ (VH pol.)	952.404	24148.932	890.051	25.489
$\chi_{water} = 0.296$ (VV pol.)	953.288	152857.135	6161.320	23.307
$\chi_{water} = 0.296$ (VH pol.)	952.971	22265.168	818.978	25.540
Asymmetric Ester Band				
$\chi_{water} = 0$ (VV pol.)	1224.306	41129.143	1673.639	23.086
$\chi_{water} = 0$ (VH pol.)	1224.625	26213.472	1060.907	23.212
$\chi_{water} = 0.296$ (VV pol.)	1224.731	35800.864	1463.143	22.987
$\chi_{water} = 0.296$ (VH pol.)	1225.048	22665.846	925.767	23.0005

A.5 Electric Field Fluctuation Decomposition

In Chapter 3, with the help of Dr. David Limmer, we have used the distribution of electric fields along the O-H bond of a water molecular as a map to the Raman line shape. We have found that these distributions are naturally decomposed into two sub-populations depending on whether the tagged O-H bond is donating a hydrogen bond to another water molecule or not. Using the same geometric definition for a hydrogen bond as discussed in Chapter 3, these decomposed distributions are shown in Figure 38 for a range of water concentrations.
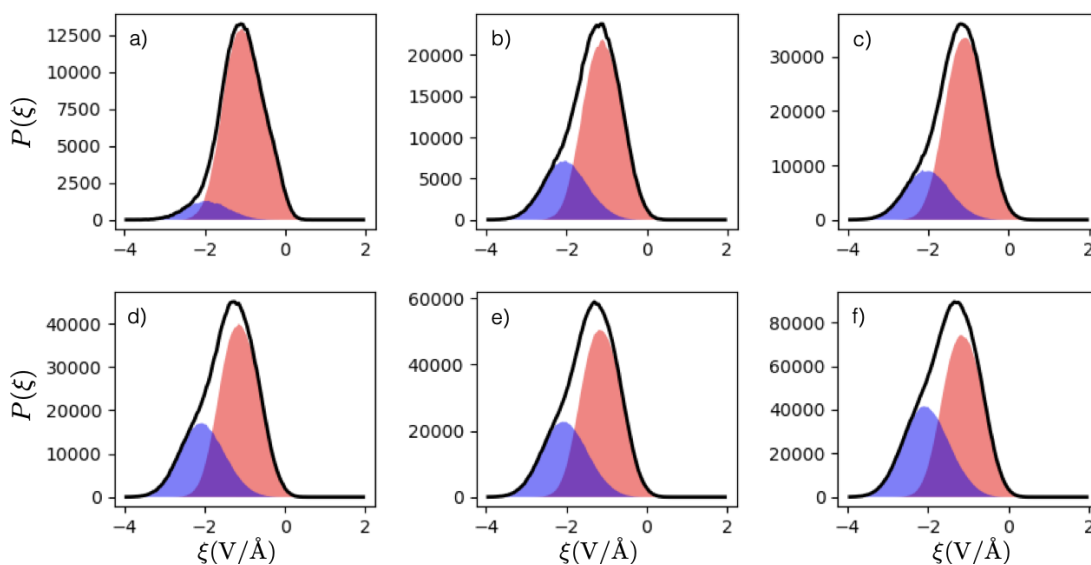
Figure 38. Electric field distributions for water solutions with χ_{water} = a) 0.04, b) 0.08, c) 0.12, d) 0.16, e) 0.19, and f) 0.22 computed from the molecular dynamics simulations discussed in Chapter 3. Shaded regions highlight sub populations for O-H oscillators that are donating a hydrogen (blue) or not (red) to another water molecule.

Appendix B. Supplemental Information for Chapter 4

B.1 Measurement of NO$_2$ Concentration

The concentration of NO$_2$ delivered to the liquid surface was determined using FTIR spectroscopy. To achieve this, the Teflon cell described in the main text was replaced by a 10 cm path length linear gas cell equipped with two ZnSe windows (Pike Technologies, part #: 162-2200). Using the gas purification system described in the main text, 50 mL/min N$_2$ and 5 mL/min zero air were flowed through the linear cell and to exhaust for 5 days before the experiment was started. After 5 days, the flow of 100 mL/min N$_2$ and 5 mL/min air through the cell was collected as background spectrum. Immediately following this, the NO$_2$ flow was set to 40 mL/min and spectra were acquired every 10 min. Spectra were collected using 128 scans and 4 cm^{-1} resolution. The intensity of the NO$_2$ peaks was monitored over time as the gas flowed through the cell. A constant intensity was reached after 30 min and the intensity of the NO$_2$ peak at 1602 cm^{-1} was used along with Beer's Law to calculate the concentration of NO$_2$. The average spectrum of NO$_2$ after 30 min flow through the linear cell during two trials is plotted in Figure 39. The absorbance (*A*) of the NO$_2$ peak occurring at 1602 cm^{-1} was determined to be 5.91x10^{-4}. Using Beer's law (*A=εbc*), the known 10 cm path length (*b*), and the previously reported absorption cross section (*ε*, 4.71x10^{-19} cm^2/molecule)[174] of NO$_2$ at 1602 cm^{-1}, the concentration was determined to be 5.1 ppm.
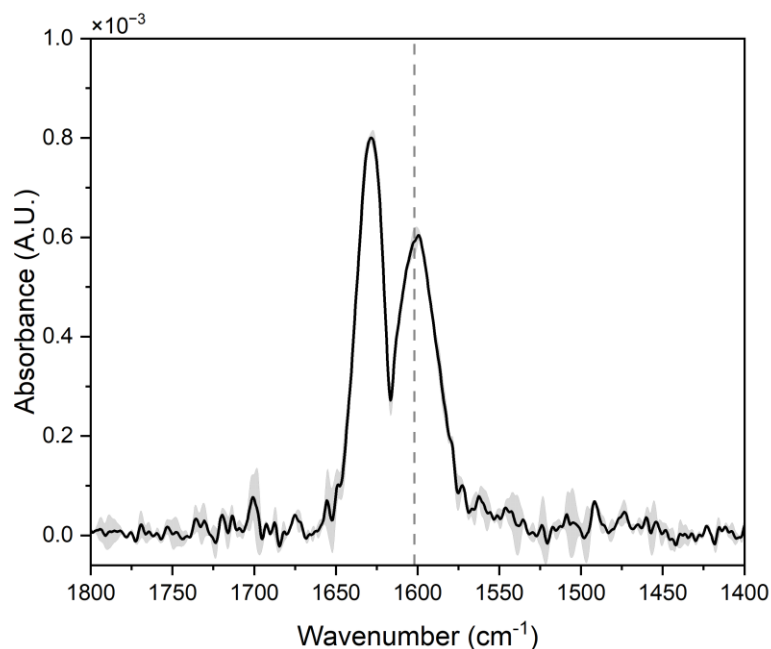
Figure 39. FTIR spectrum of NO_2 gas used to determine its concentration for surface studies. Dashed reference line included at 1602 cm^{-1} to indicate peak position of the absorbance used in the calculation. The spectrum is an average of two trials, with the standard deviation plotted as shading.

B.2 Spectral Pre-Processing & Baseline Correction

Following calculation of RA as described in the main text, a Savitzky-Golay filter was applied to all IRRAS spectra to improve the signal-to-noise ratio. The filter used 30 adjacent data points (15 cm^{-1}) to fit the noise to a second order polynomial function. The spectra were then all baseline corrected using OriginLab's built-in baseline correction functionality. Within the "peak analyzer" tab, the "subtract baseline" procedure was selected. To define the baseline, 7 anchor points were selected between 2300 and 800 cm^{-1} in regions of the spectrum where no vibrational modes occurred. The initial anchor points chosen for all IRRAS spectra were 806, 990, 1310, 1450, 1730, 2060, and 2238 cm^{-1}. Minute adjustments to these initial anchor points were made for each individual spectrum to ensure that the points represented the average of the noise in that particular region. The

123

anchor points were then fit using a linear function to define the baseline, which was subtracted.

B.3 Time-Resolved Spectra of PC Surface Before NO₂ Exposure
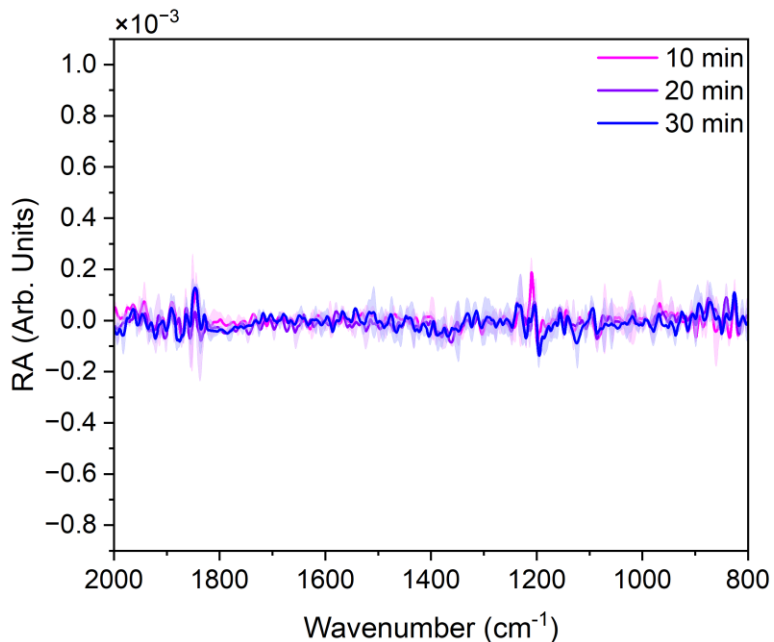
Figure 40. IRRAS spectra of 100 mL/min N₂ and 5 mL/min air flowing over the PC surface for 30 min. Spectra are an average of two trials, with the standard deviation plotted as shading. These results demonstrate that the flow of N₂ and air over the PC surface does not disrupt the vibrational modes of PC over time.

B.4 Propylene Carbonate Peak Assignments (IRRAS)
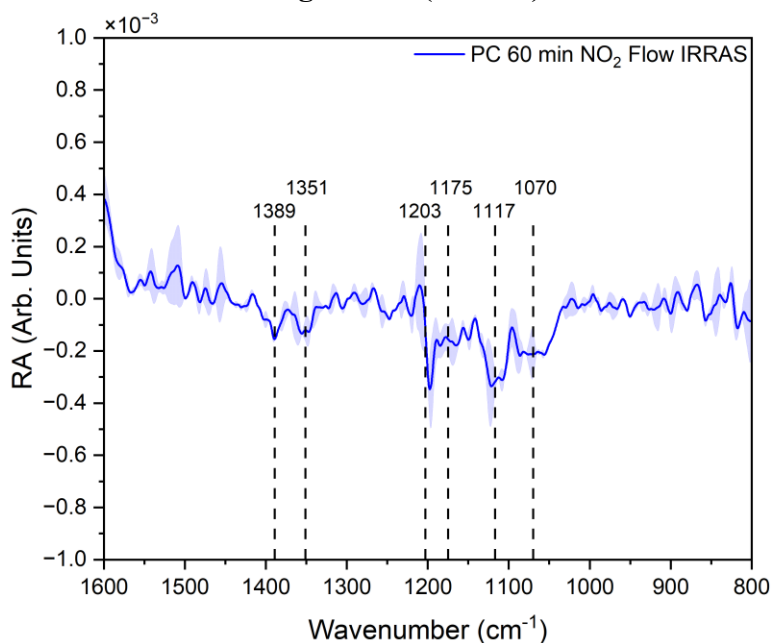
Figure 41. IRRAS spectra of the low frequency peaks observed when 5.1 ppm NO$_2$ was flowed over the PC surface for 60 min. Spectra are used to assign the observed peaks to the vibrational modes of PC. Dashed reference lines are included at the center of each band, and the position (in cm^{-1}) is labeled above the reference line.

Table 6. Summary of the low frequency peaks observed in the IRRAS spectrum of the PC surface during 60 min of NO$_2$ flow. Peaks are assigned by comparison to a previous study that combined ab initio calculations with experimental ATR-FTIR spectra of PC to make the vibrational assignments.

This Work (IRRAS, cm^{-1})	Literature (ATR-FTIR, cm^{-1})[2]	Assignment[2]
1389	1389	CH bend/rock
1351	1354	HCCH bend
1203	1225	CH$_2$ rock
1175	1184	CH$_2$ rock
1117	1120	In-plane ring + carbonate str. (O=COO)
1070	1077	In-plane asym. ring str.

B.5 Attenuated Total Reflection (ATR)-FTIR Spectroscopy Experiments

The spectrum of bulk PC without exposure to NO_2 was acquired using attenuated total reflectance (ATR)-FTIR. A Perkin Elmer diamond/KRS-5 universal ATR assembly was used with a Perkin Elmer Spectrum 100 FTIR spectrometer. The spectrum of the crystal following cleaning with ethanol was used as the background for all spectra. Propylene carbonate was transferred from the septum-sealed bottle using a syringe and 5 drops of the liquid were deposited onto the ATR crystal. ATR spectra of the PC sample were collected in duplicate using 128 scans and 4 cm^{-1} resolution.

B.6 Additional Diethyl Sebacate Experiments
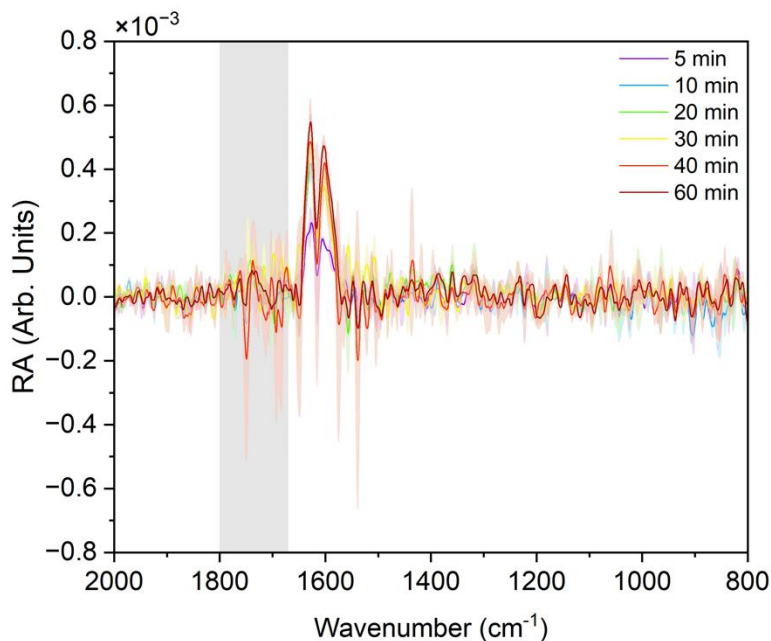
Figure 42. Time-resolved IRRAS spectra of NO_2 flowing over the surface of DES. The spectra presented are an average of two trials with the standard deviation plotted as shading. Only peaks belonging to NO_2 (1600 and 1630 cm^{-1}) are present in the spectra and no perturbation to the carbonyl is observed. This is in contrast to the carbonyl mode observed in the additional two replicated of DES and NO_2 presented in Chapter 4.

B.7 Determination of Water Content in PC using Raman Spectroscopy

Raman spectroscopy was used to evaluate the water content in the pure PC sample as well as determine the amount of water removed from the PC surface when following 120 min of air flow over the surface of a 0.091 mole fraction water-in-PC solution. Spectra were acquired using a custom-built Raman spectrometer (described elsewhere[182]) with 532 nm excitation. Spectra are collected by averaging 150 exposures with a 0.1 s exposure time. For studies of pure PC, the liquid was transferred from the septum-sealed bottle directly into the quartz cuvette and sealed with a cap equipped with a silicone gasket. These steps were taken to limit water contamination within the sample. For studies of PC/water solutions, 20 mL of PC was transferred to an acid-cleaned vial and mixed with the appropriate mass of water to achieve a 0.091 mole fraction of water in PC. An aliquot of this sample was taken and placed in a quartz cuvette then used to acquire the Raman spectrum of the solution before gas flow experiments. After the spectrum was acquired, the aliquot was returned to the original vial and used for the IRRAS flow experiments. Following the 120 min flow of N_2 and air over the PC/water surface, an aliquot of the sample was taken again and the Raman spectrum after the flow experiments was acquired. The OH stretching region in the Raman spectra of pure PC, 0.091 mole fraction PC/water before flow experiments, and PC/water after flow experiments is plotted in Figure 43. The OH stretching region is convoluted with the CH stretching modes of PC as observed from $3100 – 3350$ cm^{-1} in the Raman spectra. When water is added to PC, a sharp band at ~3550 cm^{-1} grows in along with a shoulder at ~3650 cm^{-1}. We have investigated the structure of water in PC that gives rise to these bands in a previous publication and find that these bands

127

result from mostly unassociated water molecules.[182] Here, the absence of these peaks in the pure PC spectrum (Figure 43, black) indicate that the water content is below the limit of detection. When considering the PC/water spectra before (Figure 43, dark blue) and after (Figure 43, light blue) 120 min of air flow over the surface, there is a marked decrease in the OH stretching band intensity of ~2/3. While the intensity of Raman bands does not correlate linearly with concentration, we can conclude that water was removed from this system during the flow experiments. Moreover, these results support that the changes observed in the IRRAS spectra during N_2 and air flow over the PC/water solution is due to dehydration of the surface.
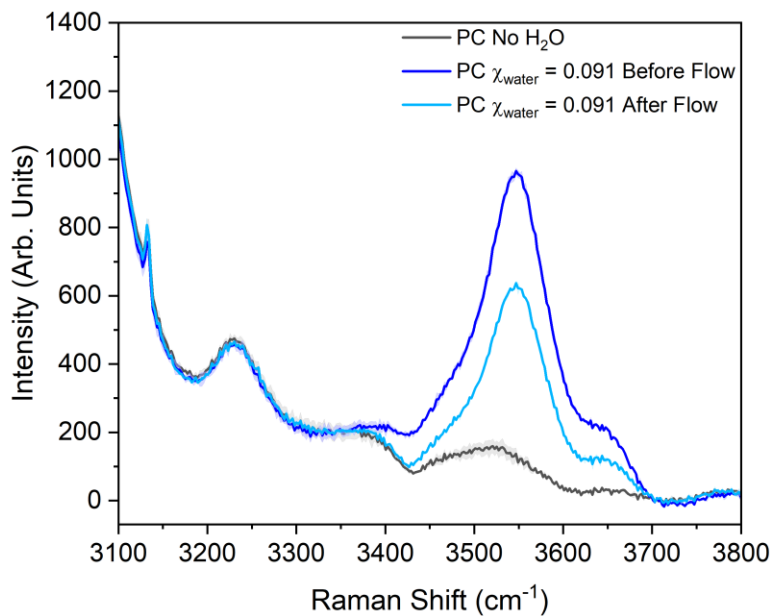
Figure 43. Raman spectra in the OH stretching region of pure PC (black), 0.091 mole fraction of water in PC before flow experiments (dark blue), and 0.091 mole fraction of water in PC after flow experiments (light blue).

B.8 IRRAS Spectra of NO$_2$ Flow Over PC/water Solution
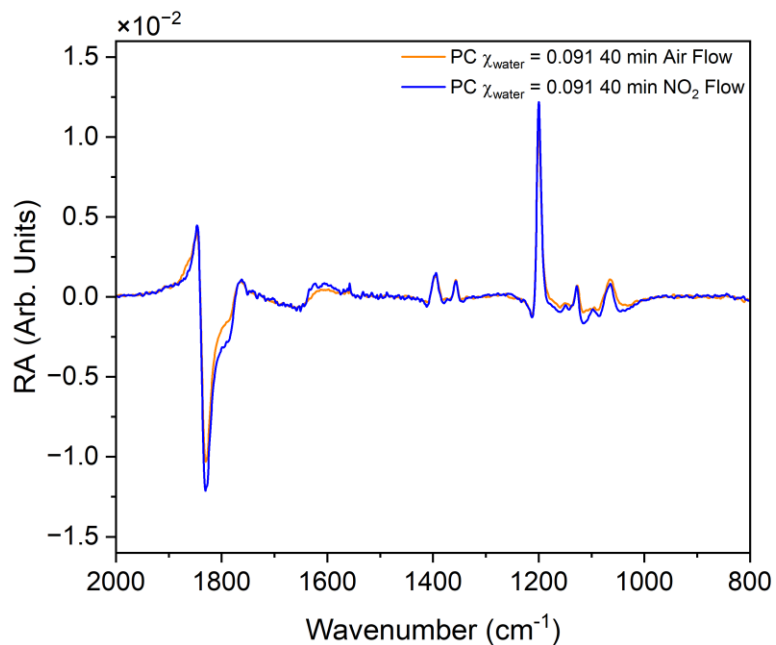
Figure 44. IRRAS spectra of the PC + H$_2$O surface after 40 min of dehydration (orange) and 40 min of NO$_2$ exposure (blue). The reference used to calculate RA for the dehydration spectrum is the initial reference spectrum taken at time 0. The reference used to calculate RA for the NO$_2$ exposure is the spectrum taken after 40 min flow of N$_2$ and air over the surface (sample spectrum used in orange trace). The IRRAS spectra can then be compared as they represent the same duration of gas flow over the surface. The changes caused by dehydration vs. those caused by the presence of NO$_2$ cannot be deconvoluted.

Appendix C. Supplemental Information for Chapter 5

C.1 UV-Vis Measurement of O_3 Concentration

The concentration of ozone produced using the gas synthesis system described in Chapter 5 was determined using UV-Visible spectroscopy. To enable this measurement, the Teflon cell was replaced by a 10 cm pathlength flow-through cuvette. The gas connections to the 0.25 in. inlet and outlet tubes at the top of the cuvette were made using PFA Swagelok tube fittings. A deuterium-halogen lamp (OceanOptics, DT-mini) was used as the excitation source and the sample was irradiated using a 300 μm solarization resistant fiber optic to couple the source to the collimating lens of the cuvette holder (CUV-UV-10). The signal was detected using a second 300 μm solarization resistant fiber optic that coupled the collection lens of the cuvette holder to the spectrometer (OceanOptics, USB 2000).

Ozone was produced by flowing 150 sccm (mL/min) of N_2 and 5 sccm of air through an ozone generator (Jelight, model 610), then through the absorption cell, and to exhaust. The ozone generator consists of a stainless-steel housing, which encloses a Hg pen lamp. The lamp is sheathed by a glass test tube that is used to tune the concentration of O_3 produced. The greater the test tube is extended from the housing, the more O_3 is produced. The tube was extended 66 mm from the housing for all experiments. The UV absorption spectrum was acquired by first acquiring a reference spectrum of the N_2 and O_2

flow through the cell with the Hg lamp turned off. The Hg lamp was then turned on to begin producing O_3. The intensity of the absorption band at ~254 nm was monitored over time and the spectrum was recorded after the intensity stabilized (30 min after lamp turned on). OriginLab was used to fit the absorption band at 254 nm to a gaussian and the maximum absorbance was determined to be 0.027. The absorption spectrum of O_3 and the result of the gaussian fit are presented in Figure 45. Using Beer's law ($A=\varepsilon bc$), the known 10 cm path length (b), and the previously reported absorption cross section (ε, 1.15×10^{-17} cm^2/molecule)[1] of O_3, the concentration was determined to be 9.62 ppm. When the flow rate of N_2 is decreased to 100 mL/min, the concentration of ozone is increased. This concentration was estimated to be 15 ppm from the ratio of flow rates.
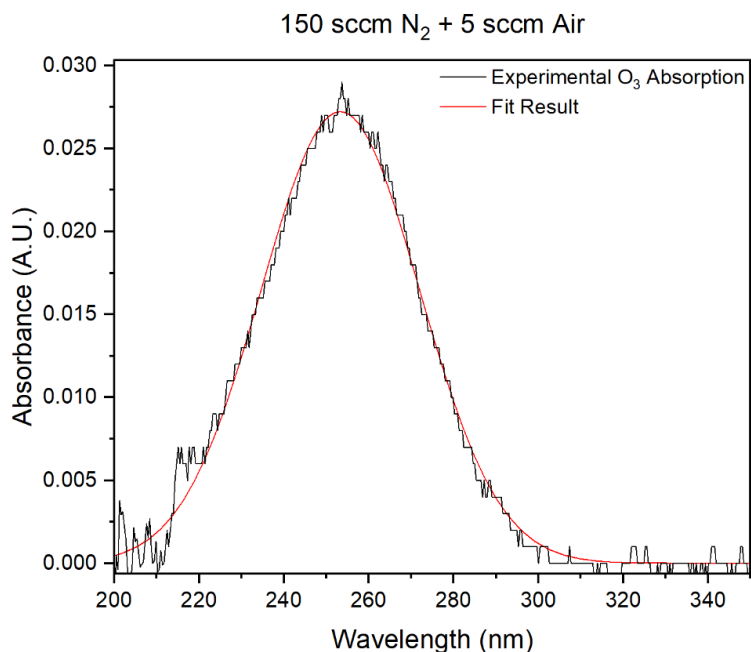
Figure 45. UV-Vis spectrum of the O_3 flow produced from 150 mL/min N_2 and 5 mL/min air (black). The result of the gaussian fit used to determine the maximum absorbance is also included (red).

C.2 List of Materials Used in Gas System

Table 7. Tabulation of all materials used to build the gas synthesis system described in Chapter 5 along with specifications and part numbers.

Item	Specifications	Supplier	Part Number/Link
Teflon Tubing	1/4" O.D. 1/8" I.D.,	Swagelok	PFA-T4-062-100
Straight Union	1/4", PFA	Swagelok	PFA-420-6
Tee Union	1/4", PFA	Swagelok	PFA-420-3
Elbow Union	1/4", PFA	Swagelok	PFA-420-9
Groove Cutter	1/4"	Swagelok	MS-GC-4
Plug Valve	1/4", PFA	Swagelok	PFA-43S4
Reducing Union	1/2" to 1/4" PFA	Swagelok	PFA-820-6-4
Reducing Union	3/8" to 1/4" PFA	Swagelok	PFA-620-6-4
Male connector	1/4" PFA	Swagelok	PFA-420-1-4
Front ferrule spare	1/4" PFA	Swagelok	PFA-423-1
Back ferrule spare	1/4" PFA	Swagelok	PFA-424-1
Snoop leak detector	8 oz bottle	Swagelok	MS-SNOOP-8OZ
Ozone generator	N/A	Jelight	610
Reaction Chamber	12 in. x 2 in.	Glass blower	N/A
Traps/bubblers	200 and 250 mm long with tapered joint	Chemglass	CG-4516-01 & CG-4516-07
Grease for trap joints	Krytox fluorinated grease	Chemglass	CG-GPL-205-01
Keck Clamps	29/42 and 40/50	Chemglass	CG-145-06
Large o-ring	#232, FFKM, o-ring	Grainger	741W31
Small o-ring (windows)	# 027, FFKM o-ring	Grainger	741V98
ZnSe Windows	37.5 mm x 4 mm	PIKE Technologies	160-1291
UHP N_2	Nitrogen 5.0, UHP 99.999%- K	Gas Warehouse	98287
Air	Air Class 2.2 ZERO K cylinder	Gas Warehouse	98768
NO_2	50 ppm NO_2 in N_2.	Gas Warehouse, Non-Catalog	NI NX50MC-AS
Nylon mesh	100% nylon, 1 yard	Joann Fabrics	White nylon mesh fabric
Tube Cutters	Pack of 3	Amazon	N/A
KOH	ACS Reagent >85%	Millipore Sigma	221473-500G
NO_2 Monitor	MSA Alt Air 2X NO_2	IE Monitoring Instruments	MSA10154078
Calibration gas	10 ppm NO_2 44 L	Grainger	16M559
Regulator	5/8 UNF 0.25 LPM	Grainger	33V726

C.3 FTIR Spectra of N$_2$O$_5$ During Purge
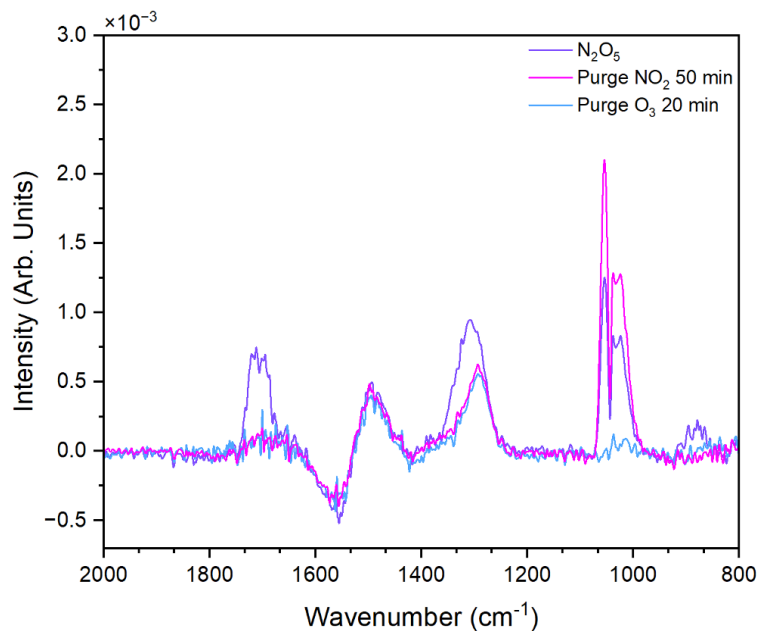
Figure 46. FTIR spectrum of 60 min N$_2$O$_5$ flow through linear cell (purple) along with the FTIR spectra 50 min after turning off the NO$_2$ flow (pink) and 20 min after stopping O$_3$ production (blue). Spectra demonstrate that the peaks at 1495 and 1560 cm^{-1} do not decrease in intensity upon purging, supporting that they result from adsorbed species.

C.4 Effect of 3Å Molecular Sieves on NO₂ Flow
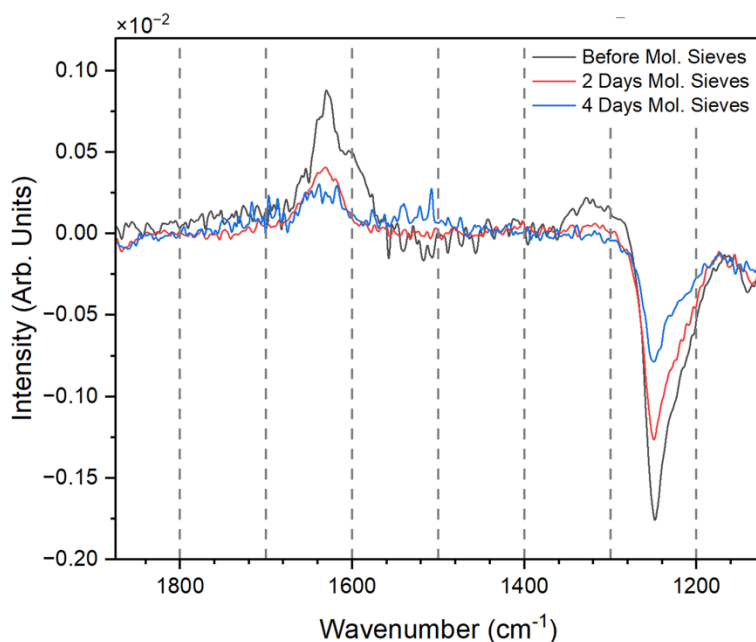
Figure 47. IRRAS spectra of NO_2 flowing over gold mirror before 3Å molecular sieves were added to trap (black), 2 days after they were added (red), and 4 days after they were added (blue). Spectra show that the sieves adsorb NO_2 to a significant extent through the decrease in intensity over time for the gas-phase NO_2 bands at 1600 and 1630 cm^{-1} as well as the band at 1250 cm^{-1} from the NO_2 adsorbed on the gold mirror surface.

Appendix D. Kramers-Kronig Transformation of Reflectance Spectra

D.1 Theory

In reflection spectroscopy, a strong IR absorption leads to a significant change in reflectivity which can cause bands with a distinct derivative shape. This line shape is due to the superposition of spectra from the real (refractive) and imaginary (absorptive) components of the complex refractive index. For the case of specular reflection off of a single interface, a Kramers-Kronig transformation can be used to correct these line shapes.[1,2] In general, the Kramers-Kronig relation defines the relationship between the real $\chi_r(\omega)$ and imaginary $\chi_{im}(\omega)$ components of a complex function $\chi_c(\omega)$. If we consider the complex function:

Equation 48

$$\chi_c(\omega) = \chi_r(\omega) + i\chi_{im}(\omega)$$

The Kramers-Kronig relation between the real and imaginary parts of the function can be written as follows:

Equation 49

$$\chi_r(\omega_0) = \frac{2}{\pi}\mathcal{P}\int_0^\infty \frac{\omega\chi_{im}(\omega)}{\omega^2 - \omega_0^2}d\omega$$

Equation 50

$$\chi_{im}(\omega_0) = -\frac{2\omega_0}{\pi}\mathcal{P}\int_0^\infty \frac{\chi_r(\omega)}{\omega^2 - \omega_0^2}d\omega$$

where ω is the angular frequency in rad/s, $\mathcal{P}$ is the Cauchy principal value, and $\chi_r(\omega)$ and $\chi_{im}(\omega)$ are the real and imaginary components of the complex function $\chi_c(\omega)$, respectively.

The Kramers-Kronig relation can be used to correct derivative line shapes in reflection spectra due to the complex nature of the Fresnel reflection coefficient, r, which dictates reflection from an interface due to the interaction of light with a material's complex refractive index. The complex Fresnel reflection coefficient can be written as:

Equation 51

$$r = |r|e^{i\phi}$$

where ϕ and $|r|$ are the phase and modulus of the reflection coefficient, respectively. The experimental reflectance spectrum ($R(\omega)$) is the ratio of the intensity of light reflected off the sample and the intensity of light reflected off a gold mirror reference. The reflectance spectrum is equal to the square modulus of the reflection coefficient which when solved for r gives:

Equation 52

$$r = \sqrt{R(\omega)}e^{i\phi}$$

Taking the natural logarithm of both sides of equation 5 yields:

Equation 53

$$\ln(r) = \ln(\sqrt{R(\omega)}) + i\phi$$

Equation 53 demonstrates that the experimental reflectance spectrum and the phase of the reflection coefficient are a Kramers-Kronig pair. Thus, $\phi(\omega)$ can be obtained through a Kramers-Kronig transformation of the experimental spectrum as demonstrated below:[3,4]

136

Equation 54

$$\phi(\omega_0) = -\frac{2\omega_0}{\pi} \mathcal{P} \int_0^\infty \frac{\ln\sqrt{R(\omega)} - \ln\sqrt{R(\omega_0)}}{\omega^2 - \omega_0^2} d\omega$$

Multiple methods to numerically solve the above integral have been developed.[5] Here, McLaurin's formulae is used to solve for ϕ as follows:

Equation 55

$$\phi(\omega_i) \cong -\frac{2\omega_i}{\pi} \times 2h \times \sum_j f_j$$

where h is the frequency step-size and f_j is defined as:

Equation 56

$$f_j = \frac{\ln\sqrt{R(\omega_j)} - \ln\sqrt{R(\omega_i)}}{\omega_j^2 - \omega_i^2}$$

The integral given in Equation 56 has a singularity when $\omega_j = \omega_i$ therefore the indices of the above summation are chosen to avoid direct calculation of the point where $j = i$. Evaluation of the Kramers-Kronig transformation requires integration over all frequency space, however only the reflectance for a finite range of frequencies is known. In order to obtain a more accurate solution to the transform, it is typically useful to extrapolate the reflectance data to zero and far beyond the maximum experimental frequency.[6–8] Others have reported that extrapolation was not necessary.[7] We find that extrapolation does not provide significant improvement to results.

Once the value of $\phi(\omega)$ has been determined, Equation 52 can be used to solve for the complex value of r, which allows for determination of the complex refractive index of the sample. The reflection coefficient for s-polarization (polarization perpendicular to the

137

plane of incidence) is given by Equation 34. Using Snell's law (Equation 32), Equation 34 can be rearranged to solve for the complex refractive index of the reflecting medium:[3,8]

Equation 57

$$\tilde{n}_2 = \tilde{n}_1 \left(sin^2(\theta_i) + \left(\frac{r_s - 1}{r_s + 1} \right)^2 cos^2(\theta_i) \right)^{1/2}$$

Here, the incident medium is air, therefore $\tilde{n}_1 = 1$. The complex refractive index is then a function of the complex Fresnel coefficient and the angle of incidence. The absorption spectrum can then be obtained from the imaginary component of $\tilde{n}_2$ using the following relationship:[4]

Equation 58

$$\alpha(\omega) = \frac{4\pi k(\omega)}{\lambda_0}$$

where $\alpha(\omega)$ is the absorption coefficient, λ_0 is the wavelength of light in vacuum, and $k(\omega)$ is the imaginary component of the refractive index. Note: KK transform assuming normal incidence has been applied to spectra obtained with non-normal incidence and allowed for quantitative information.[2] This is important because the analysis is much simpler and extrapolation was found to not be necessary for our data.[7,9]

D.2 Python Code

The input required for this code is a gold mirror reflectance spectrum to use as a reference and between 1 and 3 trials of reflectance spectra measured off a sample interface in s-polarization.

```
"""
Created on Thu Mar  3 11:01:34 2022

@author: jessicabclark
```

138

```python
"""
import matplotlib.pyplot as plt
import pandas as pd
import os
import numpy as np

#Set material studed
material = 'Diethyl Sebacate v-polarized'

#Set incidence angle of IRRAS
Incident_deg = 48
theta = Incident_deg*(np.pi/180) #radians

#Input number of experimental trials
Num_Trials = 3

#Name files to import
Data_1 = 'DES_Vpol_1.asc'
Data_2 = 'DES_Vpol_2.asc'
Data_3 = 'DES_Vpol_3.asc'

Au_bkg = 'Au_Mirror_Avg_11-17-2021.xls'

#Change path to folder with raw data
path = r'/Users/jessicabclark/Library/CloudStorage/OneDrive-
TheOhioStateUniversity/Research/N2O5 Project/KK Python/DES Vpol 4-6-2022'
os.chdir(path)

#Import raw reflection data as data frames and name columns
#Remove data below 750 cm-1 b/c of noise
Data_1 =
pd.DataFrame(np.genfromtxt(path+'/'+Data_1,skip_header=25,skip_footer=600))
Data_1.columns = ['Omega','Intensity']
Data_2 =
pd.DataFrame(np.genfromtxt(path+'/'+Data_2,skip_header=25,skip_footer=600))
Data_2.columns = ['Omega','Intensity']
Data_3 =
pd.DataFrame(np.genfromtxt(path+'/'+Data_3,skip_header=25,skip_footer=600))
Data_3.columns = ['Omega','Intensity']

#Import gold mirror background
#Remove data below 750 cm-1 b/c of noise
Au_bkg = pd.read_excel(Au_bkg,header=2,skipfooter=600)
Au_bkg.columns = ['Omega','Intensity','stdev(Intensity)']
```

```python
#Pull frequency in cm-1 from experimental data
omega = Au_bkg.iloc[:,0]
omega = np.asarray(omega)

#Convert frequency to angular frequency in rad*s-1
nu = omega*(3*10**10)*2*np.pi
dnu = nu[0]-nu[1]

#Calculate R(w) by taking ratio of each trial by avg gold mirror background then change
to numpy array
R1 = Data_1.iloc[:,1]/Au_bkg.iloc[:,1]
R1 = np.asarray(R1)
R2 = Data_2.iloc[:,1]/Au_bkg.iloc[:,1]
R2 = np.asarray(R2)
R3 = Data_3.iloc[:,1]/Au_bkg.iloc[:,1]
R3 = np.asarray(R3)
R_All = np.column_stack((R1,R2,R3))

#Take the natural log of the square root of R(w)
LnsqrtR1 = np.log(np.sqrt(R1))
LnsqrtR2 = np.log(np.sqrt(R2))
LnsqrtR3 = np.log(np.sqrt(R3))
Lnsqrt_All = np.column_stack((LnsqrtR1,LnsqrtR2,LnsqrtR3))

#########Start Kramers-Kronig Transformation#########

#use Krames-Kronig to calculate phi for each trial
f = np.zeros((len(nu),len(nu)))
fsum = np.zeros((len(nu),Num_Trials))
for i in range((Num_Trials)):
    for j in range(0, len(nu)):
        for k in range(0, len(nu)):
            if j != k:
                f[j, k] = (Lnsqrt_All[k,i]-Lnsqrt_All[j,i])/(nu[k]**2-nu[j]**2)
    fsum[:,i] = np.sum(f,1)

phi = np.zeros((len(fsum),Num_Trials))
for i in range((Num_Trials)):
    for j in range(0, len(fsum)):
        phi[j,i] = -(2*nu[j]/np.pi)*2*dnu*fsum[j,i]

#Calculate complex Fresnel factor for s-polarization
r_complex = np.zeros((len(phi),Num_Trials), dtype=complex)
```

```python
for i in range((Num_Trials)):
    for j in range(0, len(phi)):
        r_complex[j,i] = np.sqrt(R_All[j,i])*np.exp(phi[j,i]*1j)

#Calculate complex index of refraction
n_complex = np.zeros((len(phi),Num_Trials), dtype=complex)
for i in range((Num_Trials)):
    for j in range(0, len(r_complex)):
        n_complex[j,i] = np.sqrt((np.sin(theta))**2*((r_complex[j,i]-
1)/(r_complex[j,i]+1))**2*(np.cos(theta))**2)

#Extract imaginary component of index of refraction to get absorption information
k = np.zeros((len(r_complex),Num_Trials))
for i in range((Num_Trials)):
    for j in range(0, len(n_complex)):
        k[j,i] = np.imag(n_complex[j,i])

k_avg = np.mean(k,axis=1)
k_std = np.std(k, axis=1)

n = np.zeros((len(r_complex),Num_Trials))
for i in range((Num_Trials)):
    for j in range(0, len(n_complex)):
        n[j,i] = np.real(n_complex[j,i])

n_avg = np.mean(n,axis=1)
n_std = np.std(n, axis=1)

#Save data as a CSV
df =
pd.DataFrame(data=np.column_stack((omega,k_avg,k_std)),columns=['omega','Average
k','stdev k'])
df.to_csv("DES_48deg_Vpol_H_analysis.csv")

lamb = np.zeros((len(omega),1))
for i in range(0, len(omega)):
    lamb[i] = (omega[i]**-1)*1*10**7

mu = np.zeros((len(lamb),3))

for i in range((Num_Trials)):
    for j in range(0,len(lamb)):
        mu[j,i] = 4*np.pi*k[j,i]/lamb[j]
```

```
mu_avg = np.mean(mu,axis=1)
mu_std = np.std(mu, axis=1)

fig1 = plt.figure()
x = omega
y = -LnsqrtR1
plt.xlim([800, 4000])
plt.plot(x,y)

fig2 = plt.figure()
x = omega
y = k_avg
std = k_std

plt.plot(x,y,'k')

plt.fill_between(x,y-std, y+std, color ='k', alpha = 0.3)
plt.xlim(800,4000)
#plt.ylim([-0.25, 0.25])
plt.title(material+ ' Kramers-Kronig Transformation')
plt.xlabel('wavenumber ($cm^{-1}$)')
plt.ylabel('k')
plt.savefig('DES_imag_KKTransform_Vpol_H_analysis.pdf')

fig3 = plt.figure()
x = omega
y = n_avg
std = n_std

plt.plot(x,y,'k')

plt.fill_between(x,y-std, y+std, color ='k', alpha = 0.3)
plt.xlim(800,4000)
#plt.ylim([-0.25, 0.25])
plt.title(material+ ' Kramers-Kronig Transformation')
plt.xlabel('wavenumber ($cm^{-1}$)')
plt.ylabel('n')
plt.savefig('DES_real_KKTransform_Vpol_H_analysis.pdf')
```

#########################End Code#########################

The reflectance spectra of the PC and DES surfaces before and after the Kramers-Kronig

transformation are presented in Figure 48 and Figure 49, respectively.
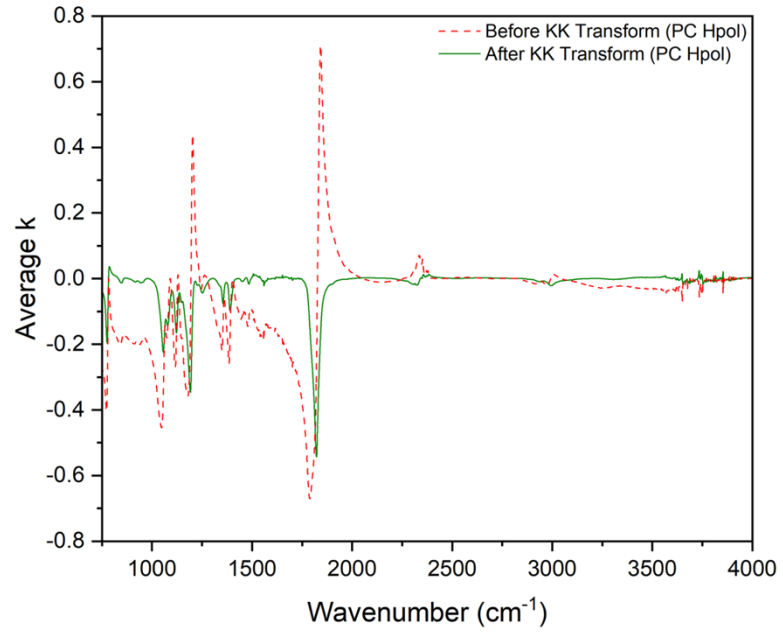
Figure 48. Reflectance spectrum of the PC surface before (red dashed) and after (green solid) the Kramers-Kronig transformation.
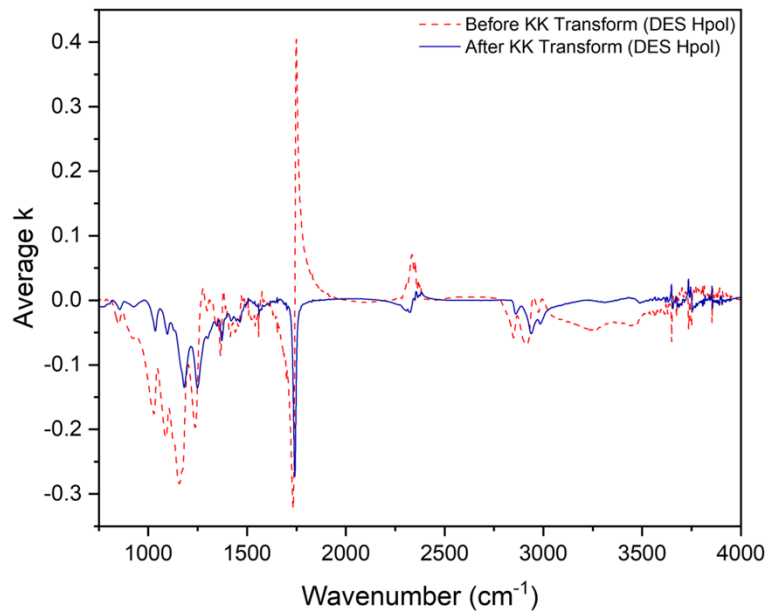
Figure 49. Reflectance spectrum of the DES surface before (red dashed) and after (blue solid) the Kramers-Kronig transformation